The Dissertation Committee for Derek Edward Sawyer Certifies that this is the approved version of the following dissertation:

FAILURE MECHANICS, TRANSPORT BEHAVIOR, AND MORPHOLOGY OF SUBMARINE LANDSLIDES

Committee:

Peter B. Flemings, Supervisor

David Mohrig

Luc Lavier

Matthew Hornbach

Maria Nikolinakou

R. Craig Shipp

FAILURE MECHANICS, TRANSPORT BEHAVIOR, AND MORPHOLOGY OF SUBMARINE LANDSLIDES

by

Derek Edward Sawyer, B.S. M.S.

Dissertation

Presented to the Faculty of the Graduate School of
The University of Texas at Austin
in Partial Fulfillment
of the Requirements
for the Degree of

Doctor of Philosophy

The University of Texas at Austin
December 2010

Acknowledgements

I would like to thank my wife Audrey and my family and friends for their constant support throughout the long process of completing this Ph.D., which occurred over the course of 5 years and 2 states.

I have benefitted greatly from a dissertation committee with broad expertise in the geosciences. I thank my advisor Peter Flemings for giving me the opportunity, funding, facilities, and persistent push to learn more and communicate better. Peter's enthusiasm and work ethic are outstanding. I am grateful to David Mohrig for the opportunity to explore experimental mudflows in the Morphodynamics Lab. I would like to extend a special thanks to Dr. Jim Buttles who spent many hours working with me during my foray into experimental sedimentology. The expertise and experience provided by David and Jim were invaluable to the project reported in Chapter 3. I thank Craig Shipp for encouraging me to pursue a Ph.D. and for providing an internship at Shell in 2005 during which I was able to jumpstart my Ph.D. research by synthesizing data collected on Expedition 308 (Ch. 1). I have learned a great deal from Craig's extensive knowledge of Mars-Ursa stratigraphy and his experience in geohazard projects around the world. I thank Maria Nikolinakou for letting me pick her brain on theoretical soil mechanics and the finite element soil modeling software PLAXIS. From Penn State I thank Heather Nelson, Prof. Rudy Slingerland, and Prof. Chris Marone.

I thank my fellow graduate students and colleagues at both at Penn State University and at the University of Texas. In particular, Julia Schneider, Yao You, Hui Long, Shawn Goldman, Jon Samuelson, and Brandon Dugan.

Finally, I thank the following for monetary support: the University of Texas Institute for Geophysics Ewing/Worzel fellowships, Conoco Phillips SPIRIT Scholarship, Chevron Excellence award, and the AAPG Raymond D. Woods Memorial Grant.

FAILURE MECHANICS, TRANSPORT BEHAVIOR, AND MORPHOLOGY OF SUBMARINE LANDSLIDES

Derek Edward Sawyer, Ph.D.

The University of Texas at Austin, 2010

Supervisor: Peter B. Flemings

Submarine landslides retrogressively fail from intact material at the headwall and then become fluidized by strain weakening; the final deposits of these flows have low porosity, which controls their character in seismic reflection data. Submarine landslides occur on the open slope and also localized areas including margins of turbidite channel-levee systems. I develop and quantify this model with 3-D seismic reflection data, core and log data from Integrated Ocean Drilling Program Expedition 308 (Ursa Basin, Gulf of Mexico), flume experiments, and numerical modeling. At Ursa, multiple submarine slides over the last 60 ky are preserved as mass transport deposits (MTDs). Retrogression proceeded from an initial slope failure that created an excavated headwall, which reduced the horizontal stress behind the headwall and resulted in normal faults. Fault blocks progressively weakened until the gravitational driving stress imposed by the bed slope exceeded soil strength, which allowed the soil to flow for more than 10 km away from the source area. The resulting MTDs have lower porosity (higher bulk density) relative to non-failed sediments, which ultimately produces high amplitude reflections at the base and top of MTDs. In the laboratory, I made weak (low yield strength) and strong flows (high yield strength) from mixtures of clay, silt, and water. Weak flows generate turbidity currents while moving rapidly away from the source area. They create thin and long deposits with sinuous flow features, and leave behind a relatively smooth and featureless source area. In contrast, strong flows move slowly, do not generate a turbidity current, and create blocky, highly fractured source areas and short, thick depositional lobes. In Pleistocene turbidite channels of the Mississippi Fan, deep-seated rotational failures occurred in the flanking levees. The rotational failures displaced material into the channel from below where it became eroded by turbidity flows. This system achieved a delicate steady state where levee deposition and displacement along the fault into the channel was balanced by erosion rate of turbidity flows. This work enhances our understanding of geohazards and margin evolution by illuminating coupled processes of sedimentation, fluid flow, and deformation on passive continental margins.

Table of Contents

List of Tables

List of Figures

Chapter 1: Introduction

Continental margins are ubiquitously affected by submarine landslides. Submarine landslides occur when the down-slope component of shear stress exceeds the resisting shear strength of the soil mass, which can be triggered by earthquakes, high overpressures, storm waves, and tectonic processes (oversteepening due to crustal uplift). The deposits of past slides, termed Mass Transport Deposits (MTDs), occur in a wide range of depositional environments, with highly variable geometries, lithologies, and geotechnical properties. The observation that MTDs comprise a significant fraction of continental margin deposits underscores that understanding the processes associated with submarine landslides is key for understanding how continental margins are constructed and reshaped over time. From a hazards perspective, submarine landslides can damage seafloor facilities and generate tsunamis that can devastate coastal communities and threaten human lives. From an offshore drilling and well design perspective, MTDs are typically densified (have lower porosity) than non-remobilized sediment, which can significantly increase the installation time of self-penetrating jetted conductors ("jet pipes") and suction anchor piles.

Seismic reflection technology and interpretation software have rapidly improved in the past few decades and are the main tool used to image MTDs. The advantages of seismic reflection data are that the complex three-dimensional spatial morphology and internal architecture of submarine landslides can be analyzed in great detail quickly and effectively. However, seismic data does not yield direct information about the processes that ultimately created the observed morphology nor of in-situ geotechnical properties (e.g., porosity, lithology, pore pressure, and stress state). As a result, the marine geosciences community has compiled a vast catalog of deposit morphologies from continental margins around the world. However, the ultimate goal is to link the seismic observations to an understanding of failure and transport processes. This is turn can yield powerful insight for analyzing in-situ slope conditions, for hazards analyses, and for designing installation infrastructures (e.g., pipelines, wells, platform piles). The goal of this dissertation is a detailed understanding of the link between seismic facies and in-situ rock properties of MTDs, and ultimately, the underlying processes associated with submarine landslide failure, movement, and deposition. I synthesize different approaches by geoscientists who analyze MTDs in seismic data, outcrops, and cores, numerical modelers who simulate the physical transport processes, and the geotechnical engineer who has a detailed understanding of the stress-strain behavior of soils.

In the following chapters I explore the mechanics of submarine landslide failure, transport processes during landslide movement, and how these are recorded in the seismic facies and rock properties. My methods include a detailed core-log-seismic analysis through of a series of submarine landslide deposits in the Gulf of Mexico, laboratory experiments of subaqueous mudflows, and finite element modeling of deep-seated failures along the margins of channel-levee systems. The key contributions of this work are 1) how seismic facies link to the physical properties of landslide deposits, 2) how large retrogressive landslide complexes progressively weaken from block failure to a state of flow, 3) how the morphology of submarine landslide deposits record pre-failure stress conditions and dynamic flow behavior, and 4) that an evolving channel-levee system can destabilize as a result of channel incision and rapid levee loading, which is an important control on the lifespan of the channel. These results have significant implications for geohazards analyses, offshore drilling/well design, and understanding the slope failure processes and products that exert a fundamental control on continental margin stratigraphy.

CHAPTER 2: RETROGRESSIVE FAILURES RECORDED IN MASS TRANSPORT DEPOSITS IN THE URSA BASIN, GULF OF MEXICO

I link seismic response, rock properties from core and log, and triaxial shear experiments to develop a conceptual and quantitative model of the multi-stage process of failure and post-failure evolution of submarine landslides in the Ursa Basin, Gulf of Mexico. I first present a detailed well-seismic tie and correlate between well sites from Integrated Ocean Drilling Program Expedition 308. High-amplitude seismic reflections and large excursions in resistivity record densification and not a lithologic contrast within clay-rich Mass Transport Deposits (MTDs) of the Ursa Basin. Within a single MTD densification is greatest near the base and it declines upwards, which controls the prominent basal reflection and the weak upper reflection observed in seismic. I defined two seismic facies within the MTDs. A Chaotic facies records greater transport based on our observation of grooves and flow-like features. This facies has the highest degree of densification and soft sediment deformation. In contrast, the Discontinuous Stratified facies suggests only limited transport: there are no grooves or flow-like features in seismic, pinnacles are undeformed sediments that have not moved, and soft sediment deformation is subtle in core. I then interpret my observations in terms of failure, transport, and depositional processes of clay-rich submarine landslides. I demonstrate that a high pore pressure ratio and strain-weakening were necessary to allow retrogressive failures in these sediments. Flow of material proceeded downslope for many kilometers because the gravitational driving stress was greater than the critical state strength. The ultimate deposits have a characteristically low porosity relative to bounding sediment and this controls their acoustic impedance.

CHAPTER 3: MUDFLOW TRANSPORT BEHAVIOR AND DEPOSIT MORPHOLOGY: ROLE OF SHEAR STRESS TO YIELD STRENGTH RATIO IN SUBAQUEOUS EXPERIMENTS

In this study I build on Chapter 2 by exploring how the morphology of submarine landslide deposits record the pre-failure conditions and transport behavior. I developed a novel approach to trigger subaqueous mudflows from 10-cm thick mud beds for which I know the shear stress and shear strength *a priori*. Thus I am able to explore how the difference between shear stress and shear strength, defined as the Flow Factor (F_f = shear strength/yield strength), controls the resulting dynamic mudflow and the morphology of the deposit. I monitor the evolving flow with time lapse photos and video, and I map the final deposit with a high resolution laser scanner. A key result is that when yield strength and shear stress are nearly equal (F_f ~1), the result is a slow moving, low-volume, mudflow that retrogressively fails from the source area. The deposits grow piecewise as each fault block detaches from the source and accumulates at the back of the deposit. When the difference between yield strength and shear stress is large (F_f >1), the sediment bed is weak relative to the driving stress and thus generates a long-runout, high-volume flow. A second key result is that the yield strength is proportional to clay content and inversely proportional to water content. I show under what conditions clay-rich and silt-rich sediment can produce similar mudflows and deposit morphologies. This work illustrates that detailed analysis of mudflow deposit morphology can yield important clues to the pre-failure stress conditions when the flow was initiated as well as the flow behavior. This has important implications for hazard assessments and for interpreting depositional history of past mudflows from a detailed analysis of surface morphology.

CHAPTER 4: DEEP-SEATED FAILURE AND EROSION OF LEVEES IN TURBIDITE CHANNELS OF THE UPPER MISSISSIPPI FAN, GULF OF MEXICO

In this study I explore the fascinating interplay of rapid sedimentation and slope failure recorded in two Late Pleistocene channel-levee systems on the Mississippi Fan. Rapid levee accumulation rate outpaced fluid pressure diffusion, which in turn triggered paired rotational slump zones on both margins of the channel. In this manner, I propose a steady state system evolved where sedimentation on the levee was accommodated by displacement along the fault, and erosion of the toe thrusts by turbidity flows. Thus a self-recycling process established in which sediment was temporarily deposited on the levee but eventually conveyed through the failures zone and flushed down-system. This style of levee failure exerts a first-order control on channel morphology. If slumped levees plug the channel axis, avulsion may occur and reroute sandy flows. A fascinating stratigraphic consequence of these deep-seated failures is the violation of the Law of Superposition in which older strata overlie younger strata. This study contributes to the understanding of the coupled process of sedimentation-driven excess fluid pressure and slope failure in channel-levee systems, which are the major constructional elements on the world’s deep sea fans and common energy exploration targets.

Chapter 2

Retrogressive Failures Recorded in Mass Transport Deposits in the Ursa Basin, northern Gulf of Mexico

ABSTRACT

Clay-rich Mass-Transport Deposits (MTDs) in the Ursa Basin, Gulf of Mexico, record failures that mobilized along extensional failure planes and transformed into long runout flows. Failure proceeded retrogressively: scarp formation unloaded adjacent sediment causing extensional failure that drove successive scarp formation updip. This model is developed from 3-D seismic reflection data, core and log data from Integrated Ocean Drilling Project (IODP) Expedition 308, and triaxial shear experiments. MTDs are imaged seismically as low-amplitude zones above continuous, grooved, high-amplitude basal reflections, and are characterized by two seismic facies. A Chaotic facies typifies the downdip interior, and a Discontinuous Stratified facies typifies the headwalls/sidewalls. The Chaotic facies contains discontinuous, high-amplitude reflections that correspond to flow-like features in amplitude maps: it has higher bulk density, resistivity, and shear strength, than bounding sediment. In contrast, the Discontinuous Stratified facies contains relatively dim reflections that abut against intact pinnacles of parallel-stratified reflections: it has only slightly higher bulk density, resistivity, and shear strength than bounding sediment, and deformation is limited. In both facies, densification is greatest at the base, resulting in a strong basal reflection. Undrained shear tests document strain weakening (sensitivity = 3). I estimate that failure at 30 meters below seafloor will occur when overpressure = 70% of the hydrostatic effective stress: under these conditions soil will liquefy and result in long runout flows.

2.1 INTRODUCTION

MTDs are the products of large mass failures that typically transport hundreds of km^3 of material downslope. MTDs are composed of the deposits of slides, slumps, and debris flows (Stow, 1986; Weimer and Shipp, 2004). They can occur throughout a margin's history, in all water depths, and over a range of bed slopes from steep (oceanic island flanks, ~10°) to very gentle (Mississippi delta, <0.5°) (Booth et al., 1993; Hampton, 1996; Masson et al., 2006; McAdoo et al., 2000; Moscardelli et al., 2006; Urgeles et al., 1997). MTDs play an important role in the development of continental margins and oceanic island flanks, and often comprise greater than 50% of the stratigraphic rock record in these settings (Garziglia et al., 2008; McMurtry et al., 2004; Newton et al., 2004). Hazards, including tsunamis, coastal erosion, and impacts on subsea cables, wellheads, and other structures can result from MTDs (Bardet et al., 2003; Hampton, 1996; Masson et al., 2006; Weimer and Shipp, 2004). MTDs have generated deadly and destructive tsunamis in Papua New Guinea, Norway, France, and the Aleutian Islands (Dan et al., 2007; Fryer et al., 2004; Tappin et al., 2001). Offshore oil and gas companies routinely model potential slide pathways and analyze conditions that drove past failures (Brand et al., 2003; Butenko and Barbot, 1980; Corthay II and Aliyev, 2000; Jeanjean et al., 2003; Niedoroda et al., 2003; Pirmez, 2004). MTDs are a drilling challenge because they are generally denser than non-deformed sediments (Piper et al., 1997; Prior et al., 1984; Shipp et al., 2004).

Seismic, core, and outcrop studies have each illuminated a wide range of MTD characteristics. Outcrop studies (Lucente and Pini, 2003; Lucente and Pini, 2008) have demonstrated the internal structure of MTDs. Core studies (Jenner et al., 2007; Moscardelli and Wood, 2008; Tripsanas et al., 2008) have illuminated variable lithofacies recorded in MTDs. Seismic studies have illuminated the wide range of geomorphologic elements of MTDs (Gee et al., 2006; Homza, 2004; Jenner et al., 2007; Lucente and Pini, 2003; Lucente and Pini, 2008; Martinez et al., 2005; Moscardelli and Wood, 2008; Moscardelli et al., 2006; Posamentier, 2003; Tappin et al., 2001; Tripsanas et al., 2008). Ocean Drilling Program Leg 155 on the Amazon Fan and Integrated Ocean Drilling Program (IODP) Expedition 308 in the Gulf of Mexico collected rock properties data through MTDs (Flemings et al., 2006; Piper et al., 1997). *Piper et al.,* [1997] presented a comprehensive analysis of the Amazon fan MTDs but they lacked high-resolution seismic data to link facies with rock properties.

IODP Expedition 308 cored, logged, and sampled several MTDs in the first 600 meters below seafloor (mbsf) in the Ursa Region of the northern Gulf of Mexico [*Flemings et al.,* 2006]. A high-resolution 3-D seismic volume (~20 km^2), shot specifically for shallow hazard analysis, provides detailed imagery of the internal architecture of MTDs. The log and core data of IODP Expedition 308, together with the industry seismic data, represent a unique opportunity to better understand the properties of MTDs, to explore their relationship to seismic facies, and to ultimately illuminate the underlying processes associated with MTDs.

I link seismic response, rock properties from core and log, and triaxial shear experiments to develop a conceptual and quantitative model of the multi-stage process of failure and post-failure evolution of failures recorded in clay-rich MTDs in the Ursa Basin. I first present a detailed well-seismic correlation and correlate between the wells across the drilling transect. I then characterize the seismic-core-log attributes of MTDs at Ursa and interpret my observations in terms of failure, transport, and depositional processes of clay-rich MTDs. I close by inferring how these MTDs initiated and evolved to their current state.

2.2 REGIONAL SETTING AND SEISMIC DATA

The Ursa Basin lies 210 km (~125 miles) southeast of New Orleans, Louisiana (USA), on the Mississippi Fan, in water depths from 800-1500 meters (2600-4900 ft.) (Fig. 2.1). Late Pleistocene deposits in the Ursa Basin are associated with a much larger system in north-central Gulf of Mexico (Coleman and Roberts, 1988; McFarlan and LeRoy, 1988; Winker and Booth, 2000). Winker and Booth (2000) termed this the Eastern Depositional Complex. These strata accumulated in the last ~70 ka during Marine Isotope Stages (MIS) 1-4 during the Late Wisconsinan North American continental glaciation (Li et al., 2007; Winker and Booth, 2000; Winker and Shipp, 2002).

I focus on the sediments within the first 600 mbsf within the Ursa Basin (Fig. 2.2). Winker and Shipp [2002], Flemings et al., [2006], and Sawyer et al., [2007a] describe the regional stratigraphy of these deposits. They can be divided into four successive depositional units: the Blue Unit basin-floor fan, the Ursa Canyon channel-levee system, the Southwest Pass Canyon channel-levee system, and distal fan and hemipelagic deposits (Fig. 2.2). MTDs lie primarily within the levee sections of the Southwest Pass and Ursa channel systems. The Blue Unit is an overpressured, sand-rich, formation that has caused significant problems during drilling when unconsolidated sand has flowed to the seafloor (Ostermeier et al., 2002; Ostermeier et al., 2000; Pelletier et al., 1999).

The high resolution 3-D seismic data used here were acquired with 80 in^3 sleeve gun array (TriCluster 80), with four 100m streamers towed from a single vessel, 0.5 ms digitization, and inline and trace spacing of 7.5 m and 6.25 m, respectively. Data are zero phase with frequency content of 150 Hz or higher. Vertical resolution is thus on the order of 3 meters. I use a black/white color convention with white representing a positive impedance contrast (e.g., the seafloor is white). These data were processed with an automatic gain control (AGC) filter of 100 ms. Amplitudes in separate AGC windows are thus not directly comparable to each other and appropriate caution must be taken when interpreting amplitude variations across AGC windows. In this study the amplitude variations associated with MTDs are relatively small and lie within the same AGC window for a given MTD. Furthermore, the logging and coring data provide excellent means to verify the observed amplitude differences.

2.3 RESULTS

2.3.1 Well Tie

I use a vertical seismic profile completed at Site U1324 to define a time-depth model and correlate core and log data with seismic data. Sixteen time-depth pairs, spanning the region from 84 to 499 mbsf, were acquired [*Flemings et al.,* 2006]. I assume this velocity-depth profile describes the velocity structure beneath the entire cross section and use it to depth convert the seismic data (Fig. 2.2). As the sediment properties are similar to a depth of 250 mbsf at all sites (including all MTDs), I am confident in using the same time-depth model. The lithology and velocity structure in the lowermost 300 mbsf at Site U1324 is unique to this site; therefore extrapolations to other sites between 300-600 mbsf may not be as robust. Table 2.1 presents key seismic surfaces in both two-way travel time and depth.

Site U1324 is composed of two lithologic units: Unit I and Unit II as defined by IODP Expedition 308 (Flemings et al., 2006) (Fig. 2.3). Unit I extends from 0-365 mbsf and is composed of clay and silt; Unit II is composed of interbedded silt, sand, and clay and it ranges from 365 – 604 mbsf (Fig. 2.3). Seismic reflection S40-1324 lies at the boundary of these two lithofacies. Reflections between the seafloor and S40-1324 are generally parallel and continuous, and are controlled by relatively minor changes in bulk density and/or velocity (Fig. 2.3). The prominent seismic reflection, S30, corresponds to a thin layer of relatively low velocity, low resistivity, and high porosity at the base of MTD-2 (Figs. 2.2 and 2.3). Below S40-1324, the response of the seismic, gamma ray, resistivity, velocity, and bulk density logs are more variable (Fig. 2.3). This is due in part to the variable lithology (interbedded sand, silt, and clay) but also because of some hole-washout shown by the caliper log (Fig. 2.3). The reflections in this interval are not laterally continuous (Fig. 2.2).

No core was collected at Site U1323; however, LWD logs were collected to 247 mbsf (Fig. 2.4). Three units were defined [*Flemings et al.,* 2006]. Logging Unit 1 extends from the seafloor to 197 mbsf and is interpreted to be dominated by mud with several silty intervals and two MTDs (Fig. 2.4). At the top of Logging Unit 2 there is a sharp decrease in the gamma ray and resistivity, which I interpret to be a sand (Fig. 2.4). Logging Unit 2 cannot be correlated to Site U1324 or Site U1322. In Logging Unit 3, gamma ray values increase with depth, which suggests an increase in clay content with depth (Fig. 2.4). Seismic reflections are discontinuous in this interval. At the base of Logging Unit 3 (242 mbsf), a high-amplitude reflection correlates with a low gamma ray response, which I interpret as a sand (Fig. 2.4).

Site U1322 is composed ubiquitously of mud and the majority of the section is composed of MTDs (Fig. 2.5). Grain size does not change significantly with depth (Fig. 2.5). However, the resistivity, density, porosity, and shear strength are quite variable. Each zone of increased resistivity corresponds to a zone of increased bulk density and shear strength: in core and seismic data, these zones are shown to correspond to MTDs.

The abrupt increase in density at the base of each MTD is recorded with a prominent negative (black) reflection.

2.3.2 Age and Correlation

The base of the Blue Unit onlaps a regionally extensive condensed section, which contains the extinction events of the planktonic foraminifera *Globorotalia flexuosa* (70 ka) and the calcareous nannofossil *Pontosphaera 1* (~70 ka) (Styzen, 1996; Winker and Booth, 2000). The age of top of the Blue Unit is unknown. IODP Expedition 308 cored to within ~20 meters of the top of the Blue Unit at Sites U1324 and U1322 and recovered sediments younger than 57 ka [*Flemings et al.,* 2006].

At Site U1324, age markers of 48, 42, 24, 16, and 10 ka were identified (Fig. 2.3). These correspond to the boundaries between planktonic foraminifera subzones Y5/Y4, Y4/Y3, Y3/Y2, Y2/Y1, and Y1/Z, respectively (Flemings et al., 2006; Kennett and Huddlestun, 1972). At Site U1322, only age markers 57 ka, 24 ka, 16ka, and 10 ka, were identified (Fig. 2.2). However, the 57 ka and 24 ka markers are tentative because they were recovered within MTDs.

I correlate the above timelines across the transect with the exception of the 48 ka and 42 ka timelines because they were not identified at Site U1322 (Fig. 2.2). The 24 ka age marker is robust at Site U1324 and ties to a foraminifera-rich bed (*G. conglobatus*), which correlates to seismic reflection S30. This foraminifera-rich bed was not recovered at Site U1322, but I can correlate S30. It is likely that the foraminifera-rich bed was eroded by the MTD at Site U1322, therefore the correlation at Site U1322 is tentative (dashed line in Fig. 2.2a). The 57 ka marker was not identified at Site U1324, but I correlate the 57 ka timeline from Site U1322 to Site U1324 by the downhole profiles of relative abundance of calcareous nannofossils [*Flemings et al.,* 2006].

2.3.3 Mass Transport Deposits

MTDs at Ursa are imaged as low-amplitude zones between a high-amplitude, negative, basal reflection and a low-amplitude, positive, top reflection (Figs. 2.2-2.5) (Dugan et al., 2007b; Sawyer et al., 2007b; Urgeles et al., 2007). The sidewalls of MTDs are marked by the abrupt, steep truncation of channel-levee deposits (Fig. 2.2). I define 10 MTDs (MTDs 1- 10) based on these criteria (Table 2.2). MTD-2 is a large, multi-detachment, mass failure that extends beyond the limits of the seismic data. In contrast, MTDs 3-10 contain a single detachment, are thinner and aerially smaller than MTD-2, and lie completely within the eastern levee of the Ursa Canyon channel system.

I begin my analysis of MTDs by presenting a detailed description of the most prominent MTD at Ursa, MTD-2. I present its large-scale, seismic geomorphology, and then focus in on the details of log and core behavior. I then explore the stacked set of MTDs at Site U1322 (MTDs 3-10).

I focus on the changes in bulk density that occurred in the MTDs and how this has impacted other physical measurements. I describe the change in bulk density through the bulk density equation:

$$\rho_b = \phi\rho_f + (1-\phi))\rho_g, \qquad \text{eq. 1}$$

where ϕ is porosity, and ρ_f and ρ_g are the fluid and grain density, respectively. When LWD bulk density data are expressed in terms of porosity or void ratio (e), I have assumed in all cases that ρ_f = 1024 kg/m^3 and ρ_g = 2740 kg/m^3 (Sawyer et al., 2008). I will discuss changes in porosity in terms of both porosity and void ratio (e), where:

$$e = \frac{\phi}{1-\phi}. \qquad \text{eq. 2}$$

2.3.4 MTD-2

The top and base of MTD-2 correspond to seismic surfaces S20 and S30, respectively (Fig. 2.2). The base of MTD-2 is a complex surface, with multiple detachment levels and grooves (Figs. 2.2 and 2.6). The grooves occur on the eastern side and trend southeast, indicating the failure direction (Fig. 2.6). They extend for at least 1 km, and are up to 5 meters deep. The top of MTD-2 has two appearances in map view: a dimpled texture in the western half, and a relatively smooth surface along the eastern half (Fig. 2.7). The dimpled texture corresponds to the tops of pinnacle features that I discuss in the next section.

2.3.4.1 Seismic Facies of MTD-2

Within MTD-2, I identify two seismic facies: 1) Chaotic, and 2) Discontinuous Stratified (Figs. 2.8 and 2.9, respectively). I summarize each facies and their attributes in Table 2.3. In seismic cross section, the Chaotic facies contains high-amplitude, discontinuous reflections (Fig. 2.8).

The Discontinuous Stratified facies contains discontinuous reflections that abut against cone-shaped islands (“pinnacles”) of parallel stratified reflections (Fig. 2.9). Each pinnacle sticks above the surrounding material by a few meters and each is attached to the base of MTD-2. The pinnacles are distributed around Site U1324 as illustrated on the dip map of the top of MTD-2 (S20) (Fig. 2.7). The dip angle of the sidewalls ranges from ~50°-60°. The basal reflection (S30) has higher amplitudes beneath the discontinuous reflections and is dimmer beneath the pinnacles (Fig. 2.9). Each pinnacle is upright and I observed no overturned or detached pinnacles. Furthermore, there are no grooves along the base of MTD-2 beneath the pinnacles.

Within the Discontinuous Stratified facies, there is a faulted slump block that lies between Sites U1324 and U1323 (Fig. 2.10). A steep sidewall scarp, between Sites U1324 and U1323, truncates the western edge of this block from the thick section of parallel seismic reflections of the Southwest Pass Canyon levee. The eastern toe of this slump block ramped up above the lower detachment surface and extruded onto the intermediate detachment level, and its top was eroded. The western half of the block contains extensional faults, and the eastern half contains compressional faults (Fig. 2.10). Similar zones of extension and compression within slumps have been observed in outcrops in Ireland (Martinsen and Bakken, 1990).

Figure 2.11 illustrates the spatial distribution of the two facies. The high amplitude zone in the eastern part of the map corresponds to the Chaotic facies whereas the low amplitudes to the west correspond to the Discontinuous Stratified facies. Site U1322 and U1323 penetrated the high-amplitude region and Site U1324 penetrated the low-amplitude region.

2.3.4.2 Petrophysics, Sedimentology, and Physical Properties of MTD-2

At Site U1322, MTD-2 corresponds to the prominent zone of increased resistivity, bulk density, and shear strength (88 – 125 mbsf) (Figs. 2.5 and 2.12). In cores, MTD-2 is composed of deformed mud, with occasional folds, mud clasts, and no discernible bedding (Flemings et al., 2006) (Fig. 12). The base is a sharp contact that separates deformed, dark-brown mud above from bedded, light-brown clay below (Fig. 2.12E). The high degree of deformation at Site U1322 is pervasive throughout MTD-2, with the exception of the top 5 m, where it is gradational and less intense (Fig. 2.12B).

The bulk density is greater within MTD-2 than the bounding sediment (Fig. 2.12A). The correspondence of the LWD-derived porosity with the measured porosity (Fig. 2.12) confirms that the densification is driven by loss of pore space. The greatest densification (lowest porosity) occurs in the basal ~20 meters and densification declines upward to background values in the top 17 meters. I quantify the degree of densification by observing that the porosity above and below MTD-2 is approximately constant ($\phi_0 =$ 51%): I assume this baseline porosity (ϕ_0) represents the porosity that would be present at this depth if there were no MTD present. I calculate the porosity difference ($\Delta\phi = \phi_0 - \phi$) where ϕ is the porosity within the MTD. The maximum densification is marked by a change in porosity ($\Delta\phi$) of 0.10 units: this occurs about 8 meters above the base (Fig. 2.12). Shear strength (Fig. 2.12A) is proportional to the densification, and is greatest at the base.

The densification within MTD-2 controls the seismic response: the densification, and thus the impedance contrast, is greatest at the base, therefore the basal reflection is high-amplitude and negative polarity (high impedance to low impedance) (Figs. 2.8 and 2.12). The internal reflections are chaotic and have locally high amplitudes because of the variations in impedance within the MTD itself (Figs. 2.8 and 2.12). The top reflection has an opposite polarity from the basal reflection because the impedance contrast increases with depth.

At Site U1323, MTD-2 contains a prominent zone of increased resistivity and low porosity (91 -195 mbsf) (Fig. 2.4). The densification is fairly constant in the basal ~95 meters, and declines upward to background values only in the upper ~6 meters. The bulk density log decreases at the base; however, this is likely related to poor hole conditions as recorded by the caliper log (Flemings et al., 2006). There are high amplitude reflections of the slump block as well as transparent zones similar to Site U1322. The basal reflection is high amplitude and negative polarity (high impedance to low impedance), internal reflections are low amplitude, and the top reflection has lower amplitude than the base and an opposite polarity (positive; low impedance to high impedance).

At Site U1324, MTD-2 correlates to a zone of slightly increased resistivity and velocity, and slightly lower porosity (107-165 mbsf) (Figs. 2.3 and 2.13). The densification is highest in the basal 15 m, and declines to background values towards the top. The maximum $\Delta\phi$ is 0.07 porosity units, which occurs 15 m above the base. In core, MTD-2 contains only minor deformation features including small-offset faults and slightly tilted bedding (Fig. 2.13). Most of the deformation features are observed near the bottom of the MTD. The base, at 165 mbsf, is recorded by a color change from reddish brown clay above to dark brown clay below. This bed is enriched in foraminifera (*G. conglobatus*) and is identified by low velocity, high porosity, and low resistivity in the logs (Figs. 2.3 and 2.13). The seismic response is similar to that at Sites U1322 and U1323: the basal reflection has high amplitude due to the high impedance contrast (high impedance to low impedance) and the top reflection has an opposite polarity and lower amplitude. The internal reflections of MTD-2 at Site U1324 are unique from the other sites and are associated with the Discontinuous Stratified facies (as discussed above).

2.3.4.3 Strain in MTD-2

The incremental volumetric strain (ε_v) (compression is positive) is,

$$\varepsilon_v = \frac{\Delta e}{1+e_o}, \qquad \text{eq. 3}$$

where *e* is void ratio within the MTD and e_0 is baseline void ratio (ϕ_0 expressed as void ratio). Within MTD-2 at Site U1322, maximum ε_v is +12%, and the mean is +4% (Fig. 2.12). At Site U1324, maximum ε_v is +9%, and the mean is +2% (Fig. 2.13). Thus, the volume strain in MTD-2 at Site U1322 is twice that at Site U1324. In both cases the volume strain increases with depth within MTD-2.

I calculate vertical strain between the pinnacles and surrounding sediment by calculating the height difference. I assume the pinnacles have undergone no strain and represent the original thickness. In seismic data, I measured an average height difference of 3 meters between several pinnacles and their surrounding sediment. The average thickness of the pinnacles is 58 meters and consequently the vertical strain is 5% (positive values indicate compression). This value for vertical strain, which was derived near Site U1324, is quite similar to the average volumetric strain found from petrophysical data at Site U1324 (4%). This suggests that strain may have been largely uniaxial within the MTD. There is a progressive increase in height difference between pinnacles and surrounding sediment eastward away from Site U1324 towards the main side scarp. This suggests that vertical strain within MTD-2 increases eastward from Site U1324.

2.3.5 MTDs 3-10 at Site U1322

The high-amplitude reflections in the lower half of Site U1322, below seismic surface S30, correspond to a stacked set of 8 MTDs (MTDs 3-10) (Figs. 2.2 and 2.5). MTDs 3-7 are very thin (~3-20 meters) at Site U1322 and are difficult to distinguish from each other because of the high amplitude basal reflections; they thicken to the west where they are easier to map individually (Fig. 2.2). Each MTD correlates to a zone of increased resistivity, density, and shear strength between 141 - 234 mbsf (Dugan et al., 2007a; Flemings et al., 2006) (Figs. 2.2 and 2.5). In core, each MTD appears as homogeneous, highly deformed mud bounded by thin intervals of non-deformed mud. MTD-10 contains a smaller secondary MTD with identifiable headwall and sidescarps (Fig. 2.14) (Sawyer et al., 2007a). The distance between the sidewall scarps increases to the southeast, indicating a southeastern transport direction. The similarity of these MTDs to the more clearly imaged MTD-2 suggests that all the MTDs have a similar petrophysical behavior where each MTD is densified relative to its bounding sediment.

2.4. DISCUSSION

2.4.1 History of MTDs at Ursa

MTDs at Ursa developed within an evolving leveed-channel system. MTD-10 was the first failure at Ursa (post-Ursa Canyon) (Fig. 2.15). It records the total failure of the levee that flanks the eastern side of the Ursa Canyon. I interpret that the failure occurred relatively late in the history of Ursa levee deposition because of the thick levee deposits that it eroded. MTD-10 created a bathymetric low that trapped the 7 successive MTDs that followed (MTD-9 through MTD-3) (Fig. 2.15). MTDs 3-10 were relatively small events. The Southwest Pass Canyon system (west of the study area) deposited thick levees, which capped MTDs 3-10 [*Sawyer et al.,* 2007a] (Fig. 2.15). MTD-2 was a large failure on the continental slope that formed within the levee material of the Southwest Pass Canyon system. MTD-2 formed three different detachment levels within the area of the drilling transect alone.

2.4.2 Origin and Evolution of MTDs: Active Failure and Retrogression

I use the observations at Ursa to develop a conceptual and quantitative model to describe the failure and post-failure evolution of MTDs. I envision five stages: 1) initial failure creates an open scarp, 2) extensional active failure occurs behind the open scarp, 3) as strain accumulates the soil weakens, 4) the soil becomes weaker than the gravitational driving stress and flows downslope, and 5) uniaxial consolidation occurs after the fluidized material is arrested.

The initial failure of the slope could have been generated by either high seepage forces in response to high sedimentation rates (Bishop, 1973; Dugan and Flemings, 2000; Elverhoi et al., 1997; Iverson et al., 1997; Terzaghi, 1956), tectonic forcing, or seismic activity (Brodsky et al., 2003; Hampton, 1996; Morgenstern, 1967; Schwab et al., 1988)

(Fig. 2.16A). In the Ursa region, I interpret seepage forces and fluid overpressures are the dominant mechanisms for slope instability but seismic activity has also been recorded in the Gulf of Mexico (Dugan and Germaine, 2008; Flemings et al., 2006; Flemings et al., 2008; Urgeles et al., 2007).

The horizontal stress adjacent to the newly formed scarp is reduced, which reduces the mean effective stress and increases the shear stress. Failure caused by lateral unloading is termed Rankine active failure (Lambe and Whitman, 1969). Failure surfaces lie at 45° + $\frac{\phi_f}{2}$ to the plane on which the greatest principal stress acts (Fig. 2.16B), where ϕ_f is the internal angle of friction (Lambe and Whitman, 1969). At Ursa, ϕ_f is ~25°, thus active failure planes should be oriented at 57.5° and I observe ~50°-60° failure surfaces (Fig. 2.9).

To illustrate how the landslide mass is transformed from Rankine active failure to generalized flow, I examine the stress path of the soil during its evolution in a plot of mean effective stress (p') vs. mean stress difference (q) (Fig. 2.17a). During sedimentation, consolidation is uniaxial (K_0 conditions) ('0' to '1', Figs. 2.16B and 2.17A). Then, lateral stress (σ_3') is reduced and shear increases until Rankine active failure occurs ('1' to '2', Fig. 2.17B). The effective stress path first curves up to the peak strength (pt. '2', Fig. 2.17A) and then down to the left indicating both decreasing shear strength and decreasing mean effective stress. The decrease in mean effective stress is caused by contractive behavior during shear, which elevates the pore pressure as it takes on more of the total load (Iverson, 2005). Ultimately, the soil reaches critical state where it can continuously deform at constant volume, constant effective normal stress, constant shear stress, and constant strain rate (pt. '3', Fig. 2.17). The degree of strain-weakening is described by the Sensitivity, S_t, which is the ratio of peak undrained strength to critical state strength for a soil at a given water content and confining stress (Lambe and Whitman, 1969).

Undrained triaxial tests document strain weakening in Ursa sediment (Dugan and Germaine, 2009). These data suggest that there is as much as 5% axial strain before peak strength is reached. In all of the Ursa triaxial experiments, soil weakens beyond peak strength; however, critical state strength was not reached before tests were stopped at <20% axial strain (Dugan and Germaine, 2009). Shipboard measurements of the ratio of peak vane shear strength to the remolded strength can also be used to estimate the degree of strain weakening. The shipboard estimates show that S_t is between 2-3 (Flemings et al., 2006).

I re-plot one experimental effective stress path (TX 778 from Dugan and Germaine, 2009) during undrained shearing to simulate landsliding at Ursa (Fig. 2.18). I do not know the pore pressure (and thus vertical effective stress) that existed at failure, however I do know the present-day conditions (Dugan and Germaine, 2008; Flemings et al., 2008). It is likely that pore pressure was greater in the past than at present as sedimentation rates have decreased at Ursa over the last 10 ky (Flemings et al., 2006). I investigate three cases determined by the initial overpressure ratio, λ^* (λ^* is the ratio of the overpressure to the hydrostatic vertical effective stress): 1) present-day conditions where λ^* is 0.5 (Dugan and Germaine, 2008; Flemings et al., 2008), 2) $\lambda^* = 0.7$, and 3) $\lambda^* = 0.9$. I calculate the gravitational driving stress (τ_g) assuming a 2-D infinite slope with slope-parallel seepage (Graham, 1984):

$$\tau_g = (S_v - P_h)\sin\theta\cos\theta, \qquad \text{eq. 4}$$

where S_v and P_h are the total overburden stress and hydrostatic pore pressure, respectively. τ_g is 4.4 kPa at 30 mbsf on a typical slope (θ) in the Ursa Basin of 1.5°, constrained from seismic data. Figure 2.18 illustrates several important points. First, only the case of $\lambda^* = 0.9$ results in a topographic driving stress that is greater than the in-situ shear stress under K_0 conditions. However, even with this high pore pressure, the driving stress is less than the shear strength. If fact, an overpressure ratio of 0.92 would be necessary to instigate sliding given an infinite slope of 1.5 degrees and a friction angle of 25.8°, given in this experimental result. This result parallels previous work that have noted the extreme pore pressures necessary to generate slope failure (Coleman and Prior, 1988; Prior and Suhayda, 1979; Terzaghi, 1956). Second, retrogressive failure due to lateral unloading can only occur if there is significant soil sensitivity. For the examples shown here, for an initial pore pressure ratio of 0.5, the sensitivity must be equal to 6 whereas if the initial pore pressure ratio is 0.7, then the sensitivity need only be equal to 3.

In sum, I infer that a high pore pressure ratio ($\lambda^* \geq 0.7$) was necessary to initiate failure. To generate subsequent retrogressive failure, strain weakening, as expressed by significant soil sensitivity, transforms slope failures to long runout flows. Failure can proceed provided that the gravitational driving stress is greater than the critical state strength (Fig. 2.17) (Kayen et al., 1989; Poulos, 1981; Poulos et al., 1985; Schwab, 1988; Whitman, 1985). This allows the material to flow at the shear stress levels imposed by the regional topographic gradient without any other requirements and moves downslope for tens even hundreds of kilometers based on other studies of submarine debris flows (De Blasio et al., 2005; Elverhoi et al., 1997; Garziglia et al., 2008; Gee et al., 1999; Jansen et al., 1987; Laberg and Vorren, 2000; Masson et al., 1998; Masson et al., 1997; Mohrig et al., 1998; Niedoroda et al., 2003).

An additional mechanism, not explored here, that could contribute to decreasing the soil strength below the topographic driving stress is the long-term effect of pore pressure rise following scarp formation (Bishop and Bjerrum, 1960; L'Hereux et al., in press; Leroueil, 2001). This effect is commonly observed in excavations in normally consolidated clays where total mean stress and pore pressure drop in response to undrained unloading. Over time, pore pressure rises and slope stability decreases, which can potentially drive slope failure. An intriguing aspect of this process is that it provides an additional mechanism to drive retrogressive failure: if the undrained response does not weaken soil strength below the gravitational driving stress, the subsequent pore pressure rise could progressively weaken the soil until it does.

2.4.3 Deposition and Densification of MTDs

Experiments in subaerial and subaqueous debris flows document that high excess pore pressures are maintained throughout movement, and dissipate primarily after movement is arrested (Ilstad et al., 2004; Iverson, 1997; Major, 1996; Major, 2000; Major and Iverson, 1999; McArdell et al., 2007). Movement is arrested, presumably by a change in topographic gradient. Today the MTDs are denser than bounding sediment (Flemings et al., 2006) (Figs. 2.3-2.5). I interpret that prior to slope failure, the soil had a metastable 'cardhouse' structure, typical of normally consolidated marine clays (Mitchell, 1993). During slope failure and subsequent transport, the soil is mechanically 'remolded.' Remolding deflocculates and reduces porosity of the soil at constant water content (Mitchell, 1993). Experimental work has shown that if a natural sample and its remolded version are uniaxially consolidated to an equivalent vertical effective stress, the remolded soil has a lower porosity (higher bulk density) (Burland, 1990; Chandler, 2000; Skempton, 1970). Not only is the original structure remolded, but a shear-induced fabric develops in which grains are aligned with long axes parallel to the direction of shear. Anisotropy of magnetic susceptibility (AMS) and scanning electron microscope (SEM) images record alignment of clay particles in Ursa MTDs (Yamamoto et al., 2005). I attribute the densification and shear fabric of Ursa MTDs to remolding during downslope transport and deformation. Upon re-deposition, the MTD uniaxially consolidates, and because it is remolded, consolidates to a lower porosity for a given vertical effective stress than normally deposited soil above and below the MTD (see porosity offset at basal contact of MTD-2 in Fig. 2.13).

2.4.4 Linking Seismic Facies with Sedimentology and Physical Properties

We show that MTDs are denser than their bounding material and that densification is coincident with deformation (Figs. 2.12 and 2.13). Densification is greatest near the base of the MTD and it declines upwards. This accounts for the prominent basal reflection and the weak upper reflection observed in seismic. Within the MTD, extensive deformation results in a low-reflectivity internal character in seismic. *Piper et al.,* (1997) also described the correspondence between transparent seismic zones and MTDs in the Amazon Fan. The Amazon Fan MTDs are ~50 meters thick with similar $\Delta\phi$ as the Ursa MTDs [*Piper et al.,* 1997]. Similarly, a common interpretation in sequence stratigraphic literature is that transparent zones are MTDs (Posamentier and Kolla, 2003; Weimer, 1990; Weimer and Shipp, 2004).

A surprising outcome of this analysis is that strong seismic reflections and large excursions in resistivity record densification and not lithologic variation (e.g. Fig. 2.5). As a result, I am able to correlate MTDs with resistivity logs and this may result in a new methodology for mapping and interpreting MTDs from logs. Resistivity changes do not always map directly to lithologic contrasts but in this case resistivity maps to densification.

A unique aspect of this study is that I could explore the spatial variation of properties within a single MTD. I documented two facies: Discontinuous Stratified and

Chaotic. I suggest that the Discontinuous Stratified facies records incipient failure within a retrograding slide (Fig. 2.9). In contrast the Chaotic facies is the product of a fluidized submarine gravity flow (Figs. 2.6, 2.8, and 2.11). This facies also has the greatest degree of densification and deformation as observed in cores (Figs. 2.5 and 2.12). MTD-2 contains examples of both types. However, the stacked set of MTDs (3-10) are all characterized by the Chaotic facies and thus I interpret they are fluidized, long runout debris flows.

2.5 CONCLUSIONS

Strong seismic reflections and large excursions in resistivity record densification and not a lithologic contrast within clay-rich MTDs of the Ursa Basin. Densification is greatest near the base and it declines upwards, which controls the prominent basal reflection and the weak upper reflection observed in seismic.

I defined two seismic facies within the MTDs. The Chaotic facies records greater transport based on the observation of grooves and flow-like features. This facies has the highest degree of densification and soft sediment deformation. In contrast, the Discontinuous Stratified facies suggests only limited transport: there are no grooves or flow-like features in seismic, pinnacles contain undeformed sediment that have not moved, and soft sediment deformation is subtle in core.

A high pore pressure ratio ($\lambda^* \geq 0.7$) and strain-weakening were necessary to propagate retrogressive failures in these clay-rich sediments. Failure of material can proceed downslope for many kilometers provided that the gravitational driving stress is greater than the critical state strength. The ultimate deposits (MTDs) have a characteristically low porosity relative to bounding sediment. I suggest that the original soil fabric is remolded by the failure process and results in a shear-induced fabric.

2.6 ACKNOWLEDGEMENTS

We thank the scientists and crew on IODP Expedition 308 for their extraordinary efforts. This work was supported by the Penn State Geofluids Consortium (supported by 10 energy companies), the Jackson Chair in GeoSystems, and JOI-USSAC IODP Expedition 308 support to Sawyer and Flemings. This research uses samples and data provided by the Integrated Ocean Drilling Program. The IODP is sponsored by the U.S. National Science Foundation (NSF) and participating countries. Heather Nelson provided editorial assistance. I thank the Consortium for Ocean Leadership and the Integrated Ocean Drilling Program for post-cruise funding. I thank Shell and its Ursa partners for access to seismic data. Finally, I thank Craig Shipp, Roger Urgeles, Roger Bloch, Mike Porter, and members of the UT Geofluids Research group for helpful discussions.

Table 1. Key seismic surfaces

Site U1324	**Water depth = 1056.0 m**	
Surface	**twtbsf (ms)**	**mbsf (m)**
Seafloor	0	0
S10	45	35.5
S20	135	104.5
S30	210	165.8
S40-1324	443	359.2
S50-1324	559	463.7
S60-1324	723	609.3

Site U1323	**Water depth = 1260.5 m**	
Surface	**twtbsf (ms)**	**mbsf (m)**
Seafloor	0	0
S10	44	26
S20	124	91
S30	250	194

Site U1322	**Water depth = 1319.5 m**	
Surface	**twtbsf (ms)**	**mbsf (m)**
Seafloor	0	0
S10	40	31.6
S20	116	88.9
S30	160	124.5
S40-1324	233	181.8
S50-1324	256	202.4
S60-1324	280	221.1
S70-1322	313	245.4

twtbsf (ms) = two-way travel time below seafloor (milliseconds)
mbsf = meters below seafloor (meters)

Table 2. Thickness and seismic facies of Ursa MTDs

MTD	Site U1324 thickness (m)	Site U1323 thickness (m)	Site U1322 thickness (m)	Seismic Facies
MTD-1	**16.1**	**10.1**	**21.2**	Chaotic facies at Sites U1322 and U1323. Discontinuous Stratified facies at Site U1324
MTD-2	**58.0**	**97.4**	**34.0**	Chaotic facies
MTD-3	--	--	**4.9**	Chaotic facies
MTD-4	--	--	**6.3**	Chaotic facies
MTD-5	--	--	**6.3**	Chaotic facies
MTD-6	--	--	**2.9**	Chaotic facies
MTD-7	--	--	**8.5**	Chaotic facies
MTD-8	--	--	**17.1**	Chaotic facies
MTD-9	--	--	**17.8**	Chaotic facies
MTD-10	--	--	**~23.0**	Chaotic facies

Table 3. Summary of MTD seismic facies and related properties.

Seismic Facies	Attributes of base and top reflectors	Internal Features Observed in Seismic Cross Sections	Features Observed in Interval Amplitude Maps	Physical Properties	Deformation Features Observed in Core	Ursa MTDs	Interpreted Type of Mass Movement
Chaotic	**Base**: very high-amplitude, negative reflection coefficient, continuous, often records grooves **Top**: lower amplitude than base, positive polarity, continuous	Local packets of high-amplitude chaotic reflections but otherwise low-reflectivity and semi-transparent	High-amplitude sinuous, channel-like features that correlate to sinuous features observed in cross section	Pronounced increase in bulk density (i.e. lower porosity), resistivity, shear strength relative to bounding non-MTD sediment. Generally greatest towards to the base of MTD.	No preserved bedding, homogeneuous appearance with common folds and rare mud clasts.	Eastern sides of MTD 1 and 2, MTDs 3-10	Debris flow: relatively long run-out, greater internal deformation.
Discontinuous Stratified	**Base**: high-amplitude but dims beneath “pinnacles,” negative reflection coefficient, no grooves **Top**: lower amplitude than base, positive polarity, continuous	Local “pinnacles”of intact parallel stratified reflectors, otherwise discontinuous reflections with low-reflectivity	Low-amplitude, relatively featureless	Minor increase in bulk density (i.e. lower porosity), resistivity, and shear strength relative to bounding non-MTD sediment. Generally greatest towards the base of MTD.	Subtle and recorded as tilted bedding and small-offset faults.	Western sides of MTD-1 and MTD-2	Slump: Relatively short run-out, limited internal deformation.

Table 4. Nomenclature

Symbol	**Definition**	**Dimensions**
ϕ	Porosity	Dimensionless
e	Void ratio	Dimensionless
r_b	Bulk density	$\frac{M}{L^3}$
r_g	Grain density	$\frac{M}{L^3}$
r_f	Fluid density	$\frac{M}{L^3}$
p’	Mean effective stress	$\frac{M}{LT^2}$
q	Mean stress difference	$\frac{M}{LT^2}$
ϕ_f	Friction angle	Dimensionless
$\Delta\phi$	Porosity loss	Dimensionless
Δe	Void ratio loss	Dimensionless
ε_v	Incremental volumetric strain	Dimensionless
$\lambda *$	Overpressure ratio	Dimensionless
$\sigma_1^{'}$	Vertical effective stress	$\frac{M}{LT^2}$
$\sigma_3^{'}$	Horizontal effective stress	$\frac{M}{LT^2}$
θ	Bed slope	Dimensionless
K_0	Coefficient of lateral stress at rest	Dimensionless
P_h	Hydrostatic pressure	$\frac{M}{LT^2}$
S_v	Overburden stress	$\frac{M}{LT^2}$

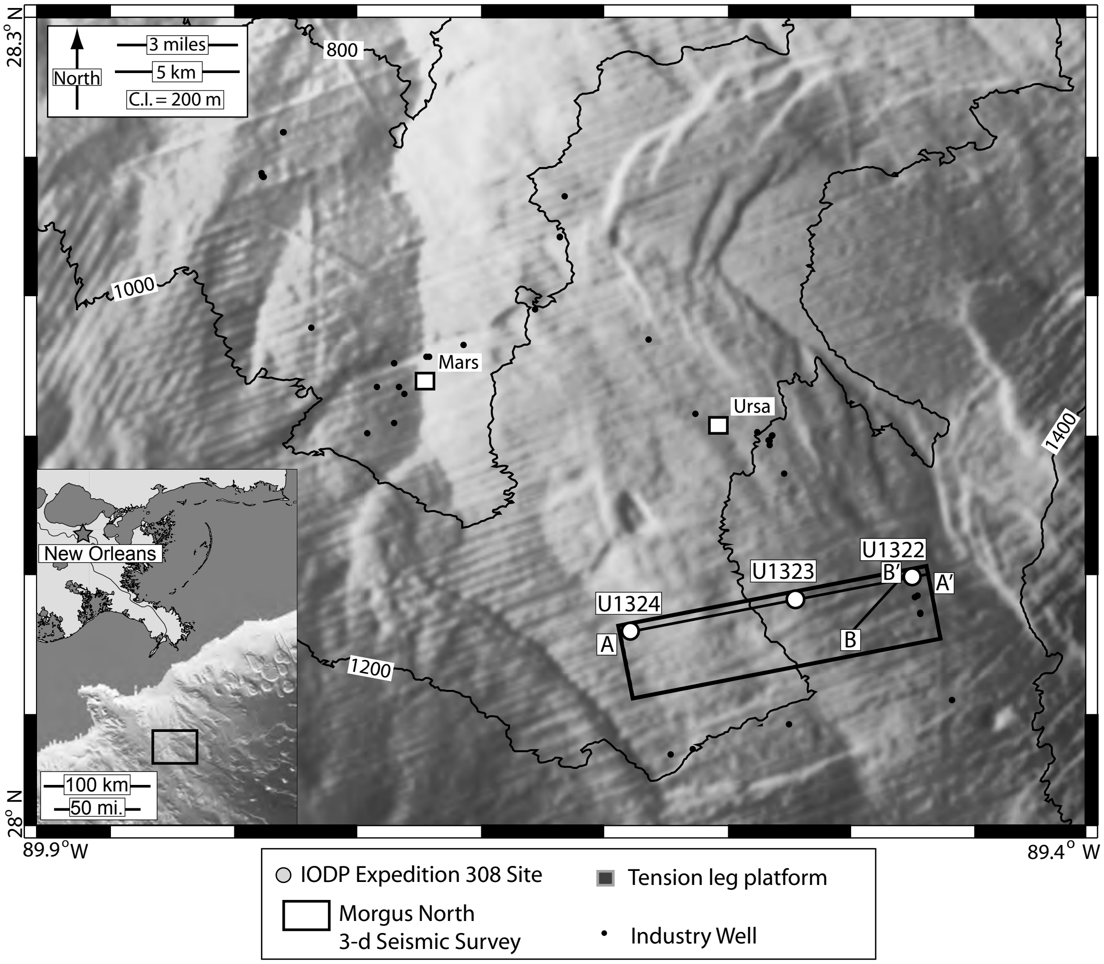

Figure 2.1
The Ursa Region is located 210 km SE of New Orleans, Louisiana, USA (inset map). The IODP drilling transect is located in 1000-1300 meters of water. IODP Sites (circles), 3-D seismic survey (black rectangle), Ursa and Mars tension-leg platforms (squares), and top-hole position industry wells (black dots) are shown.

A

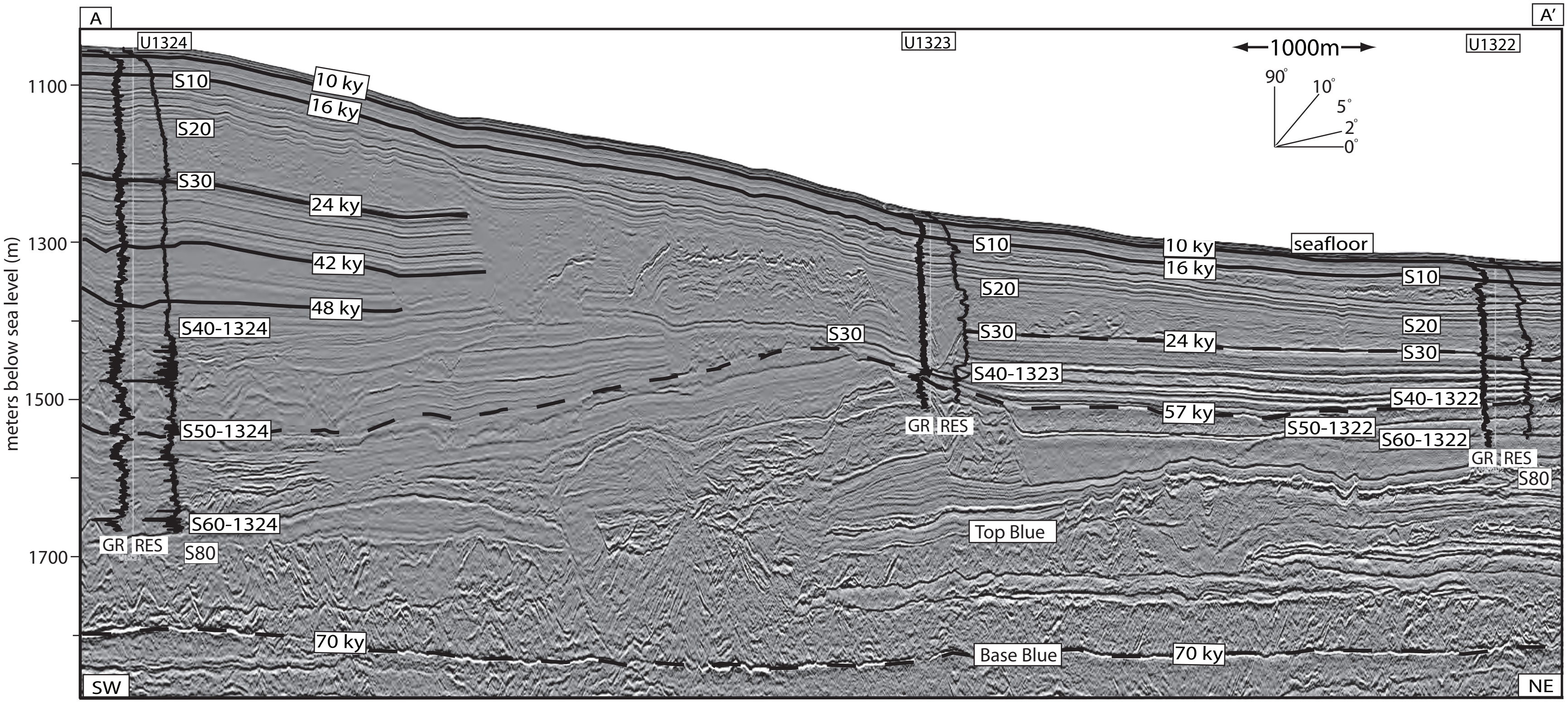

Figure 2.2
A. Depth-converted seismic cross section A-A' tied with IODP Expedition 308 wells. Gamma ray (GR) and resistivity (RES) LWD logs are posted as well as key seismic surfaces. Solid lines represent age-equivalent horizons that have been identified at IODP sites, and dashed lines are tentative timelines.

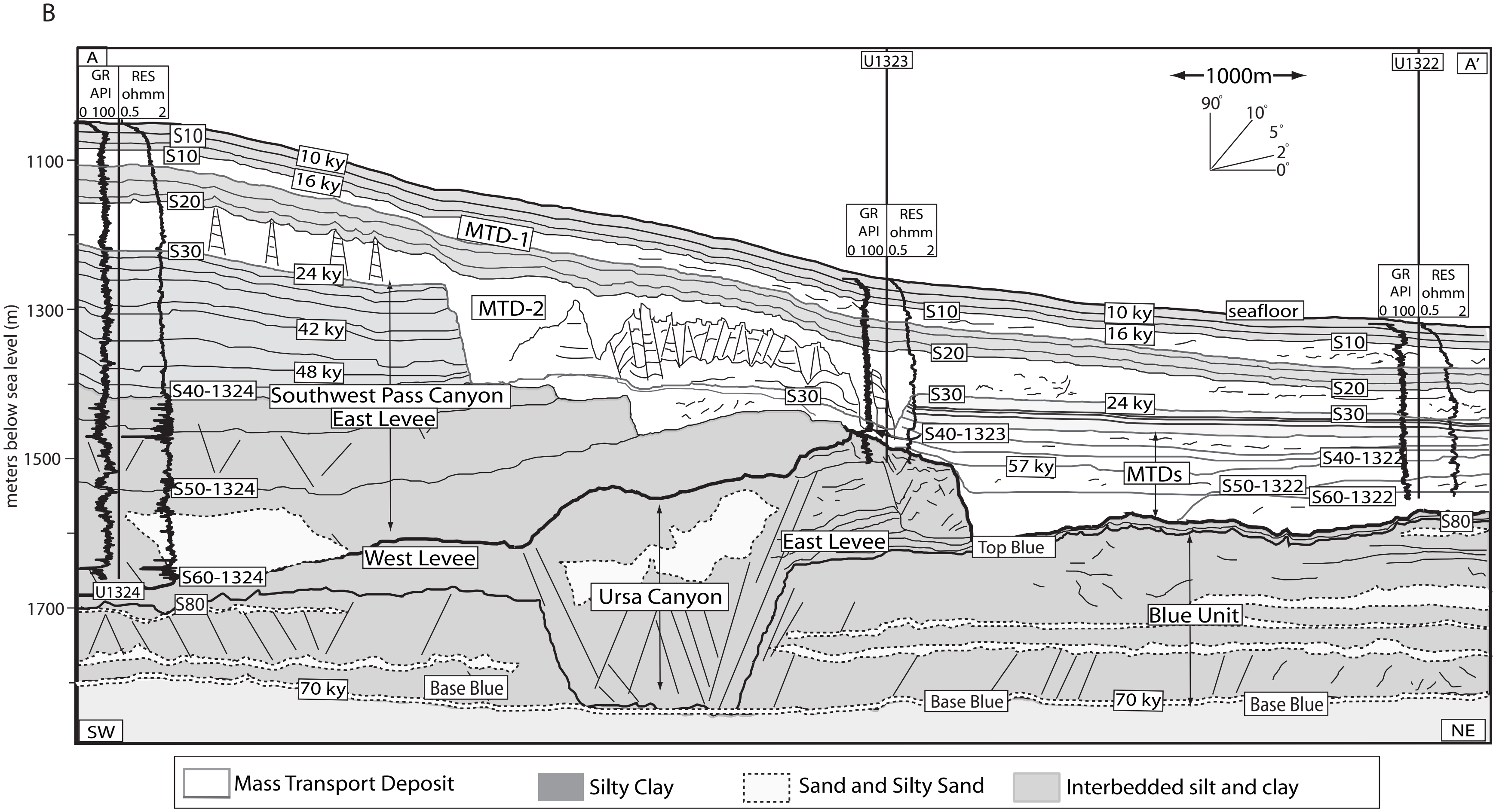

Figure 2.2
B. Interpreted well-log cross-section A-A' illustrating the main depositional units and lithology at Ursa. MTDs occur primarily within the thick silty clay levee deposits.

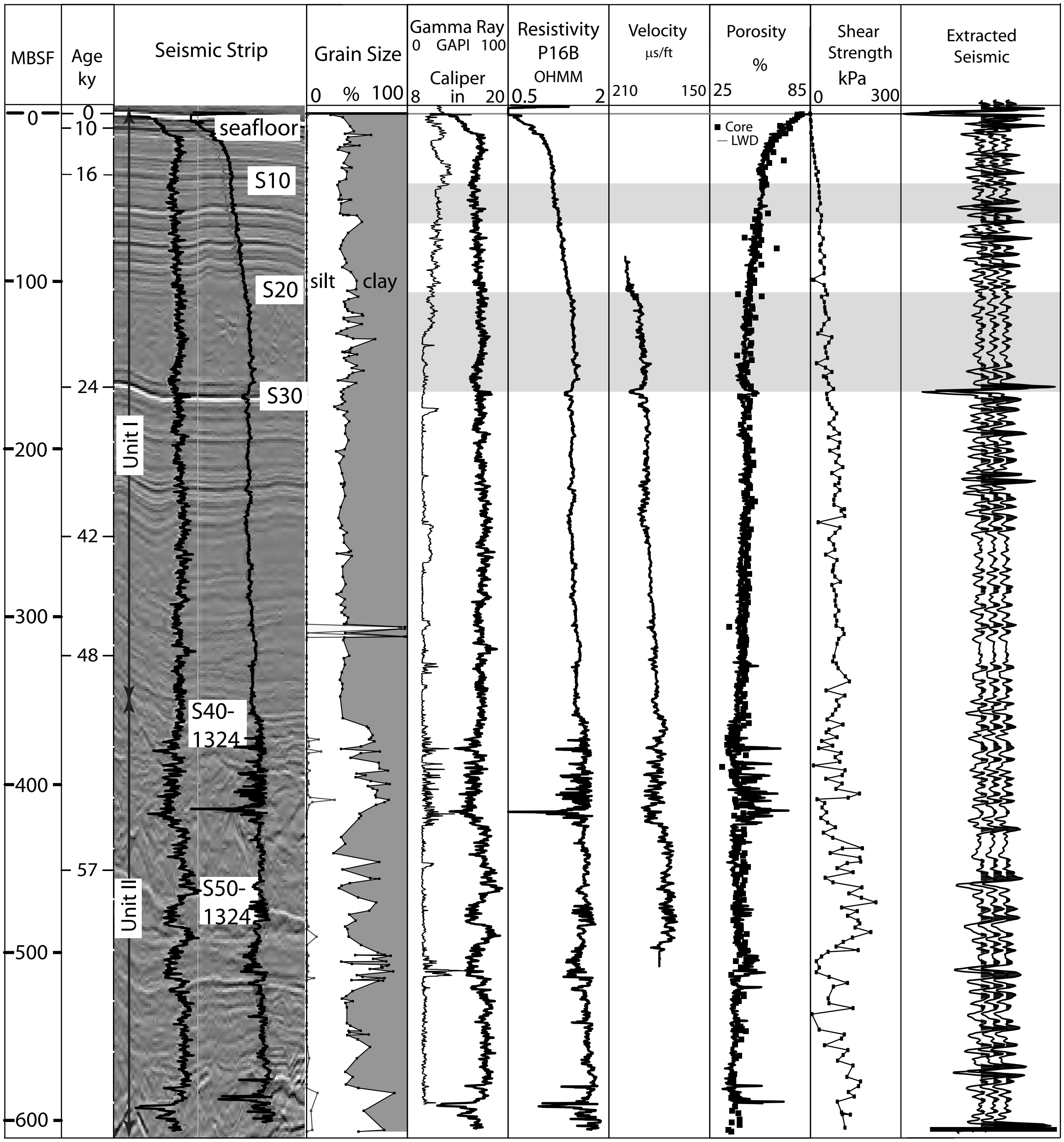

Figure 2.3
Log profile of U1324. Seismic strip from cross section A-A′ with gamma ray and resistivity curves tied to seismic. Log tracks are grain-size data [Sawyer et al., 2008], LWD gamma ray, caliper, resistivity, velocity, porosity (core and LWD-derived), vane peak shear strength, and extracted seismic trace. Log and core data from IODP Expedition 308 (Flemings et al, 2006).

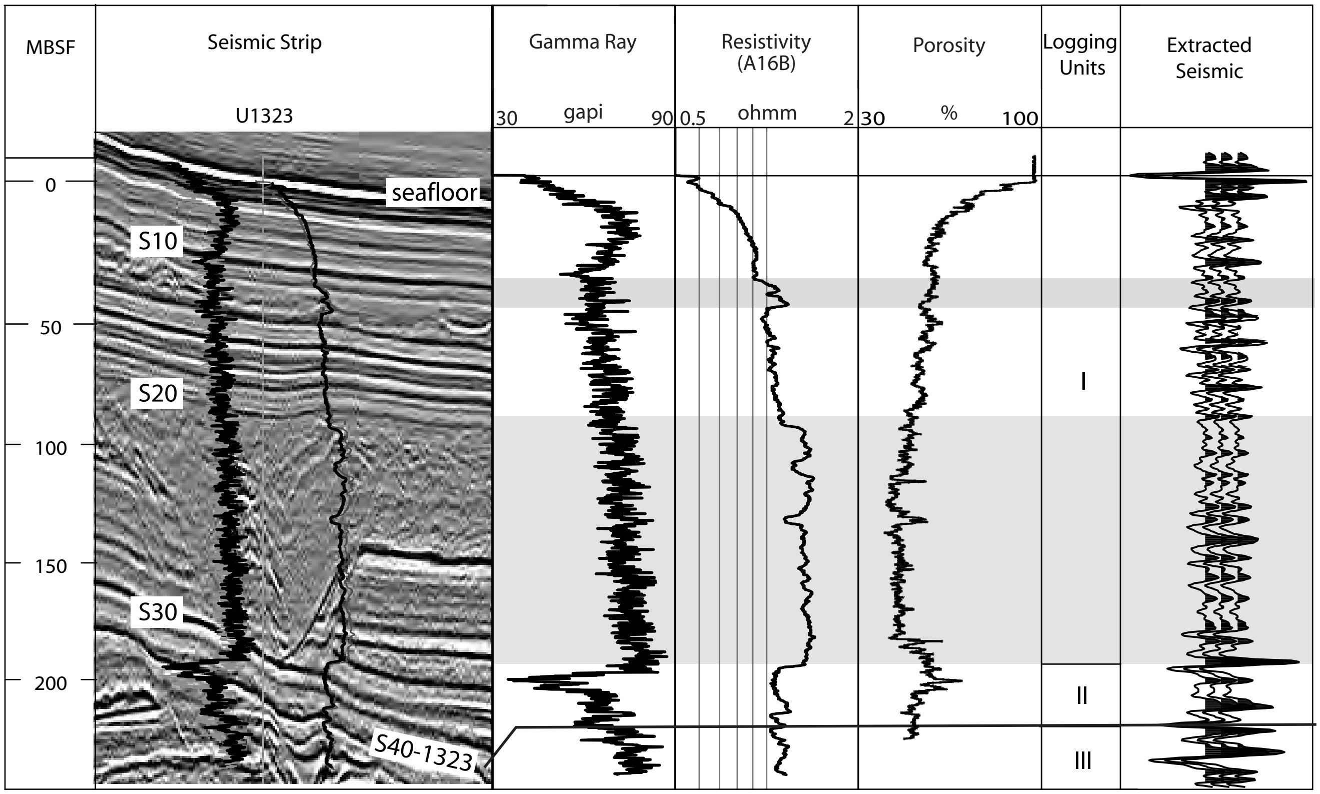

Figure 2.4
Log profile of U1323. Seismic strip from cross section A-A' with gamma ray and resistivity curves tied to seismic. Log tracks are LWD gamma ray, resistivity, porosity (from bulk density log), logging units, and extracted seismic trace. Log and core data and description of logging units from IODP Expedition 308 (Flemings et al, 2006). Log-derived porosity is based on the bulk density log assuming 2740 kg/m3 grain density and 1024 kg/m3 fluid density.

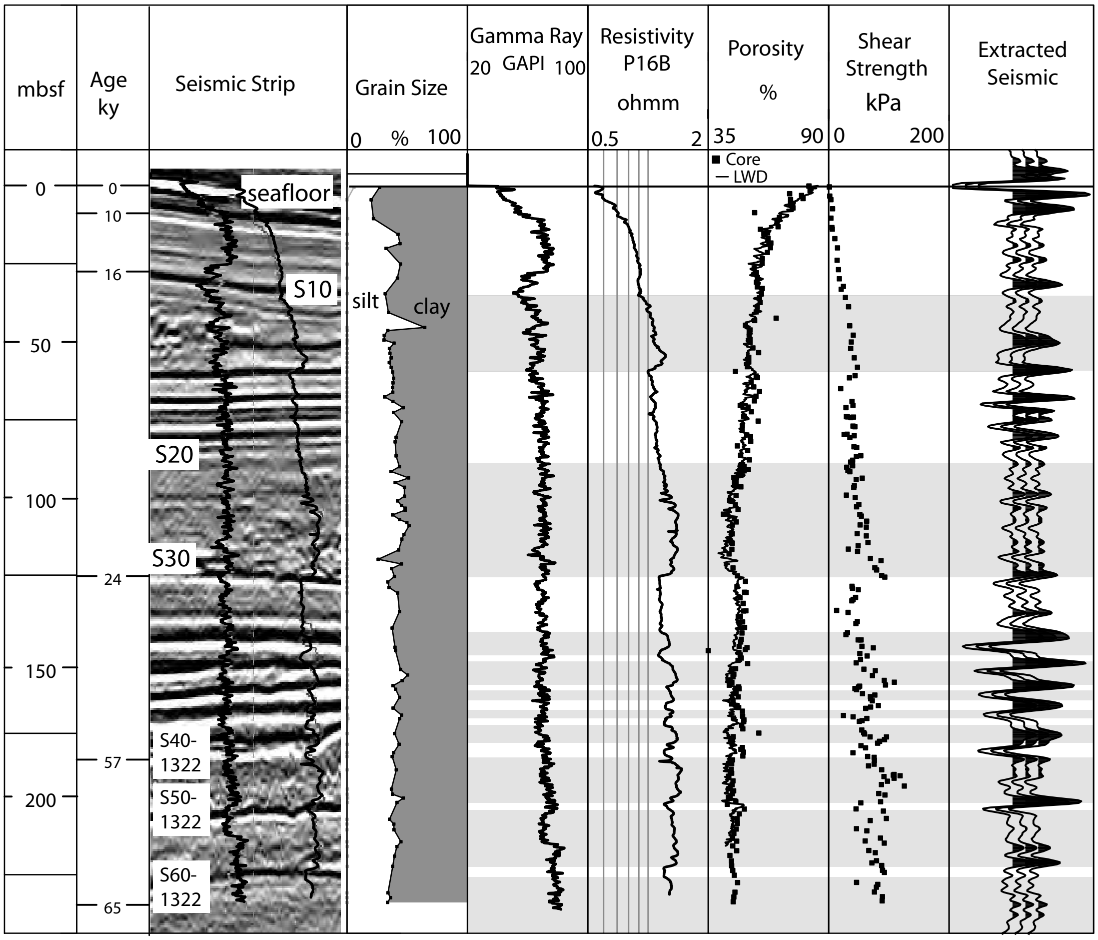

Figure 2.5
Log profile of U1322. Seismic strip from cross section A-A' with gamma ray and resistivity curves tied to seismic. Log tracks are grain-size data [Sawyer et al., 2008], LWD gamma ray, resistivity, porosity (core and log derived), and vane peak shear strength. Log and core data are from IODP Expedition 308 (Flemings et al, 2006).

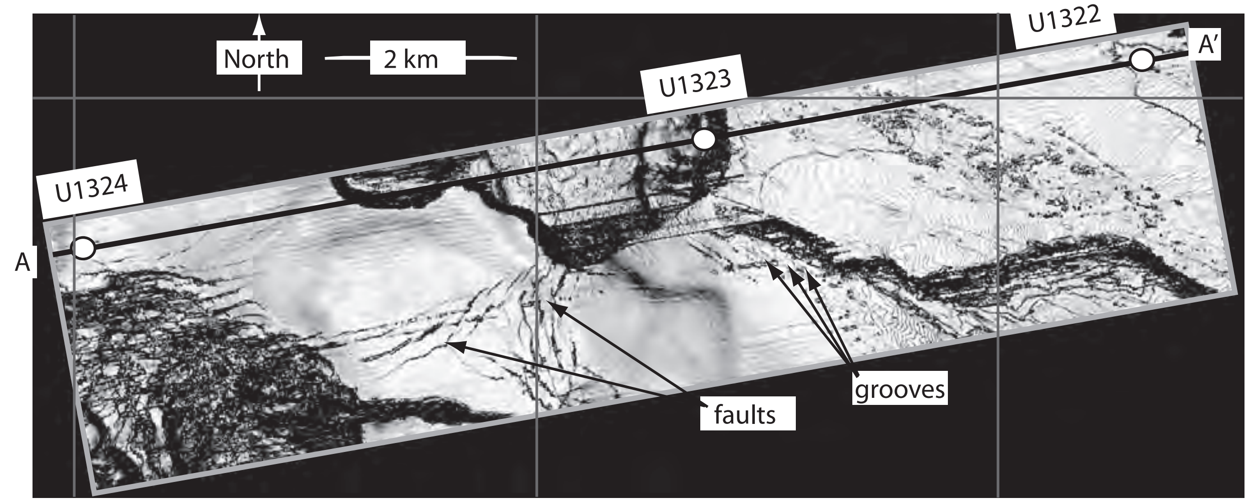

Figure 2.6
Dip map on base of MTD-2, seismic reflection S30 (Fig. 2). Dip map accentuates variations in slope on surfaces (gray is relatively flat and black is relatively steep). Steep sidescarps, linear groove traces, and faults are recorded on the base of MTD-2.

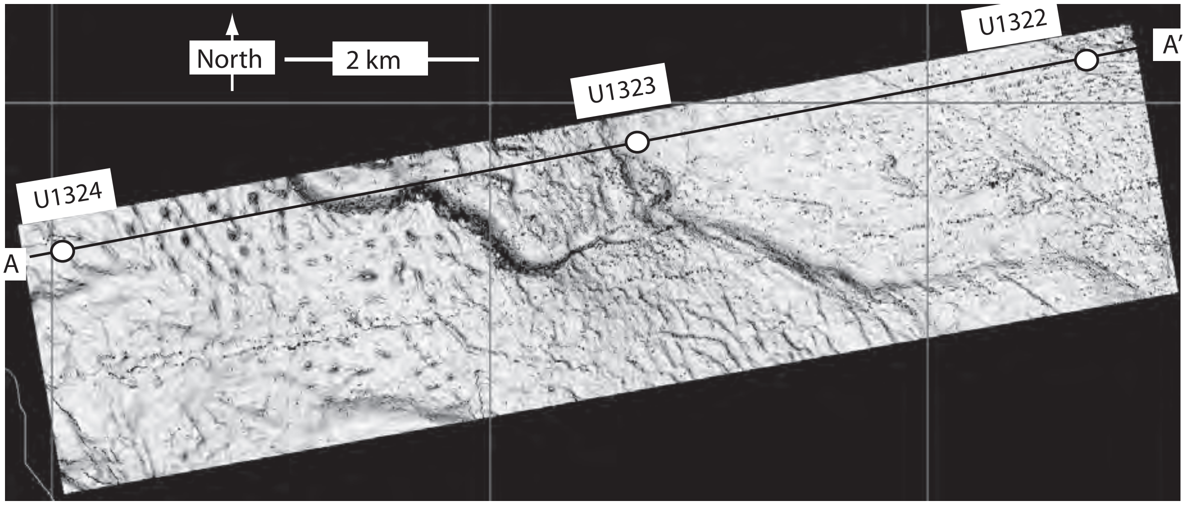

Figure 2.7
Dip map of top of MTD-2, seismic reflection S20 (Fig. 2). The rugose texture in the western half records the tops of pinnacles.

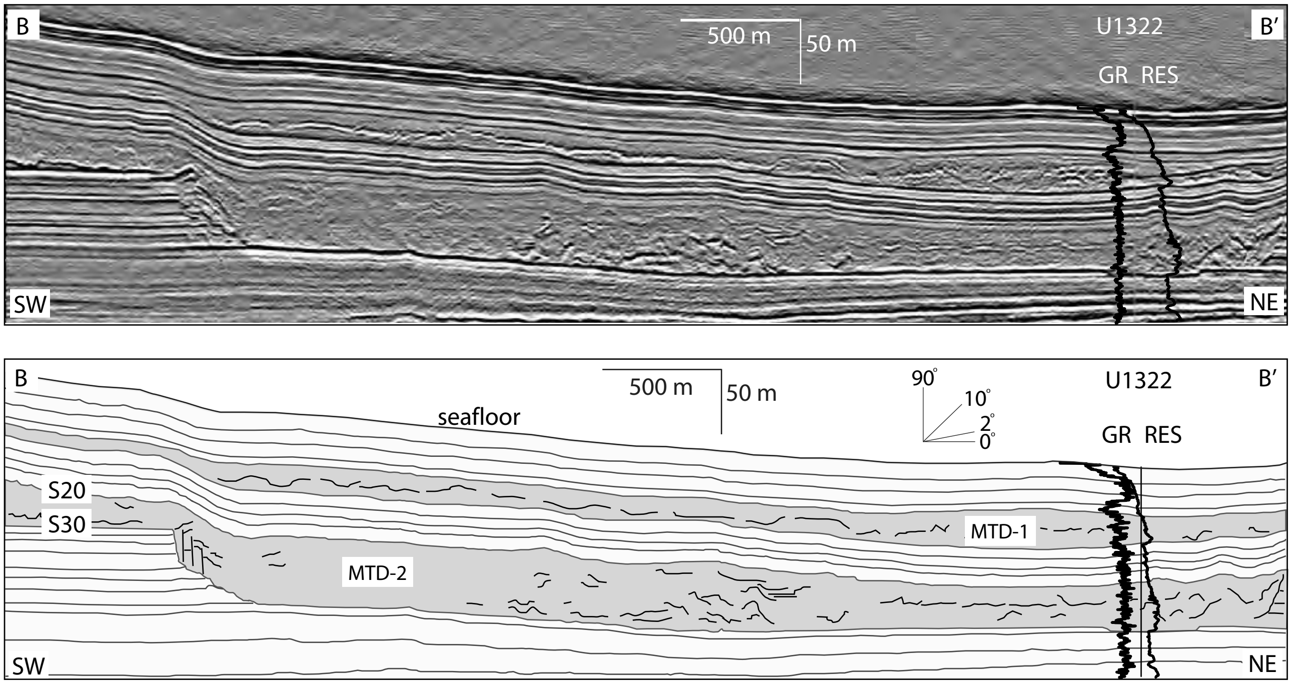

Figure 2.8
Seismic cross section B-B′ illustrating characteristic features of the Chaotic facies. This facies is characterized by local packets of high-amplitude and chaotic reflections within an otherwise low-reflectivity unit. It is present in the eastern areas of MTDs 1 and 2 and all of MTDs 3-10.

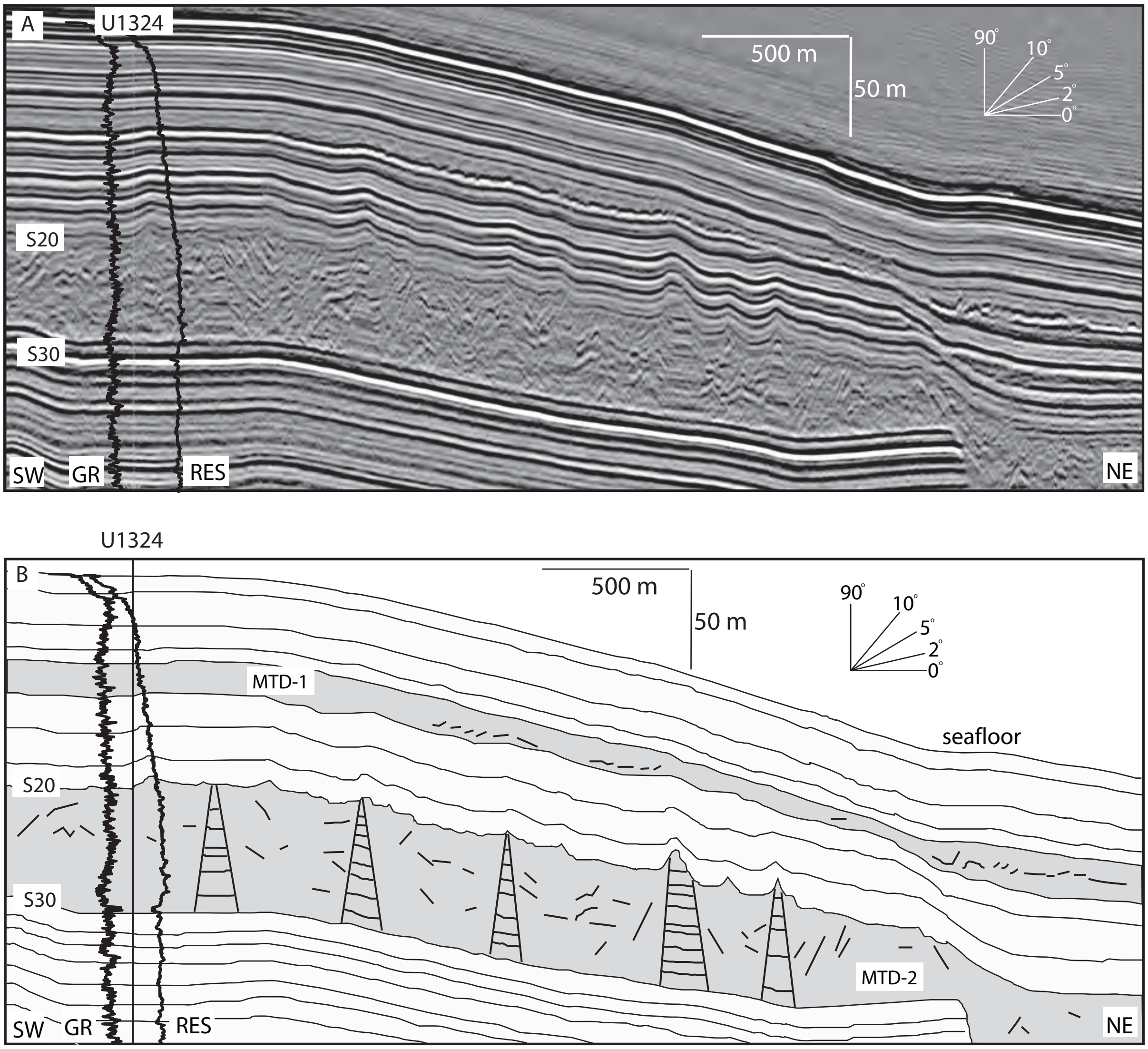

Figure 2.9
A. Close-up of seismic line A-A' illustrating characteristic features of the Discontinuous Stratified facies with pinnacle features near Site U1324. B. Interpreted line. Sidewall angles on the pinnacles range between 45°-60°. Amplitude of the basal reflection, S30, dims beneath the pinnacles. This facies is present in the western areas of MTDs 1 and 2.

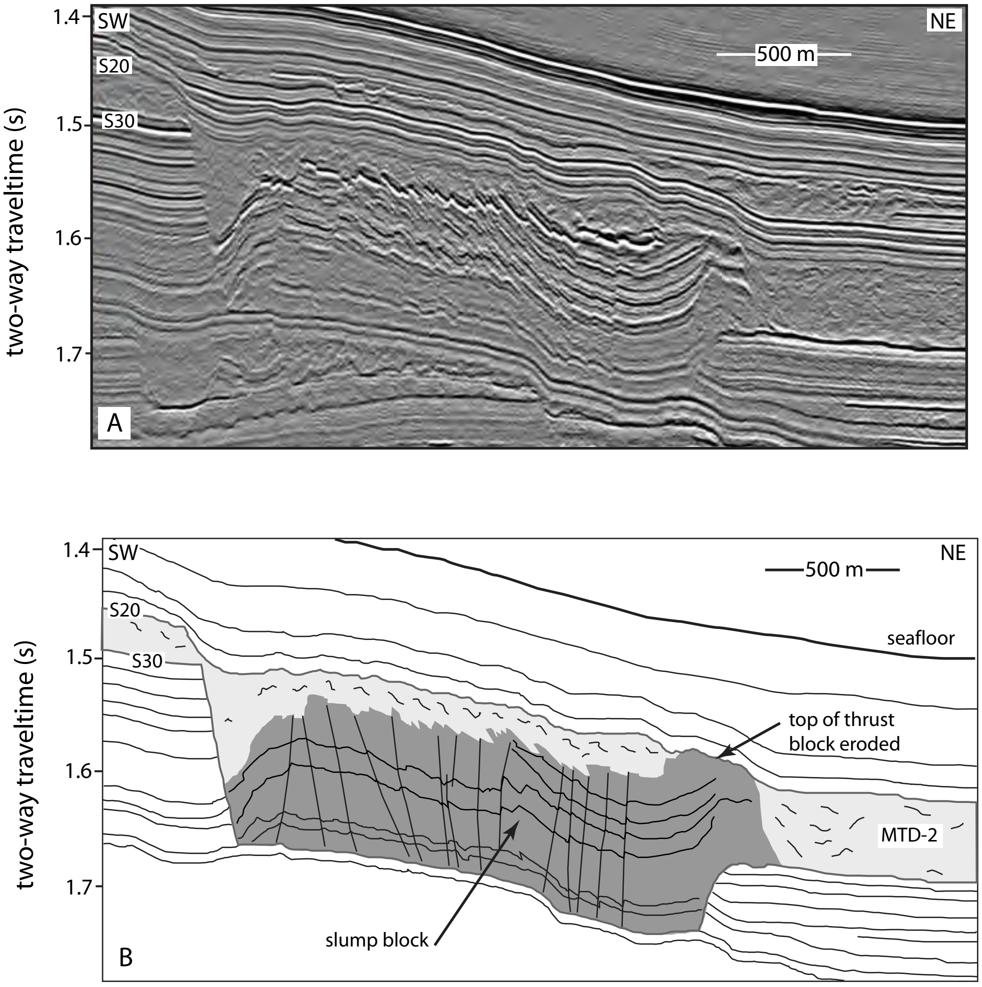

Figure 2.10
A. Close-up of seismic line A-A' illustrating the faulted slump block between Sites U1323 and U1324. B. Interpreted line. This slump block was detached from the steep western sidewall. Internally deformation is recorded extensional faults on the western side and compressional faults on the eastern side.

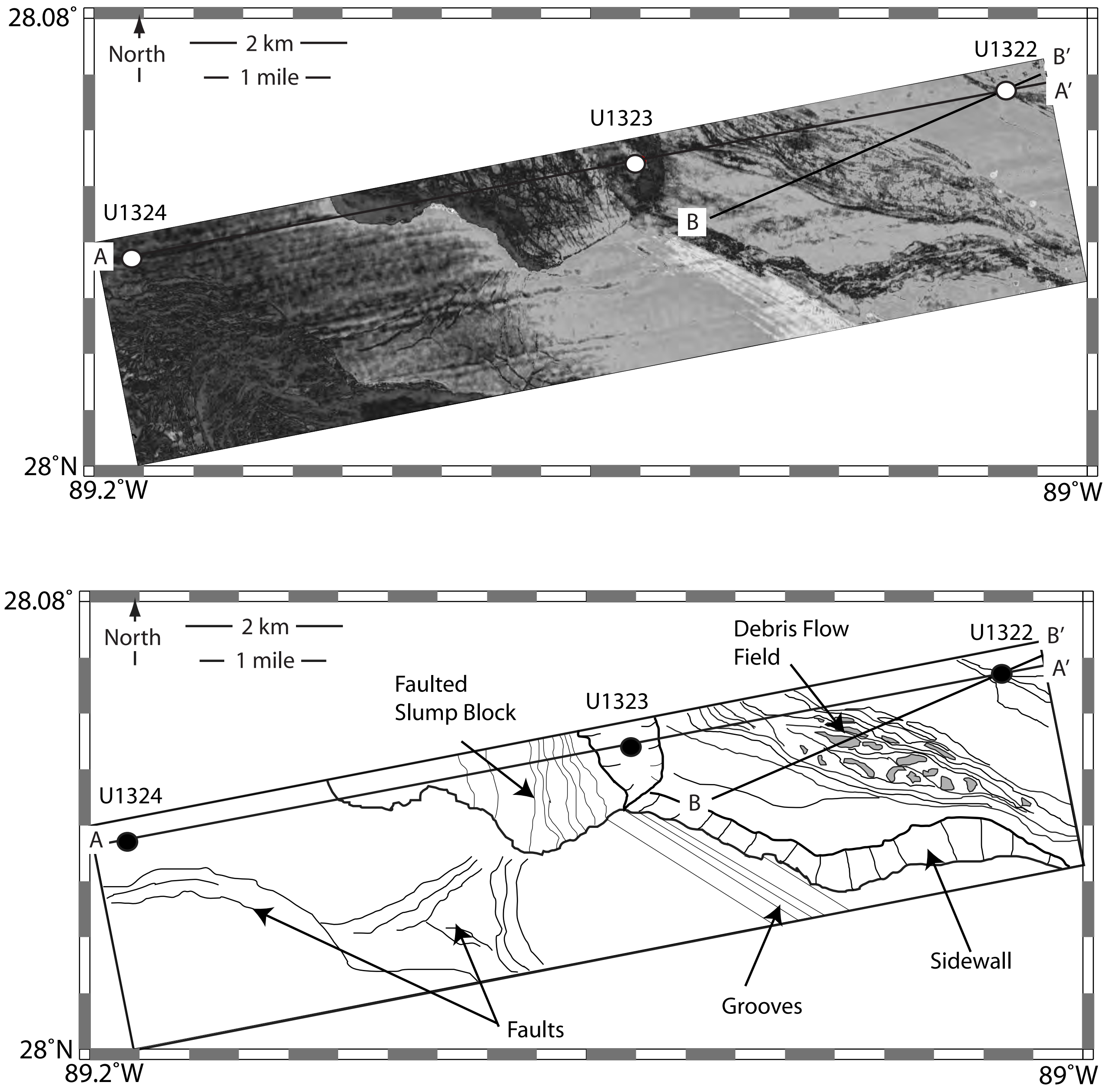

Figure 2.11
Interval amplitude map (root-mean square) of MTD-2. In the east there are sinuous channel-like features that correspond to the Chaotic seismic facies. The western area of MTD-2 is featureless in the amplitude map, and corresponds to the Discontinuous Stratified facies.

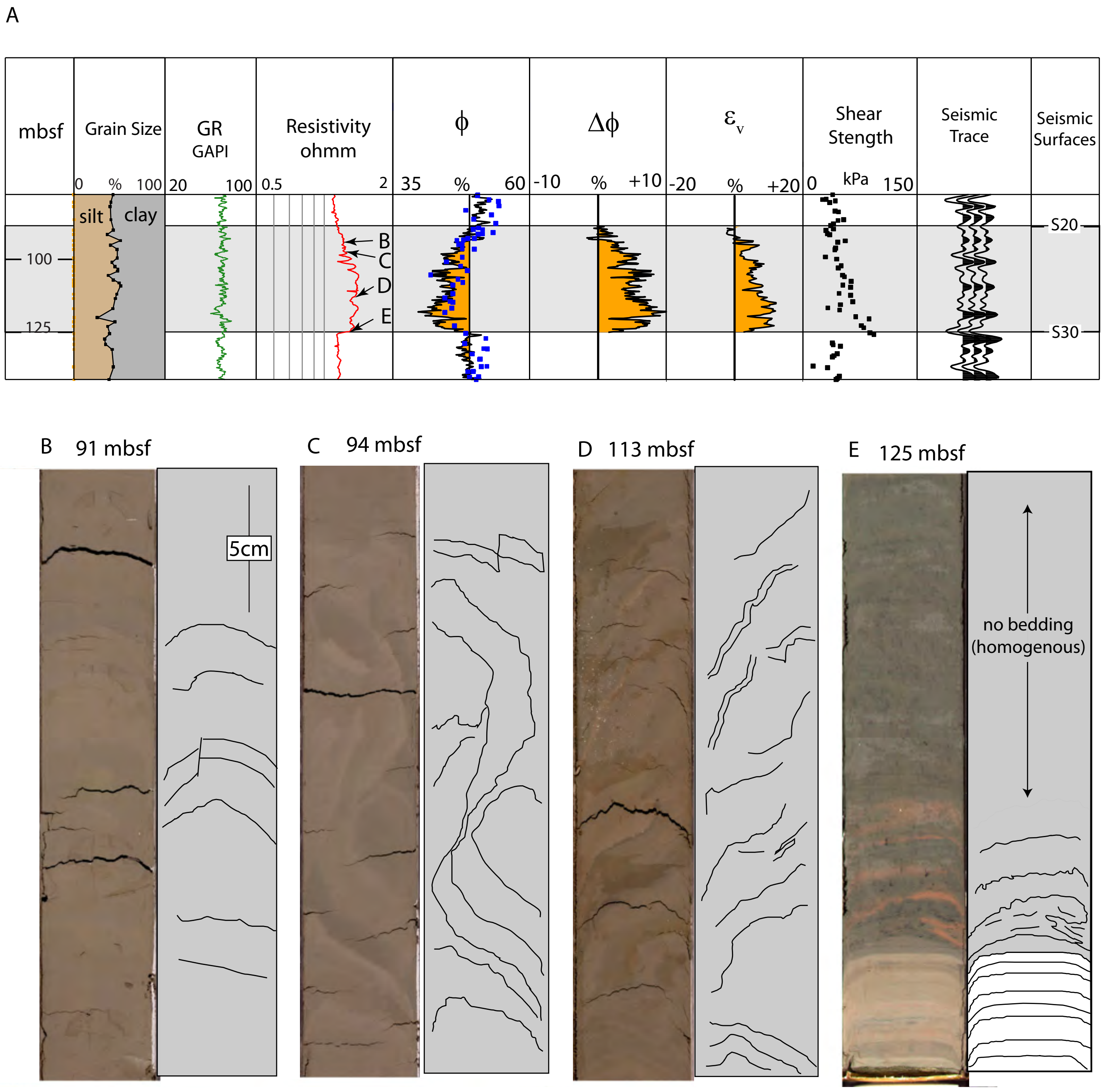

Figure 2.12
A. Log profile through MTD-2 at Site U1322. Incremental volumetric strain (ε_v) is calculated (equation 3) from the porosity loss ($\Delta\phi$) by assuming an original porosity (ϕ) of 0.51 everywhere in the MTD: this approximates the porosity above and below MTD-2. B-E. Core photos from the top (B), middle (C, D) and base (E) of MTD-2 Deformation progressively increases form top to base.

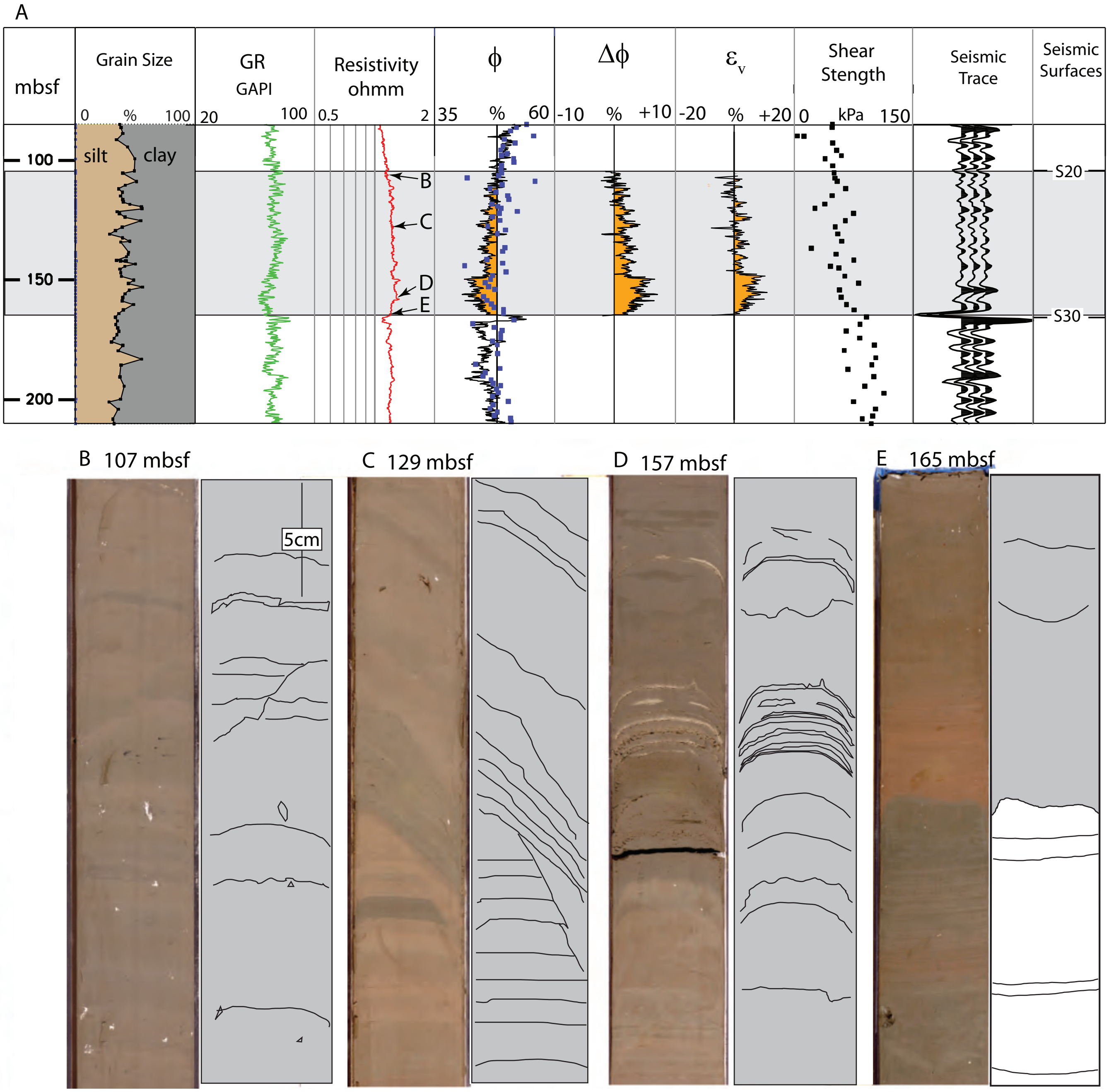

Figure 2.13
A. Log profile through MTD-2 at Site U1324. Incremental volumetric strain (ε_v) is calculated (equation 3) from the porosity loss ($\Delta\phi$) by assuming an original porosity (ϕ) of 0.49. B-E. Core photos document the progression of soft-sediment deformation from the top (B), through the middle (C, D), and to the base (E). The deformation within MTD-2 at this site is subtle compared to Site U1322.

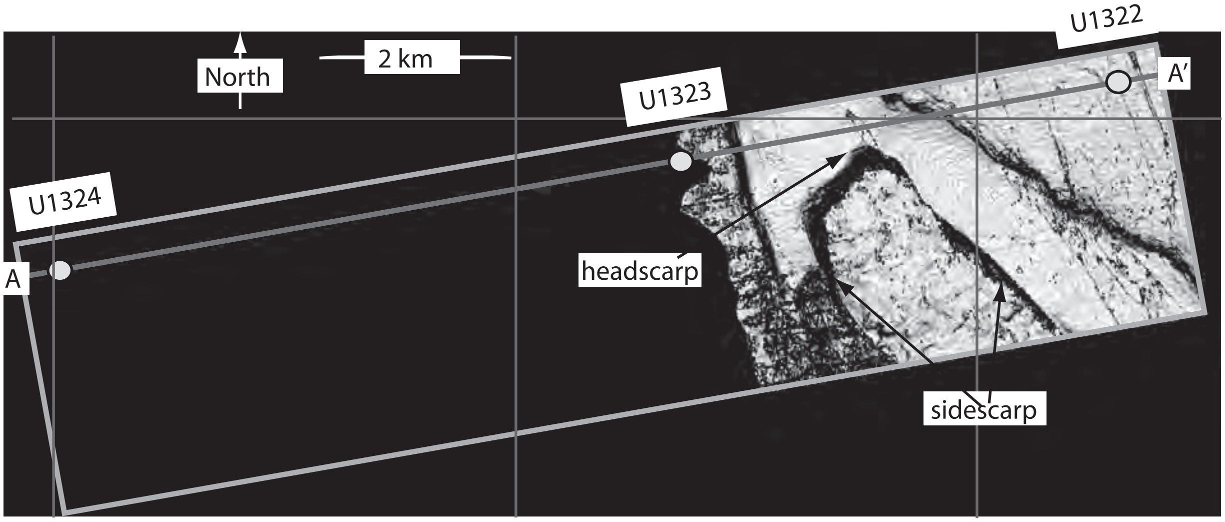

Figure 2.14
Dip map of base MTD-10 and MTD-9. MTD-9 remobilized and eroded into MTD-10. The headscarp and sidewalls are preserved and imaged in seismic data.

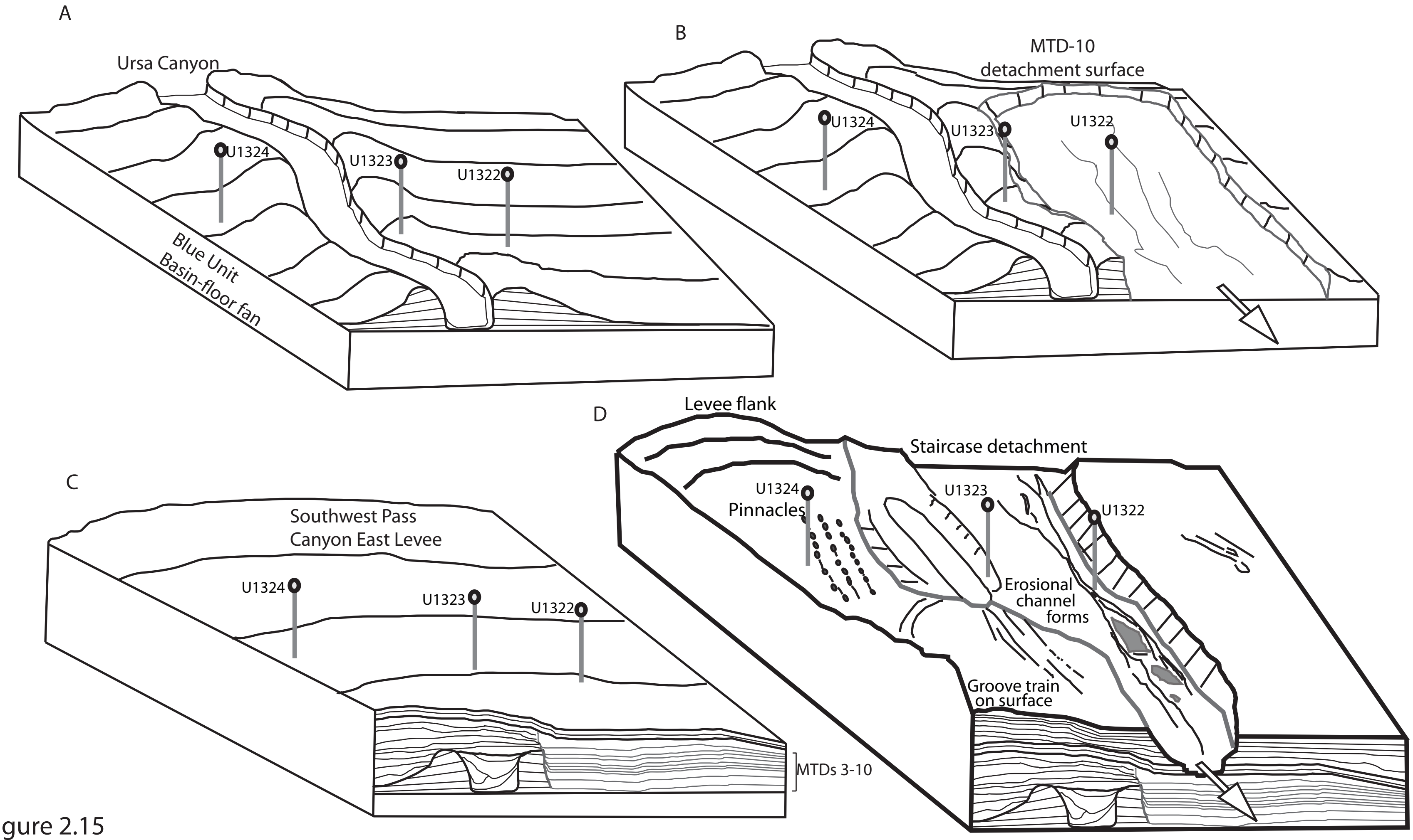

Figure 2.15
Illustration of Ursa Basin evolution. A.The Ursa Canyon deposited thick levees above the basin-floor fan. B. MTD-10 was the initial failure of the eastern levee of Ursa Canyon. Successive flows (MTDs 9-4) were trapped in the initial space created by MTD-10. C. Distal turbidites and levee sediments from Southwest Pass Canyon system capped this set of MTDs. D. MTD-2 was a regional-scale failure on the slope with multiple detachment levels.

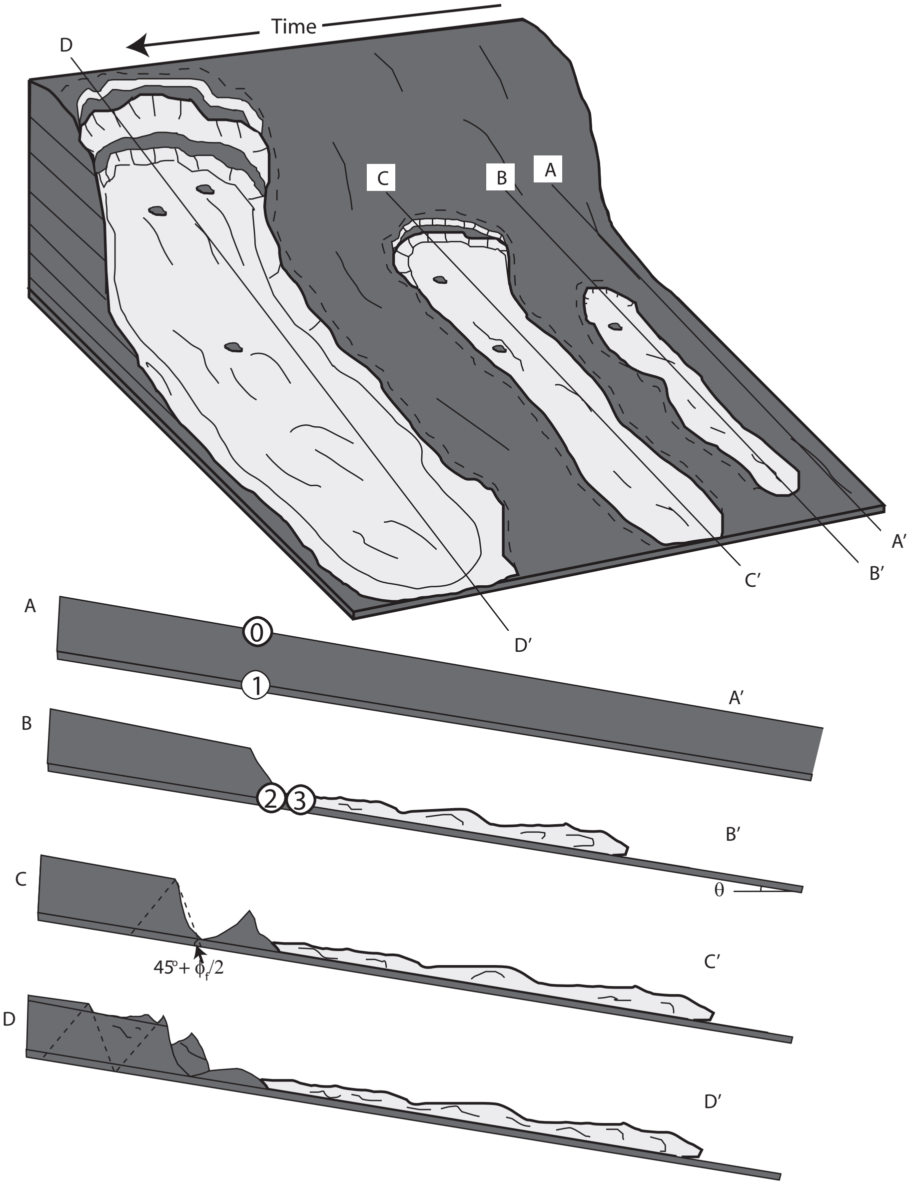

Figure 2.16
Conceptual model of time-evolution of retrogressive MTDs. Initial failure creates a scarp along the headwall and upper sidewalls that promotes extensional failure, strain weakening and ultimately a large complex forms. Cross-sections A-A′, B-B′, C-C′, and D-D′ illustrating the formation of Rankine active failure surfaces that fail down-slope over time and leave an open scarp behind. The theoretical failure planes lie at 45° +/- $\phi/2$. Points 0-3 refer to stress states at initial burial on seafloor, uniaxial consolidation, peak undrained shear strength, and critical state, respectively.

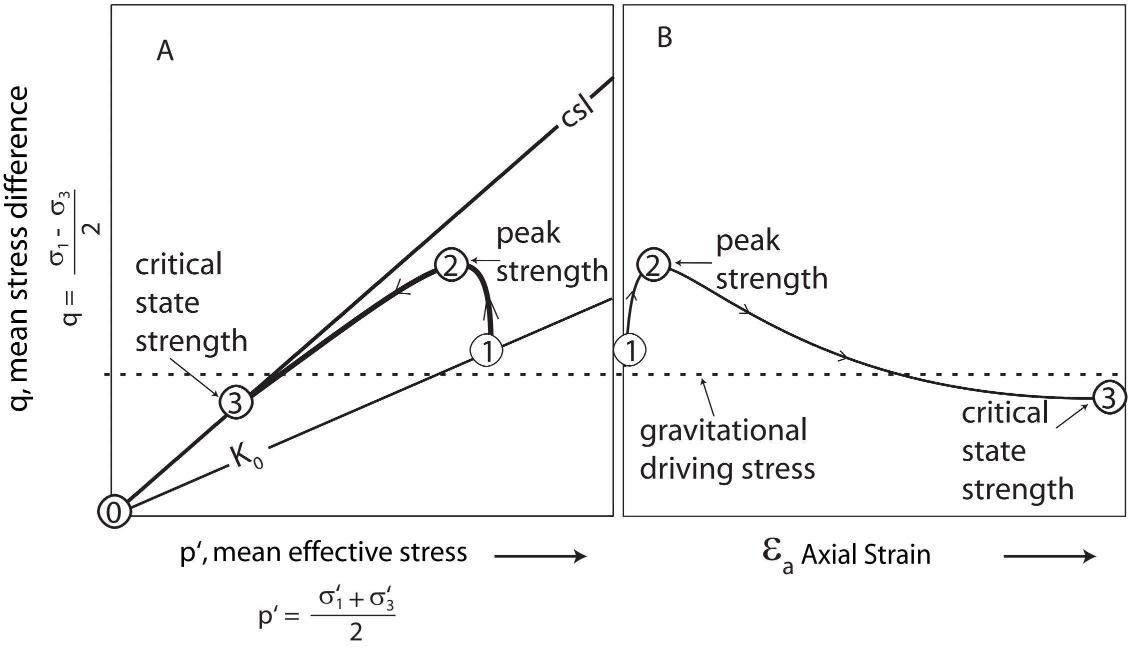

Figure 2.17
A. Conceptual p'-q plot showing stress paths from initial burial under uniaxial consolidation (pt. 0-1), followed by undrained shear to peak strength (pt. 1-2) and strain-weakening (sensitivity) to critical state strength (pt. 2-3).. Each point on a p'-q diagram represents the peak point on a Mohr circle of effective stress and allows successive states of stress to be presented [Lambe and Whitman, 1969]. The horizontal line represents the gravitational driving stress. B. Corresponding q vs. axial strain plot showing the rise to peak strength at low strain, then strain-weakening to critical state. The critical state line (CSL) defines the limiting failure envelope, which is a function of the friction angle. Ko defines the uniaxial strain burial condition.

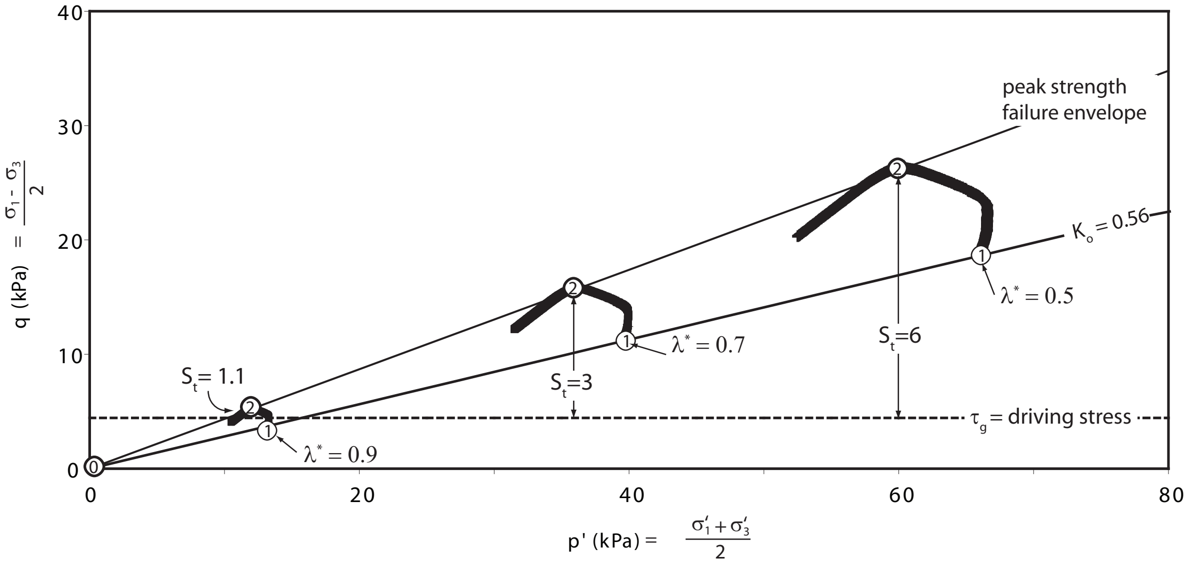

Figure 2.18
Undrained effective stress paths for three pore pressure conditions following uniaxial consolidation from seafloor to 30 mbsf (pt. 0 to 1). Experimental stress path is experiment TX 778 of Dugan and Germaine [2009]. $K_0 = 0.56$ and = 25.8°. Dugan and Germaine [2009] present the data normalized by the maximum vertical effective stress during K_0 consolidation (285.9 kPa). To plot them here, we multiply the normalized q values by 85 kPa, 51 kPa, and 17 kPa to represent the in-situ stress conditions of λ^* of 0.5, 0.7, and 0.9, respectively. Mean effective stress (p′) is calculated from the total vertical stress (integrated bulk density log), the pore pressure assumption, and K_0. Horizontal line represents the gravitational driving stress on a slip plane of 1.5°. Point '2' represents peak shear strength. Critical state was not reached in triaxial tests but vertical arrows represent Sensitivity (S_t) required to weaken the soil strength to the gravitational driving stress.

2.7 REFERENCES

Bardet, J.P., Synolakis, C.E., Davies, H.L., Imamura, F. and Okal, E.A., 2003. Landslide tsunamis: Recent findings and research directions. Pure and Applied Geophysics, 160(10-11): 1793-1809.

Bishop, A.W., 1973. The stability of tips and spoil heaps, Quarterly Journal of Engineering Geology. Scottish Academic Press; Geological Society of London : Edinburgh, United Kingdom, United Kingdom, pp. 335-376.

Bishop, A.W. and Bjerrum, L., 1960. The relevance of the triaxial test to the solution of stability problems, Proceedings of the ASCE Research Conference on Shear Strength of Cohesive Soils. American Society of Civil Engineers, Boulder, CO, pp. 437-501.

Booth, J.S., O'Leary, D.W., Popenoe, P. and Danforth, W.W., 1993. U.S. Atlantic Continental Slope Landslides: Their Distribution, General Attributes, and Implications. U.S. Geological Survey Bulletin, 2002: 14-22.

Brand, J.R., Lanier, D.L., Berger III, W.J., Kasch, V.R. and Young, A.G., 2003. Relationship Between Near Seafloor Seismic Amplitude, Impedance, and Soil Shear Strength Properties and Use in Prediction of Shallow Seated Slope Failure, Offshore Technology Conference, pp. 1-8.

Brodsky, E.E., Gordeev, E. and Kanamori, H., 2003. Landslide basal friction as measured by seismic waves. Geophysical Research Letters, 30(24, doi: 10.1029/2003GL018).

Burland, J.B., 1990. On the Compressibility and Shear Strength of Natural Clays. Geotechnique, 40(3): 329-378.

Butenko, J. and Barbot, J.P., 1980. Geologic Hazards Related To Offshore Drilling And Construction In The Orinoco River Delta Of Venezuela. Journal Of Petroleum Technology, 32(5): 764-770.

Chandler, R.J., 2000. Clay sediments in depositional basins: The geotechnical cycle. Quarterly Journal of Engineering Geology and Hydrogeology, 33: 7-39.

Coleman, J.M. and Prior, D.B., 1988. Mass-Wasting On Continental Margins. Annual Review Of Earth And Planetary Sciences, 16: 101-119.

Coleman, J.M. and Roberts, H.H., 1988. Late Quaternary Depositional Framework of the Louisiana Continental Shelf and Upper Continental Slope, Transactions GCAGS, pp. 407-419.

Corthay II, J.E. and Aliyev, A.A., 2000. Delineation of a Mud Volcano Complex, Surficial Mudflows, Slump Blocks, and Shallow Gas Reservoirs, Offshore Azerbaijan, Offshore Technology Conference, Houston, TX, pp. 1-11.

Dan, G., Sultan, N. and Savoye, B., 2007. The 1979 Nice harbour catastrophe revisited: Trigger mechanism inferred from geotechnical measurements and numerical modelling. Marine Geology, 245(1-4): 40-64, doi: 10.1016/j.margeo.2007.06.011

De Blasio, F.V., Elverhoi, A., Issler, D., Harbitz, C.B., Bryn, P. and Lien, R., 2005. On the dynamics of subaqueous clay rich gravity mass flows - the giant Storegga slide, Norway. Marine And Petroleum Geology, 22(1-2): 179-186.

Dugan, B. and Flemings, P.B., 2000. Overpressure and Fluid Flow in the New Jersey Continental Slope: Implications for Slope Failure and Cold Seeps. Science, 289: 288-291.

Dugan, B., Flemings, P.B., Urgeles, R., Sawyer, D.E., Iturrino, G.J., Moore, J.C. and Schneider, J., 2007a. Physical properties of mass transport complexes in the Ursa Region, northern Gulf of Mexico (IODP Expedition 308) determined from log, core, and seismic data, OTC 18704, Offshore Technology Conference, Houston, TX, pp. 1-13.

Dugan, B., Flemings, P.B., Urgeles, R., Sawyer, D.E., Iturrino, G.J., Moore, J.C. and Schneider, J., 2007b. Physical Properties of Stacked Slumps in the Ursa Region, Northern Gulf of Mexico (IODP Expedition 308) Determined from Log, Core, and Seismic Data, Paper #18704, Proceedings of the Offshore Technology Conference, Houston, TX.

Dugan, B. and Germaine, J.T., 2008. Near-seafloor overpressure in the deepwater Mississippi Canyon, northern Gulf of Mexico. Geophys. Res. Lett., 35(L02304, 10.1029/2007GL032275).

Dugan, B. and Germaine, J.T., 2009. Data Report: Strength Characteristics of Sediments from IODP Expedition 308, Sites U1322 and U1324. In: P.B. Flemings, J.H. Behrmann, C.M. John and a.t.E. Scientists (Editors), Proc. IODP, 308. Integrated Ocean Drilling Program Management International, Inc., College Station, TX, doi:10.2204/iodp.proc.308.210.2009.

Elverhoi, A., Norem, H., Andersen, E.S., Dowdeswell, J.A., Fossen, I., Haflidason, H., Kenyon, N.H., Laberg, J.S., King, E.L., Sejrup, H.P., Solheim, A. and Vorren, T., 1997. On the origin and flow behavior of submarine slides on deep-sea fans along the Norwegian Barents Sea continental margin. Geo-Marine Letters, 17(2): 119-125.

Flemings, P.B., Behrmann, J.H., John, C.M. and Scientists, E. (Editors), 2006. Gulf of Mexico Hydrogeology. Proceedings of the Integrated Ocean Drilling Program, 308. Integrated Ocean Drilling Program Management International, Inc., College Station TX.

Flemings, P.B., Long, H., Dugan, B., Germaine, J., John, C., Behrmann, J.H., Sawyer, D. and Scientists, I.E., 2008. Pore pressure penetrometers document high overpressure near the seafloor where multiple submarine landslides have occurred on the continental slope, offshore Louisiana, Gulf of Mexico. Earth and Planetary Science Letters, 269(3-4): 309-324.

Fryer, G.J., Watts, P. and Pratson, L.F., 2004. Source of the great tsunami of 1 April 1946: a landslide in the upper Aleutian forearc. Marine Geology, 203(3-4): 201-218.

Garziglia, S., Migeon, S., Ducassou, E., Loncke, L. and Mascle, J., 2008. Mass-transport deposits on the Rosetta province (NW Nile deep-sea turbidite system, Egyptian margin): Characteristics, distribution, and potential causal processes. Marine Geology, 250(3-4): 180-198, doi: 10.1016/j.margeo.2008.01.016.

Gee, M.J.R., Gawthorpe, R.L. and Friedmann, S.J., 2006. Triggering and evolution of a giant submarine landslide, offshore Angola, revealed by 3D seismic stratigraphy and geomorphology. Journal Of Sedimentary Research, 76(1-2): 9-19, doi: 10.2110/jsr.2006.02

Gee, M.J.R., Masson, D.G., Watts, A.B. and Allen, P.A., 1999. The Saharan debris flow: an insight into the mechanics of long runout submarine debris flows. Sedimentology, 46(2): 317-335.

Graham, J., 1984. Methods of Stability Analysis. In: D. Brundsen and D.B. Prior (Editors), Slope Instability. Landscape Systems: A Series in Geomorphology. John Wiley & Sons Ltd., pp. 171-215.

Hampton, M.A., 1996. Submarine Landslides. Reviews of Geophysics, 34(1): 33-59.

Homza, T.X., 2004. A Structural Interpretation of the Fish Creek Slide (Lower Cretaceous), northern Alaska. AAPG Bulletin, 88(3): 265-278.

Ilstad, T., Marr, J.G., Elverhoi, A. and Harbitz, C.B., 2004. Laboratory studies of subaqueous debris flows by measurements of pore-fluid pressure and total stress. Marine Geology, 213(1-4): 403-414, doi: 10.1016/j.margeo.2004.10.016

Iverson, R.M., 1997. The Physics of Debris Flows. Reviews of Geophysics, 35(3): 245-296.

Iverson, R.M., 2005. Regulation of landslide motion by dilatancy and pore pressure feedback. Journal of Geophysical Research, 110(F02015, doi:10.1029/2004JF000268).

Iverson, R.M., Reid, M.E. and LaHusen, R.G., 1997. Debris-flow mobilization from landslides. Annual Review of Earth and Planetary Sciences, 25: 85-138.

Jansen, E., Befring, S., Bugge, T., Eidvin, T., Holtedahl, H. and Sejrup, H.P., 1987. Large Submarine Slides on the Norwegian Continental-Margin - Sediments, Transport and Timing. Marine Geology, 78(1-2): 77-107.

Jeanjean, P., Hill, A. and Thomson, J., 2003. The Case for Confidently Siting Facilities along the Sigsbee Escarpment in the Southern Green Canyon Area of the Gulf of Mexico: Summary and Conclusions from Integrated Studies, Offshore Technology Conference.

Jenner, K.A., Piper, D.J.W., Campbell, D.C. and Mosher, D.C., 2007. Lithofacies and origin of late Quaternary mass transport deposits in submarine canyons, central Scotian Slope, Canada. Sedimentology, 54(1): 19-38, doi: 10.1111/j.1365-3091.2006.00819.x

Kayen, R.E., Schwab, W.C., Lee, H.J., Torresan, M.E., Hein, J.R., Quinterno, P.J. and Levin, L.A., 1989. Morphology Of Sea-Floor Landslides On Horizon Guyot - Application Of Steady-State Geotechnical Analysis. Deep-Sea Research Part A-Oceanographic Research Papers, 36(12): 1817-1839.

Kennett, J.P. and Huddlestun, P., 1972. Late Pleistocene paleoclimatology, foraminiferal biostratigraphy and tephrochronology, western Gulf of Mexico. Quaternary Research, 2(1): 38-69.

L'Hereux, J.S., Leroueil, S. and Laflamme, J.F., in press. Evolution of the Factor of Safety Following Excavation in Clay. Canadian Geotechnical Journal.

Laberg, J.S. and Vorren, T.O., 2000. Flow behaviour of the submarine glacigenic debris flows on the Bear Island Trough Mouth Fan, western Barents Sea. Sedimentology, 47(6): 1105-1117.

Lambe, T.W. and Whitman, R.V., 1969. Soil Mechanics. Series in Soil Engineering. John Wiley & Sons, New York, 553 pp.

Leroueil, S., 2001. Natural Slopes and Cuts: Movement and Failure Mechanisms. Geotechnique, 51(No. 3): 197-243, doi: 10.1680/geot.51.3.197.39365.

Li, Q., Xiang, R. and Zheng, F., 2007. Data report: planktonic and benthic foraminifers from IODP Hole U1322B. In: P.B. Flemings, Behrmann, J.H., John, C.M., and the Expedition 308 Scientists (Editor), Proc. IODP, 308. Integrated Ocean Drilling Program Management International, Inc., College Station, TX, doi:10.2204/iodp.proc.308.202.2007, pp. 1-8.

Lucente, C.C. and Pini, G.A., 2003. Anatomy and emplacement mechanism of a large submarine slide within a Miocene foredeep in the northern Apennines, Italy: A field perspective. American Journal Of Science, 303(7): 565-602.

Lucente, C.C. and Pini, G.A., 2008. Basin-wide mass-wasting complexes as markers of the Oligo-Miocene foredeep-accretionary wedge evolution in the Northern Apennines, Italy. Basin Research, 20(1): 49-71, doi:10.1111/j.1365-2117.2007.00344.x.

Major, J.J., 1996. Experimental studies of deposition by debris flows: Process, characteristics of deposits, and effects of pore-fluid pressure. Ph.D. Thesis, University of Washington, United States -- Washington.

Major, J.J., 2000. Gravity-driven consolidation of granular slurries - Implications for debris-flow deposition and deposit characteristics. Journal Of Sedimentary Research, 70(1): 64-83.

Major, J.J. and Iverson, R.M., 1999. Debris-flow deposition: Effects of pore-fluid pressure and friction concentrated at flow margins. GSA Bulletin, 111(10): 1424-1434.

Martinez, J.F., Cartwright, J. and Hull, B., 2005. 3D seismic interpretation of slump complexes: examples from the continental margin of Israel. Basin Research, 17(1): 83-108, doi: 10.1111/j.1365-2117.2005.00255.x.

Martinsen, O.J. and Bakken, B., 1990. Extensional and compressional zones in slumps and slides in the Namurian of County Clare, Ireland. Journal of the Geological Society, 147(1): 153-164.

Masson, D.G., Canals, M., Alonso, B., Urgeles, R. and Huhnerbach, V., 1998. The Canary Debris Flow: source area morphology and failure mechanisms. Sedimentology, 45(2): 411-432.

Masson, D.G., Harbitz, C.B., Wynn, R.B., Pedersen, G. and Lovholt, F., 2006. Submarine landslides: processes, triggers and hazard prediction. Philosophical Transactions of the Royal Society -Mathematical Physical and Engineering Sciences, 364(1845): 2009-2039.

Masson, D.G., vanNiel, B. and Weaver, P.P.E., 1997. Flow processes and sediment deformation in the Canary debris flow on the NW African continental rise. Sedimentary Geology, 110(3-4): 163-179.

McAdoo, B.G., Pratson, L.F. and Orange, D.L., 2000. Submarine landslide geomorphology, US continental slope. Marine Geology, 169: 103-136.

McArdell, B.W., Bartelt, P. and Kowalski, J., 2007. Field observations of basal forces and fluid pore pressure in a debris flow. Geophysical Research Letters, 34(L07406, doi:10.1029/2006GL029183): 1-4.

McFarlan, E. and LeRoy, D.O., 1988. Subsurface geology of the Late Tertiary and Quaternary deposits, coastal Louisiana, and the adjacent continental shelf, Gulf Coast Association of the Geological Societies Transactions, pp. 421-433.

McMurtry, G.M., Watts, P., Fryer, G.J., Smith, J.R. and Imamura, F., 2004. Giant landslides, mega-tsunamis, and paleo-sea level in the Hawaiian Islands. Marine Geology, 203(3-4): 219-233.

Mitchell, J.K., 1993. Fundamentals of Soil Behavior. John Wiley & Sons, Inc., New York, NY, 437 pp.

Mohrig, D., Whipple, K.X., Hondzo, M., Ellis, C. and Parker, G., 1998. Hydroplaning of subaqueous debris flows. Geological Society Of America Bulletin, 110(3): 387-394.

Morgenstern, N.R., 1967. Submarine Slumping and the Initiation of Turbidity Currents. Geotechnique: 189-220.

Moscardelli, L. and Wood, L., 2008. New classification system for mass transport complexes in offshore Trinidad. Basin Research, 20(1): 73-98.

Moscardelli, L., Wood, L. and Mann, P., 2006. Mass-transport complexes and associated processes in the offshore area of Trinidad and Venezuela. AAPG Bulletin, 90(7): 1059-1088, doi: 10.1306/02210605052.

Newton, S., Mosher, D., Shipp, C. and Wach, G., 2004. Importance of mass transport complexes in the Quaternary development of the Nile Fan, Egypt, Offshore Technology Conference, Houston, TX.

Niedoroda, A.W., Reed, C.W., Hatchett, L., Young, A., Lanier, D., Kasch, V., Jeanjean, P., Orange, D. and Bryant, W., 2003. Analysis of Past and Future Debris Flows and Turbidity Currents Generated by Slope Failures Along the Sigsbee Escarpment in the Deep Gulf of Mexico, Offshore Technology Conference, Houston, TX, pp. 1-7.

Ostermeier, R.M., Pelletier, J.H., Winker, C.D., Nicholson, J.W. and Cowan, C.K., 2002. Dealing with Shallow-Water Flow in the Deepwater Gulf of Mexico. The Leading Edge(July): 660-668.

Ostermeier, R.M., Pelletier, J.H., Winker, C.D., Nicholson, J.W., Rambow, F.H. and Cowan, C.K., 2000. Dealing with Shallow-Water Flow in the Deepwater Gulf of Mexico, Offshore Technology Conference, Houston, TX, pp. 75-86.

Pelletier, J.H., Ostermeier, R.M., Winker, C.D., Nicholson, J.W. and Rambow, F.H., 1999. Shallow Water Flow Sands in the Deepwater Gulf of Mexico: Some Recent Shell Experience, 1999 International Forum on Shallow Water Flows Conference Proceedings, League City, TX.

Piper, D.J.W., Pirmez, C., Manley, P.L., Long, D., Flood, R.D., Normark, W.R. and Showers, W., 1997. Mass-Transport Deposits of the Amazon Fan. In: R.D. Flood, D. J. W. Piper, A. Klaus, and L. C. Peterson (Editor), Proceedings of the Ocean Drilling Program, Scientific Results, pp. 109-146.

Pirmez, C., Marr, J., Shipp, C., and Kopp, F., 2004. Observations and Numerical Modeling of Debris Flows in the Na Kika Basin, Gulf of Mexico, Offshore Technology Conference, Houston, TX, pp. 1-13.

Posamentier, H. and Kolla, V., 2003. Seismic Geomorphology and Stratigraphy of Depositional Elements in Deep-Water Settings. Journal of Sedimentary Research, 73(3): 367-388.

Posamentier, H.W., 2003. Depositional elements associated with a basin floor channel-levee system: case study from the Gulf of Mexico. Marine and Petroleum Geology, 20: 677-690.

Poulos, S.J., 1981. The Steady-State Of Deformation. Journal Of The Geotechnical Engineering Division-Asce, 107(5): 553-562.

Poulos, S.J., Castro, G. and France, J.W., 1985. Liquefaction Evaluation Procedure. Journal Of Geotechnical Engineering-Asce, 111(6): 772-792.

Prior, D.B., Bornhold, B.D. and Johns, M.W., 1984. Depositional Characteristics of a Submarine Debris Flow. Journal of Geology, 92: 707-727.

Prior, D.B. and Suhayda, J.N., 1979. Application of infinite slope analysis to subaqueous sediment instability, Mississippi delta. Engineering Geology, 14(1): 1-10.

Sawyer, D.E., Flemings, P.B. and Dugan, B., 2007b. Lateral variations in core, log, and seismic attributes of a mass transport complex in the Ursa Region, IODP Expedition 308, Northern Gulf of Mexico, Paper # 19098, Offshore Technology Conference, Houston, TX, pp. 1-12.

Sawyer, D.E., Flemings, P.B., Shipp, R.C. and Winker, C.D., 2007a. Seismic geomorphology, lithology, and evolution of the late-Pleistocene Mars-Ursa turbidite region, Mississippi Canyon area, northern Gulf of Mexico. AAPG Bulletin, 91(2): 215-234, doi: 10.1306/08290605190.

Sawyer, D.E., Jacoby, R., Flemings, P.B. and Germaine, J.T., 2008. Data Report: Particle Size Analysis of Sediments in the Ursa Basin, IODP Expedition 308 Sites U1324 and U1322, Northern Gulf of Mexico. In: P.B. Flemings, J.H. Behrmann, C.M. John and a.t.E. Scientists (Editors), Proc. IODP, 308. Integrated Ocean Drilling Program Management International, Inc., College Station, TX, doi:10.2204/iodp.proc.308.205.2008.

Schwab, W.C., 1988. Causes of two slope-failure types in continental-shelf sediment, northeastern Gulf of Alaska. In: H.J. Lee (Editor), Journal of Sedimentary Petrology. Society of Economic Paleontologists and Mineralogists : Tulsa, OK, United States, United States, pp. 1-1.

Schwab, W.C., Lee, H.J. and Molnia, B.F., 1988. Causes Of Varied Sediment Gravity Flow Types On The Alsek Prodelta, Northeast Gulf Of Alaska. Marine Geotechnology, 7(4): 317-342.

Shipp, R.C., Nott, J.A. and Newlin, J.A., 2004. Physical Characteristics and Impact of Mass Transport Complexes on Deepwater Jetted Conductors and Suction Anchor Piles, OTC 16751, Offshore Technology Conference. Offshore Technology Conference, Houston, TX, May 3-6, pp. 1-11.

Skempton, A.W., 1970. The consolidation of clays by gravitational compaction, Quarterly Journal of the Geological Society of London. Geological Society of London : London, United Kingdom, United Kingdom, pp. 373-411.

Stow, D.A.A., 1986. Deep clastic seas. In: H.G. Reading (Editor), Sedimentary Environments and Facies. Blackwell Scientific Publications, Oxford, pp. 399-444.

Styzen, M.J., 1996. A Chart in Two Sheets of the Late Cenozoic Chronostratigraphy of the Gulf of Mexico, Gulf Coast Section, Society of Economic Paleontologists and Mineralogists, Houston, Texas.

Tappin, D.R., Watts, P., McMurtry, G.M., Lafoy, Y. and Matsumoto, T., 2001. The Sissano, Papua New Guinea tsunami of July 1998 - offshore evidence on the source mechanism. Marine Geology, 175(1-4): 1-23.

Terzaghi, K., 1956. Varieties of Submarine Slope Failures, 8th Texas Conference on Soil Mechanics and Foundation Engineering. University of Texas at Austin Bureau of Engineering Research, pp. 1-42.

Tripsanas, E.K., Piper, D.J.W., Jenner, K.A. and Bryant, W.R., 2008. Submarine mass-transport facies: new perspectives on flow processes from cores on the eastern North American margin. Sedimentology, 55(1): 97-136, doi:10.1111/j.1365-3091.2007.00894.x.

Urgeles, R., Canals, M., Baraza, J., Alonso, B. and Masson, D., 1997. The most recent megalandslides of the Canary Islands: El Golfo debris avalanche and Canary debris flow, west El Hierro island. Journal Of Geophysical Research-Solid Earth, 102(B9): 20305-20323.

Urgeles, R., Locat, J. and Dugan, B., 2007. Recursive Failures of the Gulf of Mexico Continental Slope: Timing and Causes. In: V. Lykousis, D. Sakellariou and J. Locat (Editors), Submarine Mass Movements and Their Consequences: 3rd International Symposium. Springer, pp. 11.

Weimer, P., 1990. Sequence Stratigraphy, Facies Geometries, and Depositional History of the Mississippi Fan, Gulf of Mexico. The American Association of Petroleum Geologists Bulletin, 74(4): 425-453.

Weimer, P. and Shipp, C., 2004. Mass transport Complex: Musing on past uses and suggestions for future directions, OTC paper 16752, Offshore Technology Conference, Houston, TX, pp. 1-10.

Whitman, R.V., 1985. On liquefaction, Proceedings of the International Conference on Soil Mechanics and Foundation Engineering. A.A. Balkema : Rotterdam-Boston, International, pp. 1923-1926.

Winker, C.D. and Booth, J.R., 2000. Sedimentary Dynamics of the Salt-Dominated Continental Slope, Gulf of Mexico: Integration of Observations from the Seafloor, Near-Surface, and Deep Subsurface, GCSSEPM Foundation 20th Annual Research Conference, pp. 1059-1086.

Winker, C.D. and Shipp, R.C., 2002. Sequence Stratigraphic Framework for Prediction of Shallow Water Flow in the Greater Mars-Ursa Area, Mississippi Canyon Area, Gulf of Mexico Continental Slope, 22nd Annual GCSSEPM Foundation Bob F. Perkins Research Conference, abs., pp. 1.

Yamamoto, Y., Sawyer, D.E., Behrmann, J.H., Flemings, P.B., John, C.M. and Party, I.E.S.S., 2005. Fabric contribution to sediment physical properties in Gulf of Mexico: Preliminary Results of IODP Expedition 308, Abstract OS21A-1514, Eos Trans. AGU, Fall Meet. Suppl.

Chapter 3

Mudflow Transport Behavior and Deposit Morphology: Role of Shear Stress to Yield Strength Ratio in Subaqueous Experiments

ABSTRACT

The ratio of the shear stress to yield strength, defined here as the flow factor, controls transport behavior and deposit morphology in experimental dam-break subaqueous mudflows. A high flow factor (yield strength much lower than shear stress) produced an immediate collapse of the source area volume with an accelerating flow and a prominent turbidity current. It discharged 78 % of the original volume in 2.5 minutes and emplaced a thin and broad deposit as a single mass. In contrast, a medium flow factor generated a slow retrogressive failure that left behind a blocky, highly fractured source area and constructed a short, thick and hummocky deposit. Internal levees formed in these flows and channeled material downdip while inhibiting lateral growth. The deposit was constructed piece-wise over a period of 11.8 minutes as opposed to single mass emplacement. When flow factor is low (yield strength nearly equal to shear stress), only a narrow zone of failure occurs and a short and thick deposit is constructed. My experiments suggest that a detailed analysis of deposit surface morphology from seismic or field data can yield important clues to the depositional history of the flow. This has important implications for hazard assessments that require accurate predictions of slide dynamics and for interpreting depositional history of past mudflows.

3.1. INTRODUCTION

Submarine mudflows and debris flows are fine-grained, gravity-driven, flows having approximately equal parts water and solid by volume (Iverson, 1997; Mohrig et al., 1999; O'Brien and Julien, 1988). They are important sediment transport processes that redistribute large volumes of sediment and affect routing of subsequent mass flows including turbidity currents. (Aksu, 1984; Elverhoi et al., 2002; Embley, 1976; Gee et al., 1999; Hampton, 1972; Masson et al., 1997; Prior et al., 1984; Urgeles et al., 1997). Mudflows may create tsunamis, coastal erosion, and destruction of seafloor pipelines, cables, and platforms (Dan et al., 2007; Dugan and Flemings, 2000; Masson et al., 2006; Synolakis et al., 2002; Zakeri et al., 2008).

Mudflow deposits are imaged in 3-D seismic reflection data and record a fascinating variety of surface expressions and deposit architectures (De Blasio et al., 2005; Gee et al., 2006; Gee et al., 1999; Henrich et al., 2008; Martinez et al., 2006; McAdoo et al., 2000; Minisini et al., 2007; Moscardelli et al., 2006; Mosher et al., 2004; Mulder and Alexander, 2001; Mulder et al., 1997; Piper et al., 1985; Piper et al., 1997; Pirmez, 2004; Posamentier, 2003; Twichell et al., 2009). It remains a challenge to identify the most diagnostic morphological elements and how they relate to flow behavior and failure conditions. For example, some flow deposits appear to have moved a short distance from their source area with much of the initial stratigraphy preserved. In other cases, flows appear to have traveled hundreds of kilometers in which the initial soil structure is completely remolded.

Much of the difficulty with interpreting mudflow deposit morphology is that mudflows occur within sediments of widely varying composition, porosity, and shear strength, in all tectonic settings, and are triggered by numerous mechanisms including sedimentation-induced overpressuring (Dugan and Flemings, 2000; Flemings et al., 2008;

Stigall and Dugan, 2010), gas-charging (Bunz et al., 2005), storm wave loading (Rogers and Goodbred; Seed, 1978), salt diapirism (Orange et al., 2003), earthquakes (Hornbach et al.; Morgenstern, 1967; Stigall and Dugan, 2010; Strozyk et al.), and volcanic activity (Moore et al., 1989)). However, all mudflows initiate in the same manner: when the downslope component of shear stress exceeds the shear strength (Hampton, 1996; Iverson et al., 1997). The ratio between the shear stress that drives flow (τ_D) and the shear strength that resists flow (τ_R) is defined here as the flow factor (F_f)

$$F_f = \frac{\tau_D}{\tau_R}. \qquad (1)$$

If F_f is high (>> 1), soil strength is much weaker than the driving stress. If F_f is low (~1), soil strength is nearly equal to the shear stress. If F_f is less than 1, soil strength exceeds shear stress, and no flow will occur. The F_f is the inverse of the engineering factor-of-safety, which is the ratio of the resisting strength to the driving stress and a standard method for evaluating slope stability (Lambe and Whitman, 1969).

Direct observations of natural subaqueous flows are not possible, thus laboratory flume studies and rheological models are the main tools to explore dynamic mudflow behavior. Most flume experiments inject a sediment-water slurry down a slope to study flow dynamics over a wide range of conditions and sediment properties (Mohrig et al., 1998; Marr et al., 2002; Ilstad et al., 2004; De Blasio et al., 2005; Issler et al., 2005). However, this method does not capture the pre-failure or failure processes and conditions that preceded the flow. Experiments on subaqueous sediment failures starting from an intact bed have been described in several studies (Ancey and Cochard, 2009; Cochard and Ancey, 2009; Einsele, 1974; Rettger, 1935; Schwartz, 1982; Zreik et al., 1995). These experiments induce failure by tilting a tabular sediment bed until failure occurs or with a 'dam-break' release method in which a vertical wall is suddenly released in front of an inclined tabular bed (Ancey and Cochard, 2009; Cochard and Ancey, 2009).

Geotechnical models rely on force balances to predict that flow is initiated from intact soil when shear stress exceeds the shear strength (Hampton et al., 1978; Kayen et al., 1989; Lee et al., 1991; Poulos, 1981; Schwab et al., 1988). Once flow is established, it is commonly assumed that the soil behaves as a non-Newtonian fluid defined by a yield strength and viscosity (Huang and García, 1999; Imran et al., 2001; Johnson, 1970). These viscoplastic models simulate flow runout distance, flow velocity, and deposit thickness based on the yield strength and viscosity. These models however do not predict the three-dimensional character or the fine-scale surficial features of the final deposit.

Here I trigger mudflows from static beds for which I know the shear stress and shear strength *a priori*. Thus I have a novel approach to explore how the difference between shear stress and shear strength, quantified as F_f, controls the characteristics of the dynamic mudflow and the morphology of the deposit. An advantage of the dam-break method is that I can capture the initiation of flow as it evolves from a static bed. Other dam-break experiments using Carbopol gel have been reported by Cochard and Ancey (2008) and Ancey and Cochard (2009). Here I conduct subaqueous experiments with mixtures of natural materials (kaolin clay, silt, and water). I describe my experimental methods and present dynamic behavior and deposit morphology of low, medium, and high F_f sediment-water mixtures. A key result of my experiments is that low, medium, and high F_f experiments produce unique transport behaviors and distinct deposit morphologies. Furthermore, similar behaviors can be produced from very different lithologies if the F_f is similar. I discuss these diagnostic features and processes and suggest this insight can guide studies of past mudflows and hazard analyses of possible future mudflows. A significant component of this study was developing a methodology to understand how different sediment mixtures behave as they progress through failure and post-failure states.

3.2. SEDIMENT RHEOLOGY

3.2.1 Overview

The experimental sediment slurries are mixtures of natural kaolin clay mined in Florida, U.S.A (E.P. Kaolin clay) (Pirkle, 1960), silica silt, and room temperature tap water. I characterize slurry rheology by clay fraction (ε_c), water content (w), yield strength (τ_y), and Herschel-Bulkley viscosity parameters K and n. I then calculate the gravitational driving stress (τ_y) for each mixture for a subaqueous 10-cm thick bed sloping at 10°. Finally, I calculate F_f by the ratio of the gravitational driving stress to yield strength. All experimental values are reported in Table 1. All symbols are defined in Table 2.

3.2.2 Grain Size and Water Content

I measured the grain size distributions of the kaolin clay and the silt with a standard hydrometer analysis (ASTM, 2007) (Figure 3.1). By mass, the kaolin clay is composed of 77 % clay-sized particles (< 2 μm) and 23 % silt-sized particles. The silt is composed of 90 % silt-sized and 10 % clay-sized particles. The reported clay fraction (ε_c) for each experimental slurry is corrected for the grain size distribution of each component (Table 3.1). For example, a mixture of 75 % kaolin clay and 25 % silt contains 60 % clay-sized particles and 40 % silt-sized particles. Sediment with this grain-size distribution is classified as a silty clay (Shepard, 1954). Thus ε_c is the percent by mass of clay-sized particles to the mass of the solids.

$$\varepsilon_c = \frac{M_{clay}}{M_{solids}} \times 100 \qquad (2)$$

The water content of the slurries, w, is the mass ratio of water to solid grains:

$$w = \frac{M_{water}}{M_{solids}} \times 100 . \qquad (3)$$

It is related to void ratio (e) and porosity (ϕ) (assuming saturation = 100%):

$$wG_s = e = \frac{\phi}{(1-\phi)}, \tag{4}$$

where G_s is the specific gravity of the solid grains. I chose this water content range because it allowed the mixture to be easily poured into the bed mold (as opposed to forming the bed through particle settling), and to have a porosity (ϕ) characteristic of natural seafloor sediment that generate mudflows (Einsele, 1990; Keller et al., 1979; Lee and Baraza, 1999; Sawyer et al., 2009).

3.2.3 Yield Strength

I used a rotational viscometer (Fann model 35) to measure yield strength (τ_y) of 29 slurries, each with different clay fraction and water content. Viscometers are the most common tool to measure yield strength of fine-grained sediment-water mixtures (Coussot et al., 1998; Ilstad et al., 2004; Major and Pierson, 1992; Zakeri et al., 2008).

All mixtures have a shear-thinning rheology in which the viscosity (slope of stress-strain curve) decreases as shear rate increases (Figure 3.2). Shear-thinning behavior is common for clayey slurries and is also referred to as pseudoplastic and Casson behavior (Coussot et al., 1998; Coussot and Proust, 1996; Coussot et al., 1996; Ilstad et al., 2004; Locat, 1997; Locat and Demers, 1988; Phillips and Davies, 1991). At each strain rate setting, I recorded shear stress readings at 20-second intervals for a total 5 minutes. In all tests, the shear stress values increased over time and in most cases reached steady state after 5 minutes. In Figure 2, I plot the steady-state yield strength at each strain rate. To define τ_y at zero strain rate, I fit each viscometer test with a Herschel-Bulkley model:

$$\tau = \tau_y + K\gamma^n, \tag{5}$$

where τ is shear stress, K is apparent viscosity, γ is shear strain rate, and n describes the rate of change of viscosity ($n = 1$ for Bingham; $n < 1$ for shear-thinning).

Yield strength is inversely proportional to water content and proportional to clay fraction (Figure 3.3) as noted by previous authors (Marr et al., 2001). As water content increases, the interaction between adjacent particles decreases and thus yield strength decreases (Lambe and Whitman, 1969). Clay minerals carry electrostatic forces that can result in a net attractive forces to increase yield strength (Craig, 1992). Therefore knowledge of composition or water content alone is insufficient for predicting yield strength and mudflow behavior. As I will show, a given composition (clay-rich or silt-rich) can exist as either low or high F_f, depending on the water content. Similarly, a given water content can exist as low or high F_f depending on its grain size distribution.

3.2.4 Gravitational Shear Stress

The gravitational shear stress flow (τ_g) is due to the weight of the submerged bed inclined at 10°. I calculate τ_g assuming a 2-D infinite slope (Graham, 1984):

$$\tau_g = \gamma_b z \sin\theta \cos\theta , \qquad (6)$$

where γ_b is the submerged unit weight (Table 3.1), z is bed thickness (10 cm), and θ is the bed slope (10°). The variation in w and grain densities between kaolin clay and quartz control the variation in τ_g (Table 3.1).

3.2.4 Flow Factor

For each viscometer test I calculated F_f from eq. 1; I used τ_g and τ_y as the driving stress (τ_D) and resisting strength (τ_R) terms, respectively. I then plot w versus ε_c and contour with respect to F_f (Figure 3.4). The advantage of the F_f contour plot is that I normalize for the competing effects of clay fraction and water content.

I use figure 3.4 to predict that mixtures with equal F_f will produce similar styles of mudflow despite having markedly different water contents and compositions. I selected 6 mixtures for mudflow experiments that covered the wide range of F_f. I arbitrarily defined 3 F_f zones within Figure 3.4: high (F_f = ~6), medium (F_f = ~3), and low (F_f = ~1). Experiment 1 lies within the high F_f zone, experiments 2 and 3 within the medium F_f zone, and experiments 4-6 lie within the low F_f zone.

3.3. MUDFLOW EXPERIMENT PROCEDURE

Each experiment consists of 3 stages (Figure 3.5). In Stage 1, I first mix silt, clay, and water in a concrete mixer for 45 minutes, then hand-scoop the slurry from buckets into a horizontal aluminum-framed plexi-glass inner tank to form a tabular bed 75 cm long, 24 cm wide, and 10 cm thick (0.18 m^3). The average total mass of clay, silt, and water for each experiment was 45 kg. I then carefully smooth the surface of the bed and place colored sand grains on the surface to help visualize surface movements during the mudflow experiment. I then fill the outer tank with fresh water at room temperature to a depth of 2.5 meters. I first fill rapidly until the water surface reaches the bottom of the bed (20 minutes), then very slowly until the bed is submerged (~30 minutes). I then fill to the total depth of 2.5 meters and allow the bed to sit overnight. In Stage 2, I lower the front end of the inner tank to the 10° slope, raise the front gate to initiate flow, and collect time-lapse digital photos and video of the mudflow event until I no longer observe movement. In Stage 3, I map the source area and lobe deposit with a laser mapping system at 1mm x 1mm spatial resolution. I use the time-lapse photos and video to quantify flow velocity and volumetric discharge rate. I use the deposit maps to quantify deposit geometry such as length, width, and thickness.

3.4 RESULTS OF EXPERIMENTAL MUDFLOWS

3.4.1 Summary

I observed a continuum of dynamic behaviors and deposit morphologies between high, medium, and low F_f experiments (Figure 3.6). High flow factor (F_f = ~6) produced an immediate collapse of the source area with an accelerating flow and an associated turbidity current, and deposited a long and thin deposit *en masse*. Medium flow factor (F_f = ~3) created a retrogressive mudflow in which many (~100) small blocks detached from the source area and accumulated piece-by-piece into one deposit. Finally, when F_f is low (F_f = ~1), a blocky failure occurs with very limited runout distance and volume. In the following sections, I present details of high, medium, and low F_f experiments; I focus on the dynamic response and the final morphology of the accumulated deposit and source area.

3.4.2 High F_f (Experiment 1)

Experiment 1 had a high F_f of 6.23. The pre-failure deposit was therefore very weak relative to the shear stress. As a result, a rapidly moving mudflow (v_p = 16.3 cm/s) developed with a prominent turbidity current that outpaced the lobe (Figure 3.6A). The event duration was 2.5 minutes during which most of the original volume (70%) discharged from the source area within the first 10 seconds (Figure 3.7 and Table 3.3). The final volumetric distribution was 73% in the depositional lobe, 5% in the turbidity current, and 22% remaining in the source area (Figure 3.7).

The prominent turbidity current obscured my visual observations of the mudflow body. As a result I did not see if the main body hydroplaned as it traveled across the tank floor. However, I used the densimetric Froude number (F_{R_d}) presented in Mohrig et al, 1998 to further explore the possibility that this flow could have hydroplaned:

$$F_{R_d} = \frac{v}{\left[\left(\frac{\rho_b}{\rho_w} - 1\right) g h_a \cos\theta\right]^{0.5}} \tag{7}$$

where v is flow velocity, ρ_b is the bulk density of the material, ρ_w is density of water, g is gravitational acceleration, h_a is flow thickness, and θ is bed slope. Mohrig et al, 1998 suggest that flows with F_{R_d} greater than 0.35 are capable of hydroplaning. My calculated value for Experiment 1 is 0.65, which suggests that this flow hydroplaned.

The source area is tabular and thin (~2 cm) (Figure 3.7A). The surface contains subtle closely-spaced fractures that penetrate < 0.5 cm (Figure 3.6D and Figure 3.7A). These fractures developed only at the very end of the mudflow event and therefore are not associated with retrogressive failure.

The characteristic deposit features of experiment 1 are the long runout distance (140.2 cm) and very thin profile (Figure 3.8A, E, and Table 3.3). The deposit contains subtle compression ridges in the central area, which coincides with the break-in-slope (Figure 3.9E). Otherwise this deposit is remarkably smooth. The maximum deposit thickness also occurs at the break-in-slope (Figure 3.9A) and thins gradually to the end of the deposit. The L:W ratio of.1.3 indicates that the longest dimension is in the dip direction.

3.4.3 Medium F_f (Experiments 2 and 3)

Experiments 2 and 3 had medium F_f values of 3.53 and 3.05, respectively. I discuss experiment 3 in more detail but I point out key differences between both experiments.

The dynamic response of experiment 3 was retrogressive block failure of the source area accompanied by piece-by-piece accumulation in the depositional lobe over a period of 11.8 minutes (Figure 3.6 C,D and Figure 3.7). During the initial 30 seconds, the mudflow moved rapidly (v_p = 5.5 cm/s) but thereafter discharge rate was constant (Figure 3.7 and Table 3.3). Internal levees formed during lobe construction and channeled material downslope between levee margins (Figure 3.6D). This limited lateral spreading of the deposit but enhanced growth in the dip direction. The final volumetric distribution was 40 % contained in the lobe deposit, 59 % in the source area, and 1 % in a turbidity current (Figure 3.7).

I discuss the evolution of the retrogressive failure of experiment 3 in more detail (Figure 3.10). Within 5 seconds of flow initiation, a prominent headscarp formed ~25 cm upslope of the gate (Figure 3.10B). A zone of horst-graben structures and detached blocks developed between this headscarp and the gate. As each block detached from the main headscarp, it was progressively broken up into smaller blocks as it migrated through the system and accumulated at the back of the lobe deposit. With time, headwall retreat was balanced by downslope movement and growth of the lobe deposit. Levees formed within the interior of the deposit 20 seconds after gate release (Figure 3.10C). After 2.6 minutes, the entire surface of the source area was a zone of retrogressive failure (Figure 3.10D). The lobe continued to migrate downdip as it was pushed along by the evacuated blocks accumulating at the rear. As the deposit front was being pushed from behind, radial tension structures developed along the front (Figure 3.10D).

The final topography of the source area of experiment 3 records the retrogressive failure process (Figure 3.8A,C). Fracture spacing is 2-3 cm and fracture depth is 1- 2 cm.

The deposit of experiment 3 has a hummocky surface texture (Figure 3.6D, and Figure 3.9A,C). Radial tension fractures occur along the perimeter of the lobe. The blocky surface topography is the result of the piece-by-piece construction process (Figure 3.9A-C). The L:W ratio for experiment 4 is 1.9, which indicates the longest dimension is the dip direction. This reflects the role of the internal levees that acted to funnel material down-dip and limited lateral growth. Total runout distance was 63.7 cm and maximum lobe thickness was 1.9 cm (Figure 3.9A).

Experiment 3 ($F_f = 3.53$) was a medium F_f experiment but it resulted in a run-out length that was nearly equal to the high F_f experiment 1 (Figure 3.9 and Table 3.3). However, I argue this flow behaved more like the medium F_f experiment 2 because it evacuated retrogressively, formed internal levees, and generated a dilute turbidity current. I attribute the long runout distance to lateral levees that formed in the interior of the flow that enhanced growth in the down-dip direction, as observed in Experiment 2. This allowed experiment 3 to attain an equivalent runout distance to experiment 1, despite having a lower F_f.

3.4.4 Low F_f (Experiments 4-6)

Experiments 4 - 6 had low F_f values (< 2) (Table 1). However, only experiments 4 and 5 resulted in mudflow. The yield strength of the mixture used in Experiment 6 was greater than the shear stress ($F_f = 0.95$) and thus produced no flow. I discuss experiment 4 in detail as the characteristic experiment for this group.

The dynamic response of Experiment 4 was a very slow-moving blocky failure (Figure 3.6A,B; Table 3.3;). The event lasted 2.5 minutes; 3 blocks evacuated the source area and amalgamated into a single deposit. 2 suture lines define the locations of where the blocks joined (Figure 3.6B). As each block impacted the lobe, the entire lobe deposit was pushed along the bottom. As the lobe advanced, it spread outwardly, which is recorded by radial tension fractures that developed along the perimeter of the lobe (Figure 3.6B). Only 10 % of the original source volume evacuated the source area (Figure 3.7). The peak and average flow velocity (v_p and v_a) was 0.8 cm/s and 0.1 cm/s, respectively (Table 3.3).

The morphology of the source area records the limited retrogressive failure process (Figure 3.8A,B). The headwall marks the up-dip limit of retrogression. Down-dip of the headwall is a zone (35% by area) of detached fault blocks and grabens. Up-dip of the headwall is a smooth and featureless zone (65% by area) that is nearly unaltered from its pre-failure condition except for very subtle hairline cracks only visible with the naked eye. In the zone of detached blocks, the fracture spacing is 3-5 cm and penetration depth is limited to ~1 cm (Figure 3.7A).

The deposit morphology records its piece-by-piece depositional history (Figure 3.6 A,B, Figure 3.9 A,B). The depositional lobe contains 3 blocks. Each block is separated by a suture line, which is imaged as a furrow oriented perpendicular to flow direction (Figure 3.6 A,B, Figure 3.9 A,B). Radial tension fractures are distributed along the perimeter of the toe. The total runout was 10.1 cm, and maximum thickness was 4.5 cm. The lobe is longer in the strike direction indicated by an aspect ratio of 0.4 (Table 3.3)

3.5. DISCUSSION

I summarize the continuum of flow behavior and deposit morphology as a function of flow factor. In all cases, mudflow begins when the initial flow factor is above

1 and ends when flow factor drops to 1. When the flow factor is high ($F_f > 6$) the driving stress is much greater than the material strength, which results in an immediate collapse of the source area into a rapidly accelerating mudflow (possibly hydroplaning) with a prominent turbidity current (Figure 3.6 A,B). The flow evacuates rapidly from the source area, which drives the flow factor to also drop rapidly. The result is a rapid mudflow event but with a short duration (Figure 3.7). The deposit is thin, and broad, with a smooth surface texture with very little surface relief. The source area contains only subtle surface fractures (Figure 3.6A). When initial flow factor is intermediate ($F_f \sim 3$), a retrogressive failure process is established in which the master headwall retreats up-dip at a moderate pace (Figure 3.6 C,D. Figure 3.7). In these cases, the flow factor drops much more slowly than when flow factor is high. The result is a slower mudflow but with a long duration. The deposit develops internal levees during its growth stage, which funnel material downdip into a long and narrow deposit. Finally, if the initial flow factor is low, shear stress and resisting strength are nearly equal and the resulting failure is a slow-moving small-volume flow that is short-lived and does not generate a turbidity current (Figure 3.6 E,F). It leaves behind a fractured source area with a master headwall that does not retreat far up-dip. The length:width ratio is less than 1 indicating that the longest dimension in the strike direction.

In all experiments, the flow factors progressively decreased during the dynamic release phase and converged to a value of approximately 1, which marked the end of the mudflow event (Figure 3.11). I calculated the theoretical final bed thickness that each experiment would converge to, assuming a final flow factor of 1, and plotted them against the observed final bed thickness. The match is very good for medium and high flow factor experiments, indicating that these flows stopped moving when the gravitational shear stress dropped (via decrease in bed thickness) to a value equal to the yield strength. For the low flow factor experiments, this relationship is more difficult to discern because only the front portions of these beds actually failed (Figure 3.8). In cases where flow factor is low, the zone immediately adjacent to the stress-drop experiences failure, but far from the stress drop, the slope is essentially unaffected. This is consistent with observations of 'pinnacle' failure blocks near a prominent headscarp in the Gulf of Mexico (Sawyer et al, 2009).

From my experiments I elucidate relationships between the initial flow factor and the resulting mudflow dynamics and morphology (Figure 3.12). Peak flow velocity, runout distance, and volumetric discharge decrease with decreasing values of F_f (Figure 3.12A, B, C). This is because as F_f decreases, the pre-failure material becomes stronger relative to the imposed shear stress. This suggests that if the shear stress is more than twice the material yield strength, the mudflow can rapidly transport a large volume of material far from the source area. Below this threshold a mudflow will deposit a relatively low volume of material close to the source area. A more complex relationship exists for aspect ratio (L:W), deposit thickness, and mudflow duration (Figure 3.12 D,E, F). The deposit aspect ratio is less than 1 for low F_f ($F_f < 2$), indicating the longest dimension is perpendicular to flow. Aspect ratio is greater than 1 for medium and high F_f, indicating that the deposit is longer in the flow-parallel direction. The peak in aspect ratio (Figure 3.12C) (experiment 3) is caused by lateral levees that funneled material in the downdip direction while simultaneously restricting lateral growth (Figure 3.6D). At higher values of F_f, the material yield strength is weak enough that the deposit can expand in the strike direction nearly as much as it can in the downdip direction (and no levees are formed), which results in aspect ratio only slightly above 1. Deposit thickness increases slightly between experiment 2 and 3 but decreases for higher F_f. This makes intuitive sense because yield strength decreases as F_f increases. Finally, mudflow duration is short at low and high F_f values and peaks at medium F_f values. The peak value (experiment 3) reflects the retrogressive failure that lasted nearly 12 minutes. This suggests the longest duration flows correspond to retrogressive failure. If the initial flow factor is too high, or too low, retrogressive failure cannot occur.

The wide contrast in release mechanism (Figure 3.6), evacuation rate, (Figure 3.7) and depositional style are important because knowledge of the initial slide acceleration and volume are critical components for modeling of the magnitude of slide-generated tsunami and impact force on pipelines (Bondevik et al., 2005; Løvholt et al., 2005; Zakeri et al., 2008). I observed two fundamentally different release mechanisms: the high F_f experiment resulted in a high-velocity, high-volume flow and deposited *en masse*, most of which occurred in the first 10 seconds (Figure 3.7). In contrast, the medium F_f mudflow was a slow-velocity, low-volume retrogressive flow that constructed the final deposit as piece-by-piece accumulation of ~100 small detached blocks over a period of 11.8 minutes (Figure 3.7). It is common to assume the total volume of a slide deposit was deposited by a single body, however in light of the retrogressive failure, it is clear that this assumption is not correct for retrogressive events.

Many of the world's large mass-transport deposits (MTDs) display a combination of features observed in my low, medium, and high F_f experiments. For example, MTDs off the Canary Islands (Masson et al., 2002; Urgeles et al., 1997), in the Gulf of Mexico (McAdoo et al., 2000; Sawyer et al., 2009), and Storegga and other areas offshore Norway (Bryn et al., 2005; De Blasio et al., 2005; Gauer et al., 2005; Kvalstad et al., 2005), have headscarp regions that are characterized by a broad zone of normal faults (similar to experiment 3) that disintegrated into liquefied long runout flows (similar to experiment 1). However, in my experiments, the broad zone of normal faults in experiment 3 did not spawn liquefied long-runout flows and the liquefied flow of experiment 1 did not spawn from a retrogressive release mechanism in the source area. A key difference is likely because strain weakening of natural sediments has been shown to play a significant role in the post-failure behavior and morphology of large MTDs (Kvalstad et al., 2005; Sawyer et al., 2009). These soils weaken after peak strength is exceeded, which allows long runout flows to evolve from a low F_f state to a high F_f state. When failure initiates, flow factor is low because the shear stress has just exceeded the peak shear strength, which forms fault blocks. However, as strain continues, these materials progressively weaken under the imposed stress, which increases the flow factor (eq. 1), and allows the material to evolve into long runout flows.

I suggest that the ratio of the driving stress to the resisting strength (F_f) can be a useful metric for interpreting, in a relative sense, the linkage between flow transport behavior and deposit morphology. However, scaling-related issues are inherent to geomorphic experiments that use small-scale laboratory experiments to infer field-scale processes (De Blasio et al., 2004; Ilstad et al., 2004; Mohrig et al., 1999; Paola et al., 2009; Parsons et al., 2001). The low stress levels imposed in my set-up means that cohesion is potentially a significant component of slurry strength. In natural scale flows involving 10s-100s of meters of vertical thickness, cohesion is negligible compared to the frictional component. However, I only focus on the magnitude of the yield strength as it relates to the shear stress. It is the ratio of these that dictates flow behavior and morphology in my experiments. In addition, the experimental slurries are not strain weakening soils, which may be a significant factor controlling morphology and transport style of large-scale retrogressive MTDs. The ‘dam-break’ flow triggering mechanism used in my experiments is not the most relevant to natural triggering mechanisms but my main goal was to hold the release mechanism constant while exploring a range of deposit strengths. Finally, I rely on the concepts of Paola et al (2009) that, although most geomorphic experiments are not dynamically scaled, they do simulate spatial geometry and kinematics of natural systems and therefore can illuminate the critical linkages between landscape evolution and sedimentary processes.

3.6 CONCLUSIONS

These experiments illuminate how the difference between yield strength and flow-inducing shear stress controls mudflow dynamic behavior and deposit morphology. When this difference is small, yield strength and shear stress are nearly equal, which results in a slow moving, low-volume, mudflow that retrogressively fails from the source area. The deposits grow piecewise as each fault block detaches from the source and accumulates at the back of the deposit. As the difference between yield strength and shear stress increases, mudflows become progressively weaker and thus produce longer-runout, higher-volume flows. The flows move, and emplace, as a single body. Detailed analysis of deposit morphology can yield important clues to the depositional history of the flow. Although the experiments are presented separately according to flow factor, it is clear that natural mudflows and slope failures often display the entire continuum of behaviors observed in these experiments. In summary, this work has important implications for hazards assessments, including slide-generated tsunami modeling, which rely heavily on the initial release mechanism and volumes of the slide.

3.7 ACKNOWLEDGEMENTS

I thank the University of Texas GeoFluids Consortium and the Jackson School of Geological Sciences for financial support. I conducted my experiments at the University of Texas Morphodynamics Lab. Aymeric Peyret instructed me on operating the viscometer and Glen Baum calibrated the viscometer. I thank John Shaw and Bryant Kopriva for designing and constructing the slotted aluminum tank I used for the mudflow experiments.

Exp.	F_f	High Med Low	ε_c	Classification	w	ϕ	Gs	γ_b	ρ_b	τ_g	τ_y
			%		%	%		kN/m^3	g/cc	Pa	Pa
1	6.23	High	37	Clayey silt	107	74	2.63	4.19	1.43	71.65	11.5
2	3.53	Med	37	Clayey silt	82	69	2.63	5.17	1.52	86.57	24.5
3	3.05	Med	77	Clay	150	79	2.60	3.21	1.33	54.85	18.0
4	1.91	Low	77	Clay	130	77	2.60	3.58	1.36	61.16	32.0
5	1.38		37	Clayey silt	67	64	2.63	5.80	1.59	99.24	72.0
6	0.95		77	Clay	107	74	2.60	4.16	1.42	71.07	75.0

Table 3.1: Physical properties of flow experiments:.
Flow factor (Ff) is the ratio of gravitational driving stress (τ_g) to yield strength (τ_y), clay fraction (ε_c) reported as the percent of solid mass composed of clay-sized particles (< 2μm), water content (*w*), porosity (ϕ), specific gravity (Gs), and buoyant unit weight (γ_b). Grain size classification is according to Shepard, 1954. Gs is the specific gravity of the mixture weighted according to the mass fraction of kaolin clay (Gs = 2.59) and silica silt (Gs = 2.65).

Symbol	Definition	Dimensions
F_f	Flow Factor	Dimensionless
τ_D	Driving Shear Stress	M/LT^2
τ_R	Resisting Shear Strength	M/LT^2
ε_c	Clay Fraction	Dimensionless
w	Water Content	Dimensionless
τ_y	Yield Strength	M/LT^2
K	Herschel-Bulkley apparent viscosity	M/LT
n	Herschel-Bulkley exponent	Dimensionless
γ	Shear Strain Rate	s^{-1}
τ_g	Gravitational Shear Stress	M/LT^2
z	Bed thickness	L
F_{R_d}	Densimetric Froude number	Dimensionless
θ	Bed slope	$\circ$
ρ_b	Bulk density of slurry	M/L^3
ρ_w	Density of water	M/L^3
γ_b	Buoyant unit weight	M/s^2L^2
h_a	Flow thickness	L
v_p	Peak flow velocity	L/T
v_a	Average flow velocity	L/T
$\%vol$	Volumetric discharge from source area (% of original)	Dimensionless
g	Gravitational acceleration	L/T^2

Table 3.2: Nomenclature

Exp	F_f	**Event Duration***	**Flow Vel.** v_p, v_a**	**Max. deposit runout (L)**	**L:W**	**Max. deposit thickness**	**Turbidity current?**	**Volume evacuated (% of original)**	**Source area features**	**Deposit features**
		Minutes	cm/s	cm		cm		%		
1	**6.23**	**2.5**	**16.3 1.0**	**140.4**	**1.3**	**1.5**	**Yes, prominent**	**78**	**Relatively Smooth, subtle fractures**	**Smooth, flat, lobate deposit, subtle compression ridges**
2	3.53	3.4	10.7, 0.7	138.8	1.2	1.5	Yes, minor	63	Smooth, thin, subtle surface fractures	Curvilinear surface features (lateral levees), compression ridges, hydroplaned detached blocks
3	**3.05**	**11.8**	**5.5, 0.1**	**63.7**	**1.9**	**4.0**	**Yes, minor**	**40**	**Retrogressive fault blocks (100% of source area)**	**Lateral levees, compression ridges, blocky appearance**
4	**1.91**	**2.5**	**0.8, 0.1**	**10.1**	**0.4**	**4.5**	**No**	**10**	**Retrogressive fault blocks (35% of source area)**	**Short, thick lobe, suture lines in central lobe, radial tension cracks along perimeter**
5	1.38	0.5	0.2, 0.02	5.2	0.2	4.0	No	7	Frontal zone of large fault blocks (15% of source area)	Short, thick lobe, one main suture line running laterally across lobe.
6	0.95	No mudflow	0	0	0	0	No	0	No deformation	No deposit

Table 3.3: Characteristics of mudflow experiments. Experiments 1, 3, and 4 (bold rows) are characteristic of high-, medium-, and low-Ff flow types, respectively that I discuss in detail. Aspect ratio is defined as the maximum deposit length divided by the maximum deposit width. *Event duration is defined as the time over which I observed material evacuating from the source channel. **Flow velocity is estimated from time lapse overhead photos and reported as peak velocity (v_p) and average velocity (v_a, (time for the front to reach maximum runout distance)).

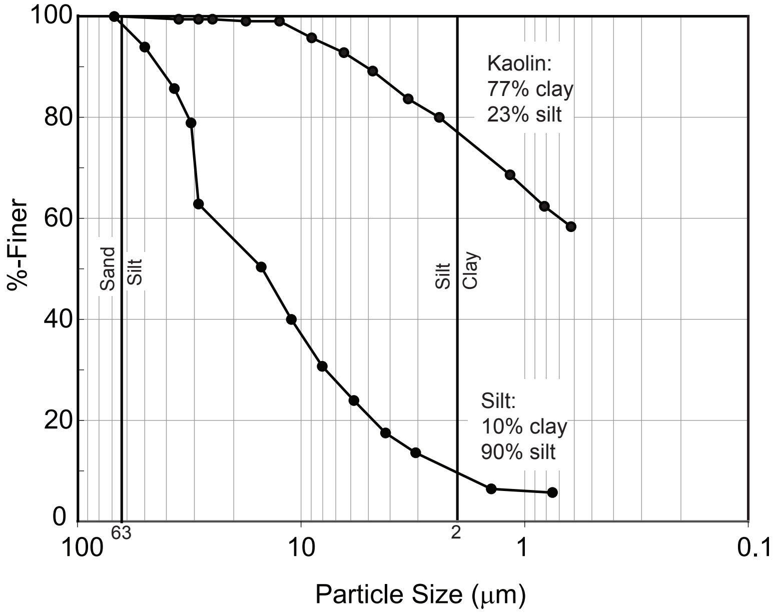

Figure 3.1. Hydrometer-derived grain size distribution of kaolin clay and silt. Silt:clay boundary is defined at 2 µm. The kaolin clay is composed of 77 % clay-sized particles and 23 % silt-sized particles. The silt is composed of 90 % silt-sized particles and 10 % clay-sized particles.

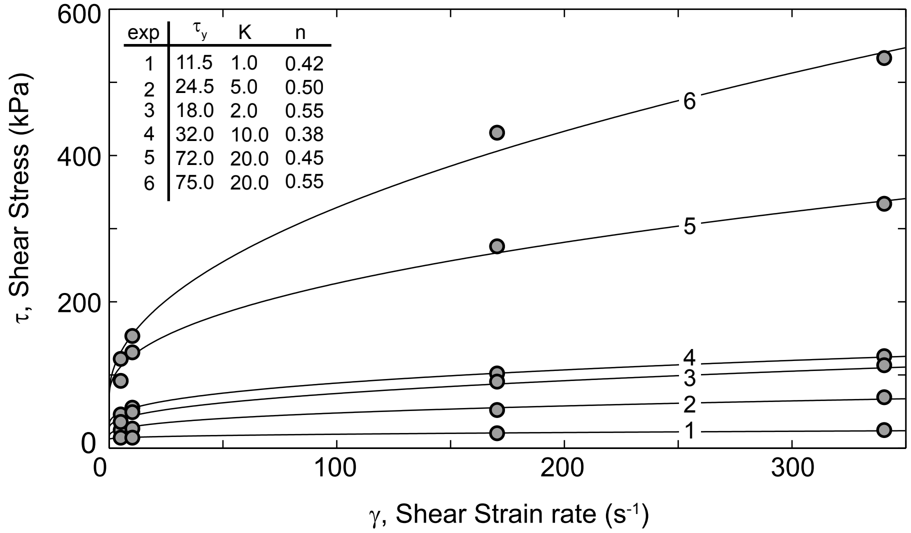

exp	τ_y	K	n
1	11.5	1.0	0.42
2	24.5	5.0	0.50
3	18.0	2.0	0.55
4	32.0	10.0	0.38
5	72.0	20.0	0.45
6	75.0	20.0	0.55

Figure 3.2: Rheology of experimental mixtures.
Viscometer data are plotted as gray circles and a Herschel-Bulkley model is fit to each test to define yield strength (τ_y) (intercept at strain rate = 0 s^{-1}).

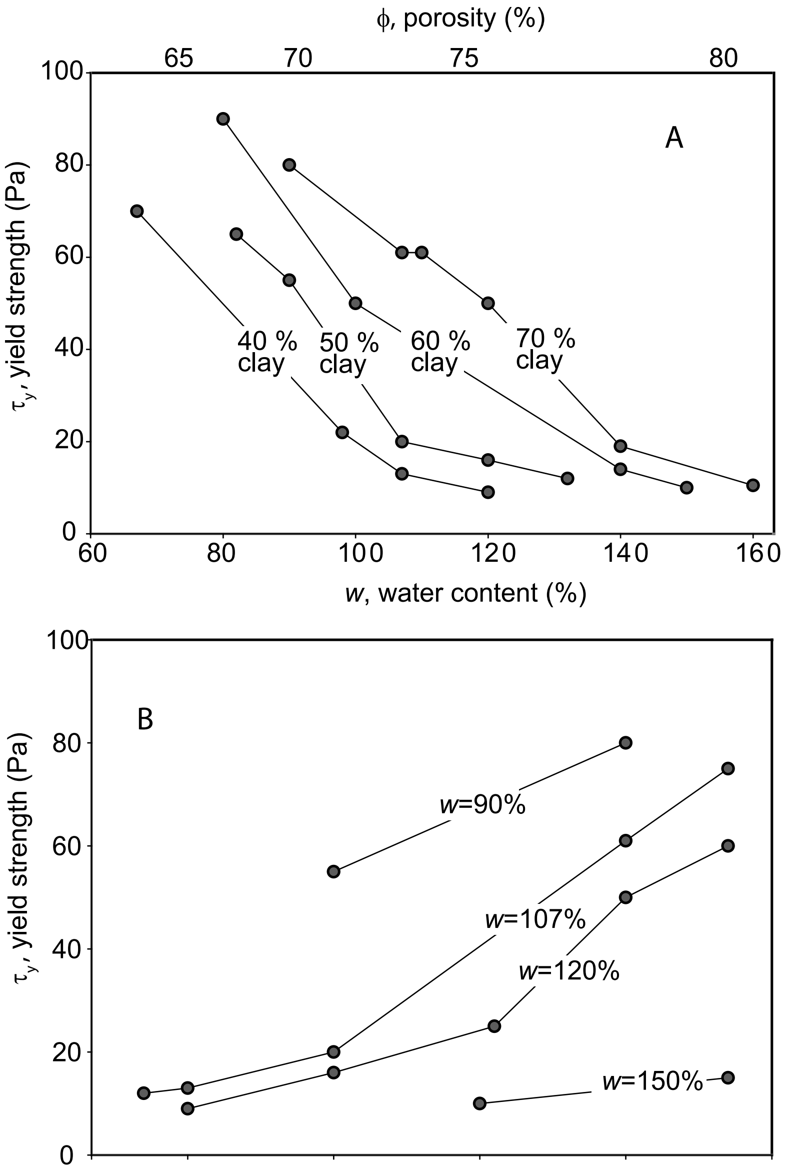

Figure 3.3: Yield strength versus (A) water content, w, and (B) clay-size fraction, for various mixtures. Yield strength is proportional to clay fraction (ε_c) and inversely proportional to water content (*w*).

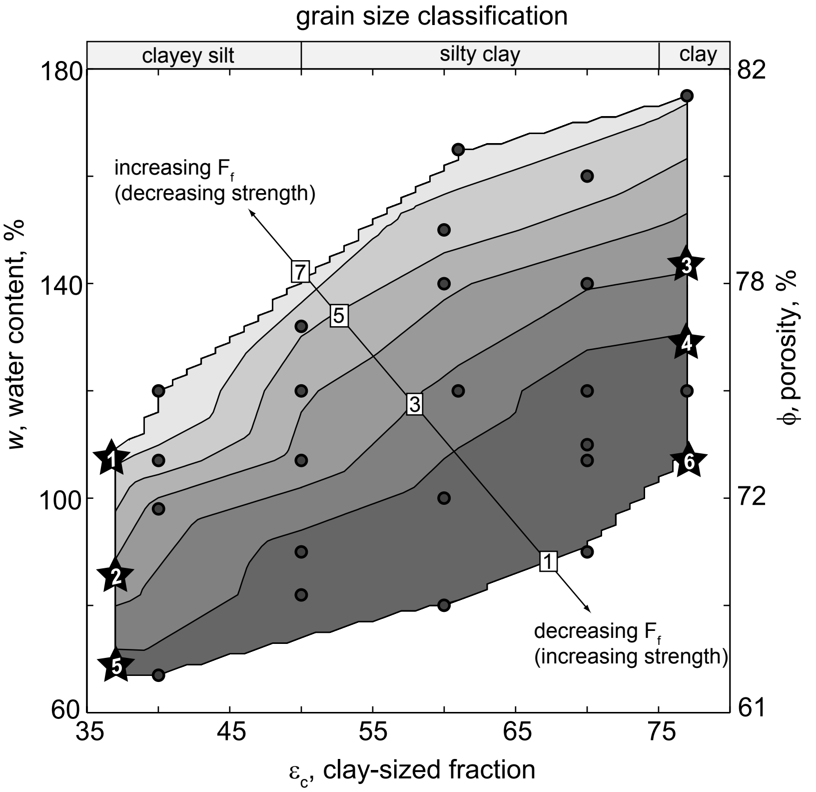

Figure 3.4: Flow factor contour plot.
Flow factor contours (labeled in white boxes) are overlain on a cross plot of clay fraction (ε_c) versus water content (w) (and porosity,). Viscometer tests are indicated as circles and mudflow experiments are indicated by numbered stars. Note that each mudflow experiment also corresponds to a viscometer test (Figure 3.2). Grain size classification is according to Shepard, 1954. Experiment 1 lies within the high flow factor zone, experiments 2 and 3 lie within the medium flow factor zone, and experiments 4-6 lie within the low flow factor zone.

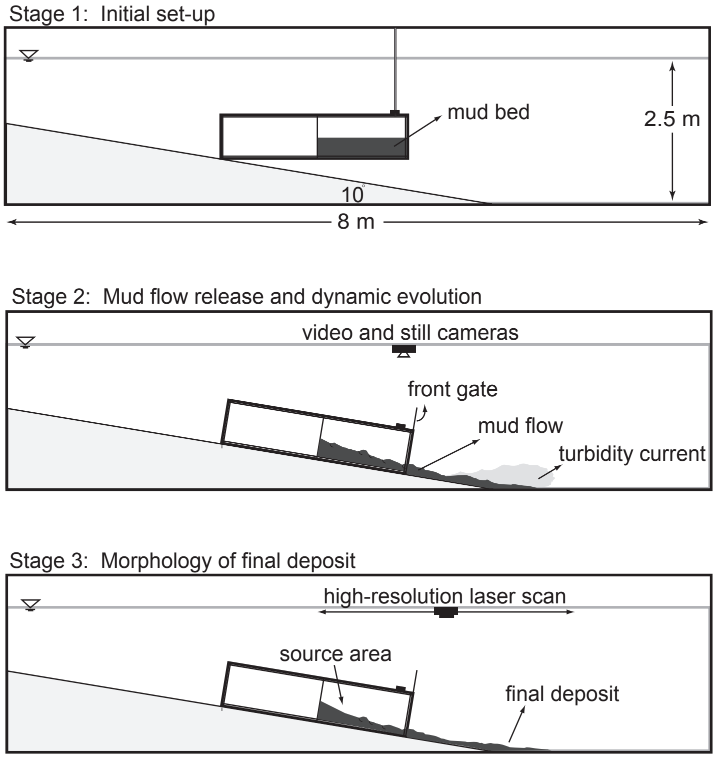

Figure 3.5: Experimental set-up and procedure.
A. Mud slurry is poured into inner tank and submerged. B. Mudflows are triggered by lowering tank onto the 10° slope and then vertically releasing front gate. Video and digital photos capture the time evolution of the resulting flow. C. The final deposit morphology of both the lobe and source area are scanned a laser with 1mm x 1mm resolution.

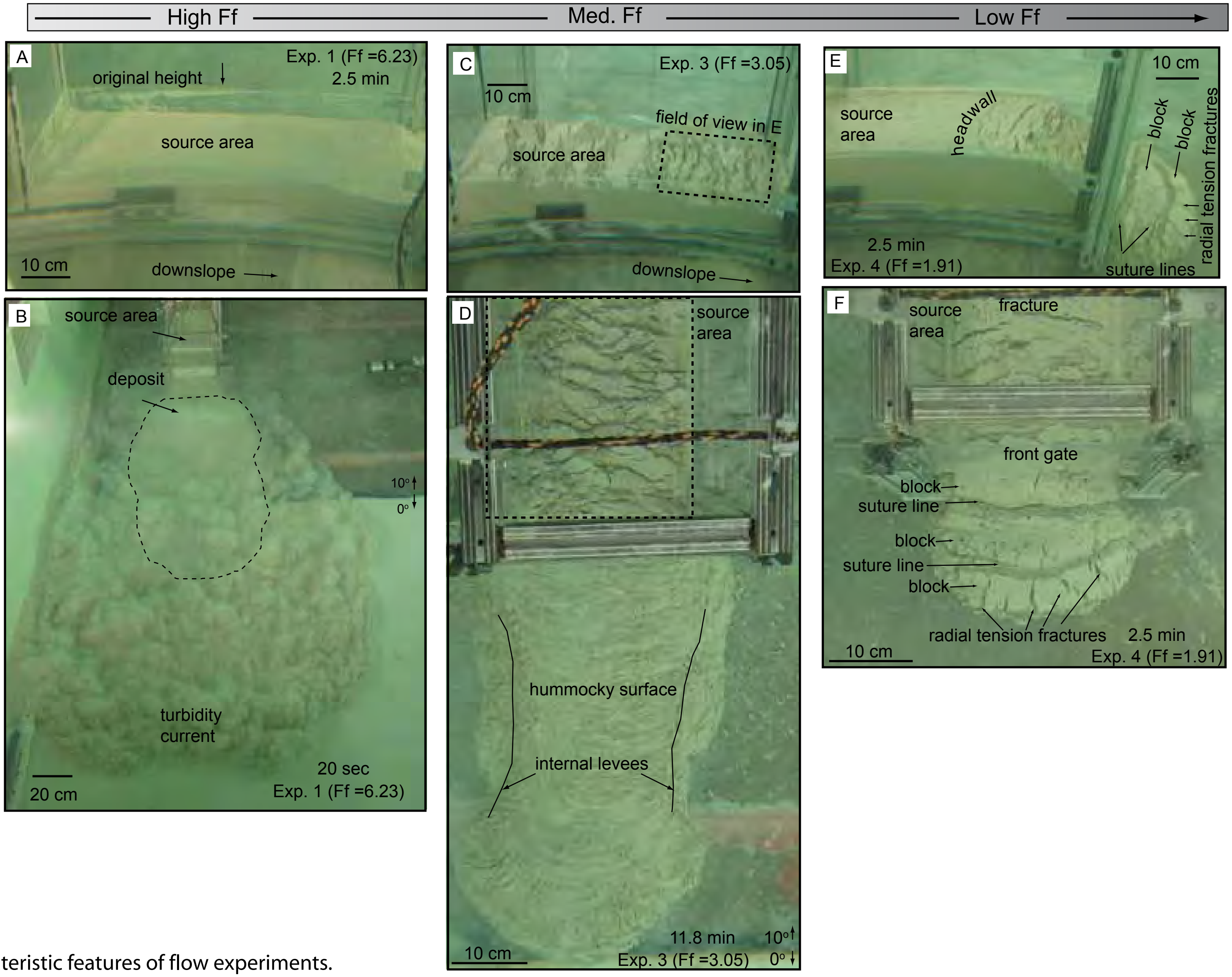

Figure 3.6: Characteristic features of flow experiments.
A, B: High F_f mudflow (experiment 1) produced a rapid mudflow that accelerated away from the source area immediately upon gate opening and produced a prominent turbidity current. C,D: . Medium F_f (experiment 3) produced a long-duration (11.8 minutes) retrogressive failure (C) that constructed a long and narrow blocky deposit (D). E,F: Low F_f (experiment 4), produced a short-duration (2.5 minutes) blocky failure. Three individual fault blocks evacuated the source area (E) and accumulated piece-by-piece in the lobe deposit (F).

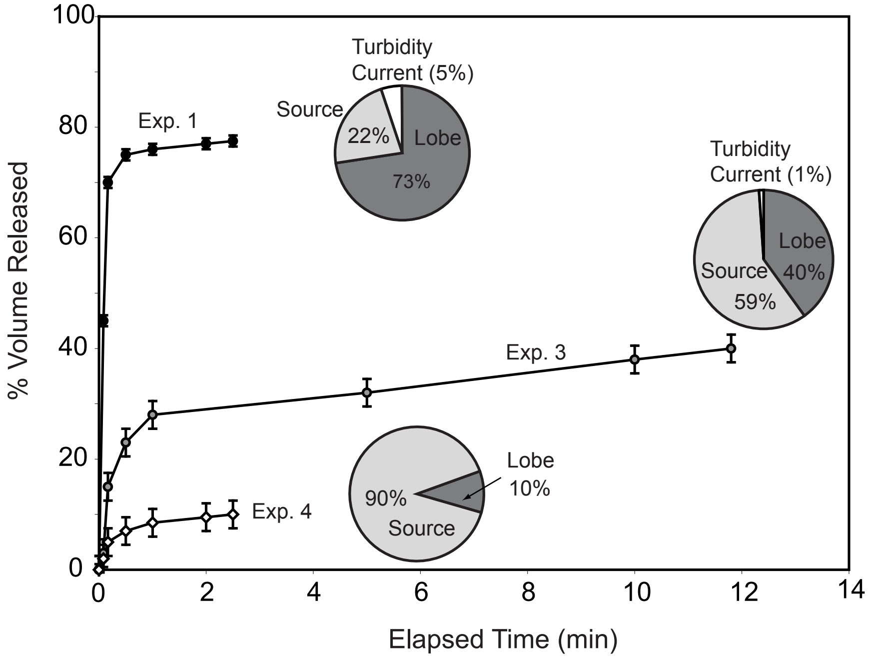

Figure 3.7: Volumetric release rate of high, medium, and low F_f mudflows.
Mudflow 1 (high F_f) occurred as a rapid pulse in which 70 % of the initial source volume released within 5 seconds including a prominent turbidity current (Figure 3.6A). Thereafter, flow rate decelerated dramatically until all flow stopped at 2.5 minutes. Mudflow 3 (medium F_f) occurred over a long period of retrogressive failure (11.8 minutes). In the first minute, 28 % of the initial source volume released and thereafter an additional 12 % released during steady retrogressive failure. Mudflow 4 (low F_f) released only 10 % of the initial source volume in slow retrogressive failure over a flow duration of 2.5 minutes.

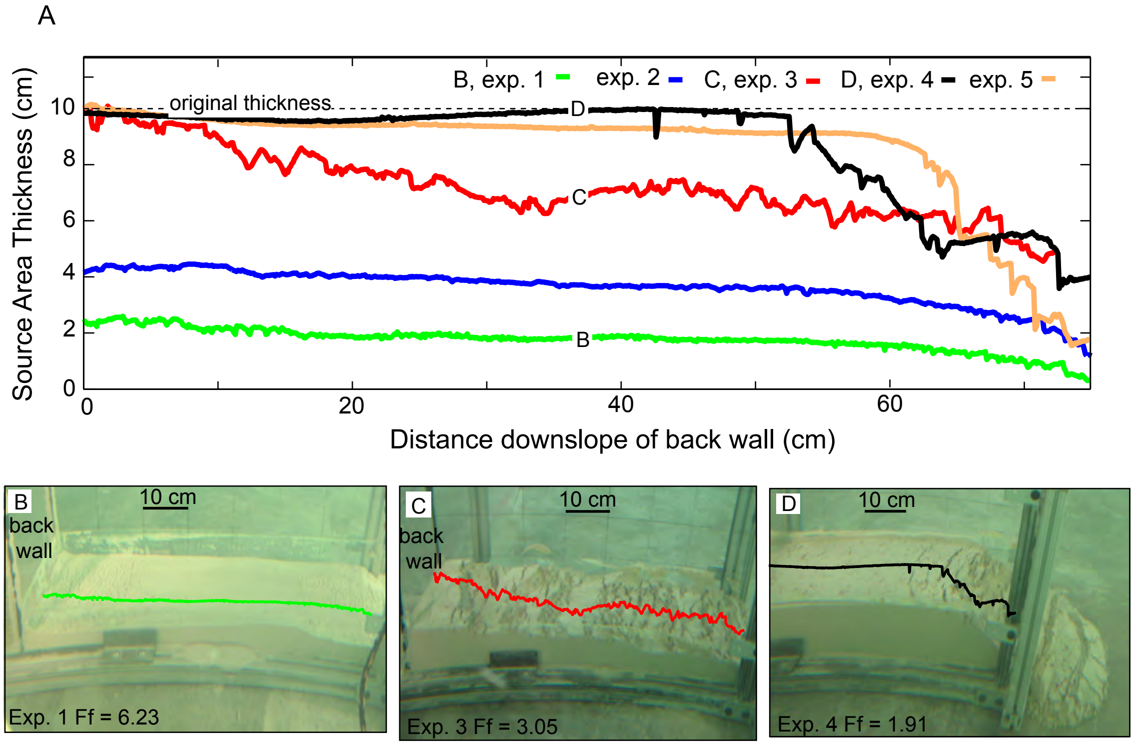

Figure 3.8: A. Source area thickness profiles and photos (B-D).
The observed surface topography is diagnostic of initial F_f: high initial F_f results in a smooth source area (green profile, photo B). A medium F_f (red profile, photo C) results in a stair-stepped morphology produced by retrogressive failure. When initial F_f is low (black, orange profiles, photo D), only the zone immediately adjacent to the stress drop experiences failure. Behind the failure zone, the bed only slightly redistributes its slope. The final thickness represents the thickness required to achieve an overall F_f of 1, which defines the end of mudflow movement.

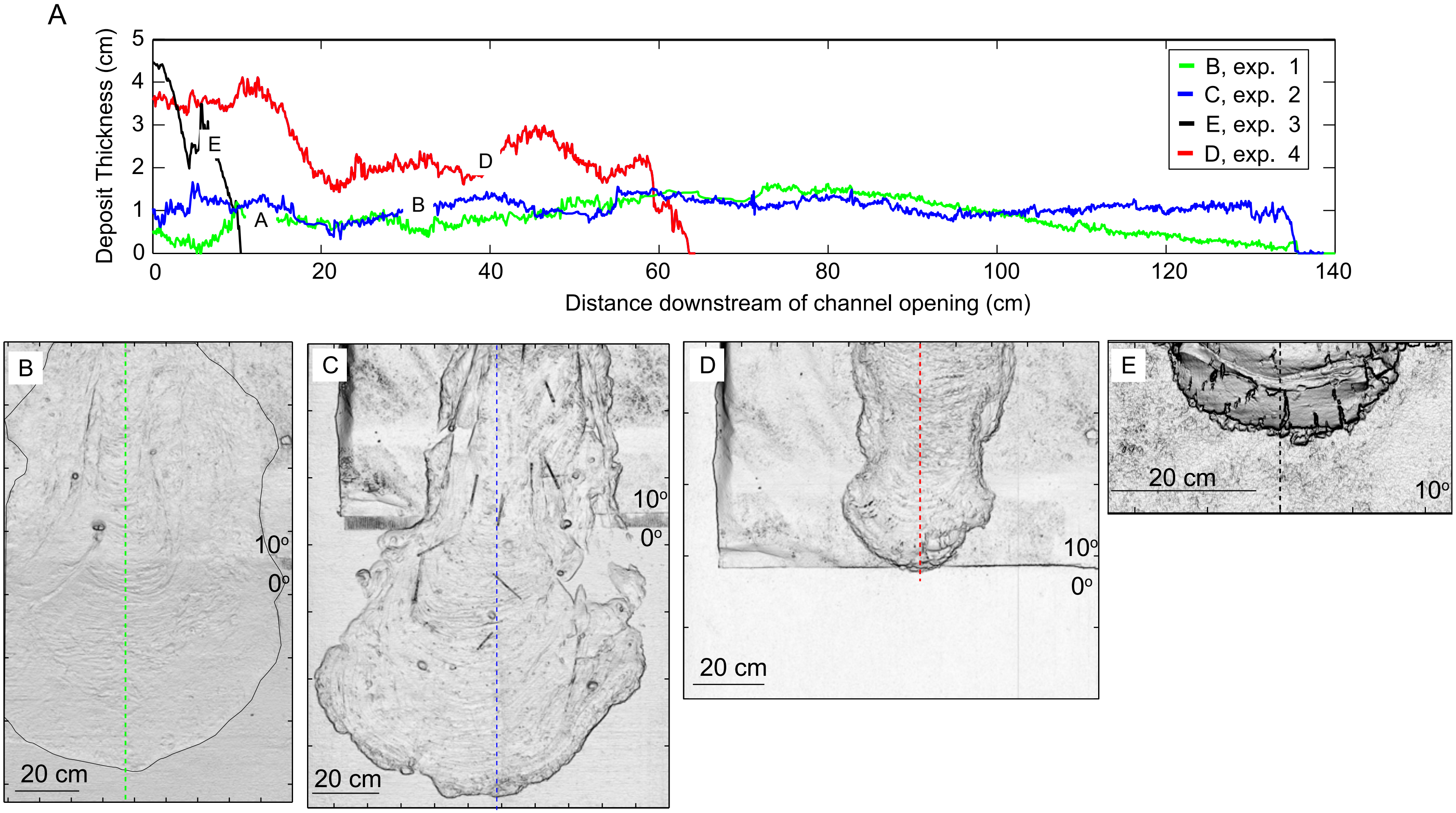

Figure 3.9: Deposit profiles and morphology.
A. Lobe thickness profiles for experiments 1-4 (experiments 5 and 6 could not be mapped with the laser). B-E. Deposit surface maps (dip maps which accentuate local variations in the surface). Cross section locations indicated by dashed line. Experiment 1 (high flow factor) is thin and broad with maximum thickness located in the central portion of the deposit at the break-in-slope. Experiments 2 and 3 show curvilinear surface flow features, internal levees, and hummocky surface topography t hat reflect retrogressive failure. Experiment 4 has a very short and thick deposit with one main suture line running laterally across the lobe where two blocks joined (Figure 5E), and radial tension features along its perimeter.

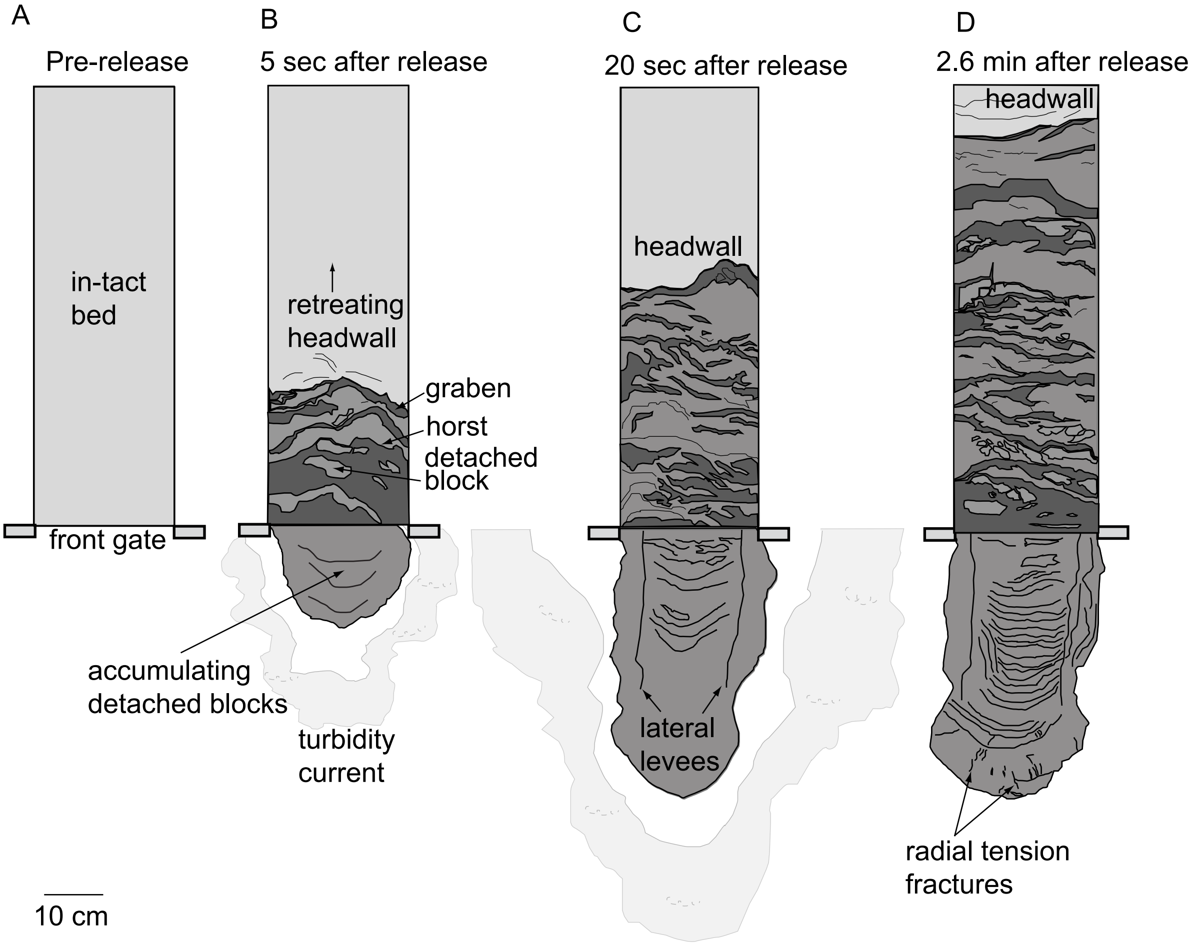

Figure 3.10: Evolution of retrogressive failure.
A-D. Line drawings from overhead time lapse photos of experiment 3. A. Pre-release configuration. B. 5 seconds after front gate is removed, the headwall is retreating as material evacuates the source area and constructs the lobe. C. 20 seconds after release, the headwall has retreated up-dip, lobe has increased in size, and lateral levees form, which restrict the lateral spreading of the deposit. D. 2.6 minutes after release, the headwall has retreated nearly to the back wall. The toe front of the deposit, beyond the lateral levees, developed radial tension features.

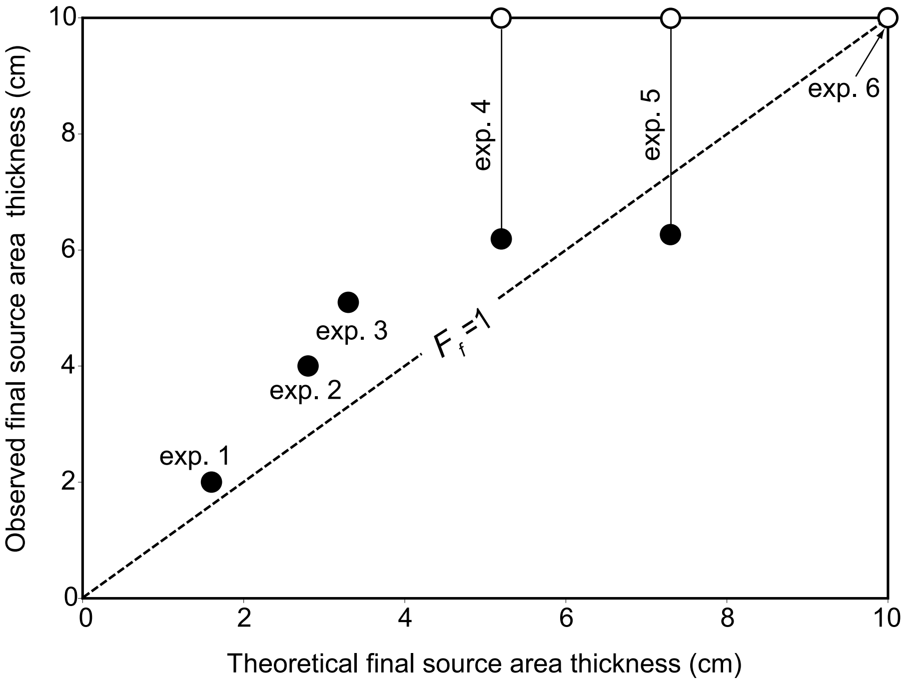

Figure 3.11: Final source area bed thickness (theoretical vs. observed). Mudflows end when the flow factor drops to a value of 1. For the observed thickness, I took the average height across the profile in Figure 8 for experiments 1-3. I calculated the final thickness by assuming a flow factor of 1 and solving for the bed thickness, z, that gave a shear stress equal to the yield strength (eq. 6). For experiments 4 and 5 the source area did not completely evacuate, therefore I plot two points for each of these experiments: the far-field thickness (white circle, 10 cm) and the mid-height of the frontal failure zone (black circles).

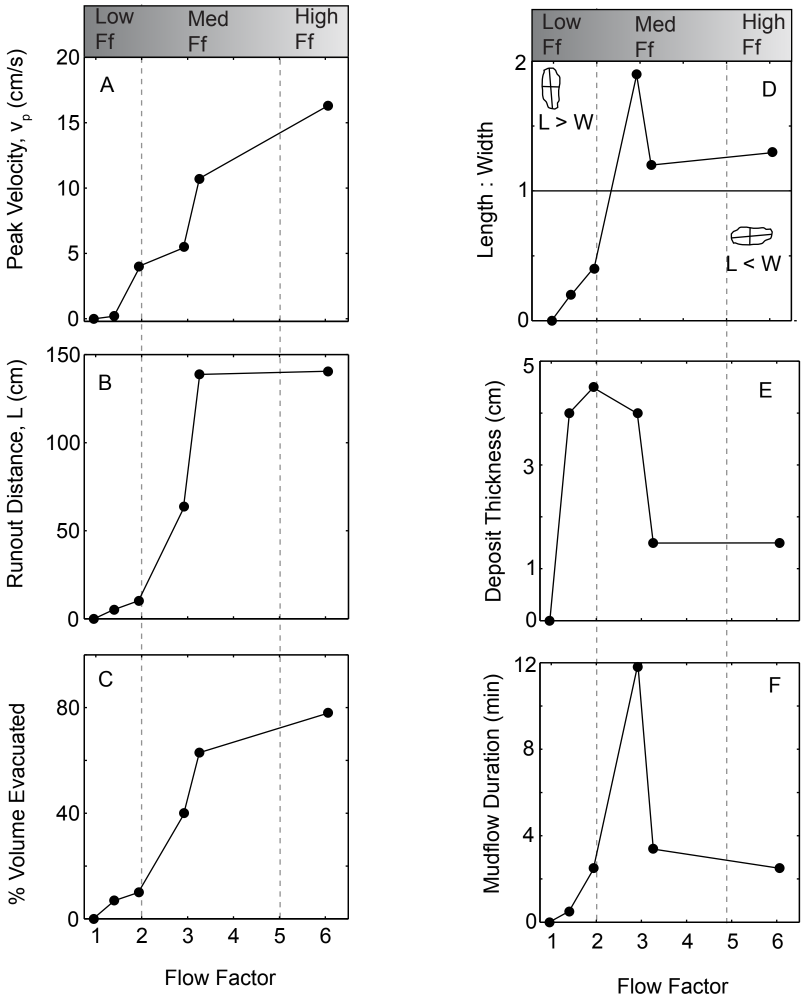

Figure 3.12: Mudflow dynamic and morphologic characteristics.
A-C). Peak flow velocity, runout distance, and % evacuated volume are proportional to flow factor. (D-F) Aspect ratio (L:W), deposit thickness, and event duration are non-linear. The peak aspect ratio and mudflow duration occurred in experiment 3 in which lateral levees directed growth in the downdip direction. and slow retrogressive failure proceeded for nearly 12 minutes.

3.8 References

Aksu, A., 1984. Subaqueous debris flow deposits in Baffin Bay. Geo-Marine Letters, 4(2): 83.

Ancey, C. and Cochard, S., 2009. The dam-break problem for Herschel-Bulkley viscoplastic fluids down steep flumes. Journal of Non-Newtonian Fluid Mechanics, 158(1-3): 18-35.

ASTM, 2007. Standard D422, Standard Test Method for Particle-Size Analysis of Soils, West Conshohocken, PA.

Bondevik, S., Løvholt, F., Harbitz, C., Mangerud, J., Dawson, A. and Inge Svendsen, J., 2005. The Storegga Slide tsunami--comparing field observations with numerical simulations. Marine and Petroleum Geology, 22(1-2): 195-208.

Bryn, P., Berg, K., Forsberg, C.F., Solheim, A. and Kvalstad, T.J., 2005. Explaining the Storegga Slide. Marine and Petroleum Geology, 22(1-2): 11-19.

Bunz, S., Mienert, J., Bryn, P. and Berg, K., 2005. Fluid flow impact on slope failure from 3D seismic data: a case study in the Storegga Slide. Basin Research, 17(1): 109-122.

Cochard, S. and Ancey, C., 2009. Experimental investigation of the spreading of viscoplastic fluids on inclined planes. Journal of Non-Newtonian Fluid Mechanics, 158(1-3): 73-84.

Coussot, P., Laigle, D., Arattano, M., Deganutti, A. and Marchi, L., 1998. Direct determination of rheological characteristics of debris flow. Journal Of Hydraulic Engineering-Asce, 124(8): 865-868.

Coussot, P. and Proust, S., 1996. Slow, unconfined spreading of a mudflow. J. Geophys. Res., 101(B11)(25): 25,217–25,229.

Coussot, P., Proust, S. and Ancey, C., 1996. Rheological interpretation of deposits of yield stress fluids. Journal of Non-Newtonian Fluid Mechanics, 66(1): 55-70.

Craig, R.F., 1992. Soil Mechanics. Chapman & Hall, London, 427 pp.

De Blasio, F.V., Elverhoi, A., Issler, D., Harbitz, C.B., Bryn, P. and Lien, R., 2005. On the dynamics of subaqueous clay rich gravity mass flows - the giant Storegga slide, Norway. Marine And Petroleum Geology, 22(1-2): 179-186.

De Blasio, R., Elverhoi, A., Issler, D., Harbitz, C.B., Bryn, P. and Lien, R., 2004. Flow models of natural debris flows originating from overconsolidated clay materials. Marine Geology, 213(1-4): 439-455.

Dugan, B. and Flemings, P.B., 2000. Overpressure and Fluid Flow in the New Jersey Continental Slope: Implications for Slope Failure and Cold Seeps. Science, 289: 288-291.

Einsele, G., 1974. Mass physical properties, sliding and erodibility of experimentally deposited and differently consolidated clayey muds (approach, equipment, and first results). In: R. Overbeck, H.U. Schwarz and G. Unsoeld (Editors), Sedimentology. Blackwell : Oxford-Boston, International, International, pp. 339-372.

Einsele, G., 1990. Deep-reaching liquefaction potential of marine slope sediments as a prerequisite for gravity mass flows? (Results from the DSDP). Marine Geology, 91: 267-279.

Elverhoi, A., De Blasio, F.V., Butt, F.A., Issler, D., Harbitz, C., Engvik, L., Solheim, A. and Marr, J., 2002. Submarine mass-wasting on glacially-influenced continental slopes: processes and dynamics. In: J.A. Dowdeswell and C.O. Cofaigh (Editors), Glacier-influenced sedimentation on high-latitude continental margins, Geological Society of London Special Publication no. 203. The Geological Society of London, London, pp. 73-87.

Embley, R.W., 1976. New Evidence For Occurrence Of Debris Flow Deposits In Deep-Sea. Geology, 4(6): 371-374.

Flemings, P.B., Long, H., Dugan, B., Germaine, J., John, C., Behrmann, J.H., Sawyer, D. and Scientists, I.E., 2008. Pore pressure penetrometers document high overpressure near the seafloor where multiple submarine landslides have occurred on the continental slope, offshore Louisiana, Gulf of Mexico. Earth and Planetary Science Letters, 269(3-4): 309-324.

Gauer, P., Kvalstad, T.J., Forsberg, C.F., Bryn, P. and Berg, K., 2005. The last phase of the Storegga Slide: simulation of retrogressive slide dynamics and comparison with slide-scar morphology. Marine and Petroleum Geology, 22(1-2): 171-178, doi: 10.1016/j.marpetgeo.2004.10.004

Gee, M.J.R., Gawthorpe, R.L. and Friedmann, S.J., 2006. Triggering and evolution of a giant submarine landslide, offshore Angola, revealed by 3D seismic stratigraphy and geomorphology. Journal Of Sedimentary Research, 76(1-2): 9-19, doi: 10.2110/jsr.2006.02

Gee, M.J.R., Masson, D.G., Watts, A.B. and Allen, P.A., 1999. The Saharan debris flow: an insight into the mechanics of long runout submarine debris flows. Sedimentology, 46(2): 317-335.

Graham, J., 1984. Methods of Stability Analysis. In: D. Brundsen and D.B. Prior (Editors), Slope Instability. Landscape Systems: A Series in Geomorphology. John Wiley & Sons Ltd., pp. 171-215.

Hampton, M.A., 1972. The role of subaqueous debris flow in generating turbidity currents. Journal of Sedimentary Research, 42(4): 775-793.

Hampton, M.A., 1996. Submarine Landslides. Reviews of Geophysics, 34(1): 33-59.

Henrich, R., Hanebuth, T.J.J., Krastel, S., Neubert, N. and Wynn, R.B., 2008. Architecture and sediment dynamics of the Mauritania Slide Complex. Marine and Petroleum Geology, 25(1): 17-33.

Hornbach, M.J., Braudy, N., Briggs, R.W., Cormier, M.-H., Davis, M.B., Diebold, J.B., Dieudonne, N., Douilly, R., Frohlich, C., Gulick, S.P.S., Johnson Iii, H.E., Mann, P., McHugh, C., Ryan-Mishkin, K., Prentice, C.S., Seeber, L., Sorlien, C.C., Steckler, M.S., Symithe, S.J., Taylor, F.W. and Templeton, J., High tsunami frequency as a result of combined strike-slip faulting and coastal landslides. Nature Geosci, 3(11): 783-788.

Huang, X. and García, M.H., 1999. Modeling of non-hydroplaning mudflows on continental slopes. Marine Geology, 154(1-4): 131-142.

Ilstad, T., Elverhoi, A., Issler, D. and Marr, J.G., 2004. Subaqueous debris flow behaviour and its dependence on the sand/clay ratio: a laboratory study using particle tracking. Marine Geology, 213(1-4): 415-438, doi: 10.1016/j.margeo.2004.10.017

Imran, J., Harff, P. and Parker, G., 2001. A numerical model of submarine debris flow with graphical user interface. Computers & Geosciences, 27(6): 717-729.

Iverson, R.M., 1997. The Physics of Debris Flows. Reviews of Geophysics, 35(3): 245-296.

Iverson, R.M., Reid, M.E. and LaHusen, R.G., 1997. Debris-flow mobilization from landslides. Annual Review of Earth and Planetary Sciences, 25: 85-138.

Johnson, A.M., 1970. Physical Processes in Geology. Freeman Cooper, San Francisco, CA.

Keller, G.H., Lambert, D.N. and Bennett, R.H., 1979. Geotechnical properties of continental slope deposits; Cape Hatteras to Hydrographer Canyon, Special Publication - Society of Economic Paleontologists and Mineralogists. SEPM (Society for Sedimentary Geology) : Tulsa, OK, United States, United States, pp. 131-151.

Kvalstad, T.J., Andresen, L., Forsberg, C.F., Berg, K., Bryn, P. and Wangen, M., 2005. The Storegga slide: evaluation of triggering sources and slide mechanics. Marine and Petroleum Geology, 22(1-2): 245-256, doi: 10.1016/j.marpetgeo.2004.10.019

Lambe, T.W. and Whitman, R.V., 1969. Soil Mechanics. Series in Soil Engineering. John Wiley & Sons, New York, 553 pp.

Lee, H. and Baraza, J., 1999. Geotechnical characteristics and slope stability in the Gulf of Cadiz. Marine Geology, 155(1-2): 173-190.

Locat, J., 1997. Normalized rheological behaviour of fine muds and their flow properties in a pseudoplastic regime. Debris-Flow Hazards Mitigation: Mechanics, Prediction & Assessment. Amer Soc Civil Engineers, New York, 260-269 pp.

Locat, J. and Demers, D., 1988. Viscosity, Yield Stress, Remolded Strength, And Liquidity Index Relationships For Sensitive Clays. Canadian Geotechnical Journal, 25(4): 799-806.

Løvholt, F., Harbitz, C.B. and Haugen, K.B., 2005. A parametric study of tsunamis generated by submarine slides in the Ormen Lange/Storegga area off western Norway. Marine and Petroleum Geology, 22(1-2): 219-231.

Major, J.J. and Pierson, T.C., 1992. Debris Flow Rheology: Experimental Analysis of Fine-Grained Slurries. Water Resour. Res., 28(3): 841-857.

Marr, J.G., Harff, P.A., Shanmugam, G. and Parker, G., 2001. Experiments on subaqueous sandy gravity flows: The role of clay and water content in flow dynamics and depositional structures. Geological Society of America Bulletin, 113(11): 1377-1386.

Martinez, J.F., Cartwright, J. and James, D., 2006. Frontally confined versus frontally emergent submarine landslides: A 3D seismic characterisation. Marine and Petroleum Geology, 23(5): 585-604.

Masson, D.G., vanNiel, B. and Weaver, P.P.E., 1997. Flow processes and sediment deformation in the Canary debris flow on the NW African continental rise. Sedimentary Geology, 110(3-4): 163-179.

Masson, D.G., Watts, A.B., Gee, M.J.R., Urgeles, R., Mitchell, N.C., Le Bas, T.P. and Canals, M., 2002. Slope failures on the flanks of the western Canary Islands. Earth-Science Reviews, 57(1-2): 1-35.

McAdoo, B.G., Pratson, L.F. and Orange, D.L., 2000. Submarine landslide geomorphology, US continental slope. Marine Geology, 169: 103-136.

Minisini, D., Trincardi, F., Asioli, A., Canu, M. and Foglini, F., 2007. Morphologic variability of exposed mass-transport deposits on the eastern slope of Gela Basin (Sicily channel). Basin Research, 19(2): 217-240, doi: 10.1111/j.1365-2117.2007.00324.x.

Mohrig, D., Elverhoi, A. and Parker, G., 1999. Experiments on the relative mobility of muddy subaqueous and subaerial debris flows, and their capacity to remobilize antecedent deposits. Marine Geology, 154(1-4): 117-129.

Moore, J.G., Clague, D.A., Holcomb, R.T., Lipman, P.W., Normark, W.R. and Torresan, M.E., 1989. Prodigious Submarine Landslides on the Hawaiian Ridge. Journal of Geophysical Research-Solid Earth and Planets, 94(B12): 17465-17484.

Morgenstern, N.R., 1967. Submarine Slumping and the Initiation of Turbidity Currents. Geotechnique: 189-220.

Moscardelli, L., Wood, L. and Mann, P., 2006. Mass-transport complexes and associated processes in the offshore area of Trinidad and Venezuela. AAPG Bulletin, 90(7): 1059-1088, doi: 10.1306/02210605052.

Mosher, D.C., Piper, D.J.W., Campbell, D.C. and Jenner, K.A., 2004. Near-surface geology and sediment-failure geohazards of the central Scotian Slope. AAPG Bulletin, 88(6): 703-723.

Mulder, T. and Alexander, J., 2001. The physical character of subaqueous sedimentary density flows and their deposits. Sedimentology, 48: 269-299.

Mulder, T., Berry, J.A. and Piper, D.J.W., 1997. Links between morphology and geotechnical characteristics of large debris flow deposits in the Albatross area on the Scotian Slope (SE Canada). Marine Georesources & Geotechnology, 15(3): 253-281.

O'Brien, J.S. and Julien, P.Y., 1988. Laboratory Analysis of Mudflow Properties. Journal of Hydraulic Engineering, 114(8): 877-887.

Orange, D.L., Saffer, D., Jeanjean, P., Al-Khafaji, Z., Riley, G. and Humphrey, G., 2003. Measurements and Modeling of the Shallow Pore Pressure Regime at the Sigsbee Escarpment: Successful Prediction of Overpressure and Ground-Truthing with Borehole Measurements, Offshore Technology Conference, pp. 1-11.

Paola, C., Straub, K., Mohrig, D. and Reinhardt, L., 2009. The "unreasonable effectiveness" of stratigraphic and geomorphic experiments. Earth-Science Reviews, 97(1-4): 1-43.

Parsons, J.D., Whipple, K.X. and Simoni, A., 2001. Experimental study of the grain-flow, fluid-mud transition in debris flows. Journal of Geology, 109(4): 427-447.

Phillips, C.J. and Davies, T.R.H., 1991. Determining rheological parameters of debris flow material. Geomorphology, 4(2): 101-110.

Piper, D.J.W., Farre, J.A. and Shor, A., 1985. Late Quaternary slumps and debris flows on the Scotian Slope. Geological Society of America Bulletin, 96(12): 1508-1517.

Piper, D.J.W., Pirmez, C., Manley, P.L., Long, D., Flood, R.D., Normark, W.R. and Showers, W., 1997. Mass-Transport Deposits of the Amazon Fan. In: R.D. Flood, D. J. W. Piper, A. Klaus, and L. C. Peterson (Editor), Proceedings of the Ocean Drilling Program, Scientific Results, pp. 109-146.

Pirkle, E.C., 1960. Kaolinitic sediments in peninsular Florida and origin of the kaolin. Economic Geology, 55: 1382-1405.

Pirmez, C., Marr, J., Shipp, C., and Kopp, F., 2004. Observations and Numerical Modeling of Debris Flows in the Na Kika Basin, Gulf of Mexico, Offshore Technology Conference, Houston, TX, pp. 1-13.

Posamentier, H.W., 2003. Depositional elements associated with a basin floor channel-levee system: case study from the Gulf of Mexico. Marine and Petroleum Geology, 20: 677-690.

Prior, D.B., Bornhold, B.D. and Johns, M.W., 1984. Depositional Characteristics of a Submarine Debris Flow. Journal of Geology, 92: 707-727.

Rettger, R.E., 1935. Experiments on soft-rock deformation. Bulletin of the American Association of Petroleum Geologists, 19(2): 271-292.

Rogers, K.G. and Goodbred, S.L., Mass failures associated with the passage of a large tropical cyclone over the Swatch of No Ground submarine canyon (Bay of Bengal). Geology, 38(11): 1051-1054.

Sawyer, D.E., Flemings, P.B., Dugan, B. and Germaine, J.T., 2009. Retrogressive failures recorded in mass transport deposits in the Ursa Basin, Northern Gulf of Mexico. J. Geophys. Res., 114.

Schwartz, H.-U., 1982. Subaqueous Slope Failures - Experiments and Modern Experiments. Contributions to Sedimentology, 11. E. Schweizerbart'sche Verlagsbuchhandlung (Nagele u. Obermiller), Stuttgart.

Seed, H.B., 1978. Wave-induced pore pressure in relation to ocean floor stability of cohesionless soils. In: M.S. Rahman (Editor), Marine Geotechnology. Crane, Russak & Co. : New York, NY, International, International, pp. 123-150.

Shepard, F.P., 1954. Nomenclature based on sand-silt-clay ratios. Journal of Sedimentary Petrology, 24: 151-158.

Stigall, J. and Dugan, B., 2010. Overpressure and earthquake initiated slope failure in the Ursa region, northern Gulf of Mexico. J. Geophys. Res., 115(B4): B04101.

Strozyk, F., Strasser, M., Förster, A., Kopf, A. and Huhn, K., 2010. Slope failure repetition in active margin environments: Constraints from submarine landslides in the Hellenic fore arc, eastern Mediterranean. J. Geophys. Res., 115(B8): B08103.

Twichell, D.C., Chaytor, J.D., ten Brink, U.S. and Buczkowski, B., 2009. Morphology of late Quaternary submarine landslides along the U.S. Atlantic continental margin. Marine Geology, 264(1-2): 4-15.

Urgeles, R., Canals, M., Baraza, J., Alonso, B. and Masson, D., 1997. The most recent megalandslides of the Canary Islands: El Golfo debris avalanche and Canary debris flow, west El Hierro island. Journal Of Geophysical Research-Solid Earth, 102(B9): 20305-20323.

Zakeri, A., Høeg, K. and Nadim, F., 2008. Submarine debris flow impact on pipelines -- Part I: Experimental investigation. 55(12): 1209.

Zreik, D.A., Ladd, C.C. and Germaine, J.T., 1995. A New Fall Cone Device for Measuring the Undrained Strength of Very Weak Cohesive Soils. Geotechnical Testing Journal, 18(4): 472-482.

Chapter 4

Deep-Seated Failure and Erosion of Levees in Turbidite Channels of the Upper Mississippi Fan, Gulf of Mexico

ABSTRACT

The levees of Late Pleistocene channels on the Mississippi Fan failed repeatedly along deep-seated listric faults where they rotated down into the subsurface, reemerged into the channel axis from below, and ultimately eroded down-system. Failure localized along an overpressured clay unit beneath the channel-levee system. Extensional fault surfaces linked the levee crest with thrust faults that emerged in the channel from below. A steady state system evolved where sedimentation on the levee was accommodated by displacement along the fault and erosion of toe thrusts by turbidity flows. Thus sediment was temporarily deposited on the levee but eventually conveyed through the failure zone and flushed down-system. I forward model the initiation of deep-seated failures with a finite element code (PLAXIS) calibrated with inputs of geometry, and material properties constrained from seismic reflection data and Integrated Ocean Drilling Program Expedition 308 data. I find that deep-seated failure originated within overpressured clay. The deep clay was loaded rapidly by the sand, which induced overpressure in the deep clay. The additional surcharge of the thick levee triggered deep-seated failure that localized just beneath the sand/clay boundary. A fascinating stratigraphic consequence of base failure is the violation of the Law of Superposition in which older strata are exhumed and emplaced above younger strata. This study illuminates the linkages between sedimentation, erosion, and the mechanical stability of channel-levee systems on modern and ancient deep-sea fans.

4.1 INTRODUCTION

Submarine channel-levee systems are primary constructional elements on the world’s deep sea fans including the Mississippi (Bouma et al., 1985; Weimer and Buffler, 1988), Amazon (Damuth et al., 1983a; Damuth et al., 1983b), Bengal (Emmel and Curray, 1985), Niger (Deptuck et al., 2007; Heinio and Davies, 2007), Zaire (Babonneau et al., 2002; Droz et al., 2003; Gervais et al., 2001; Migeon et al., 2004), Mauritania (Zühlsdorff et al., 2007), Indus (McHargue and Webb, 1986), and South China Sea (Shengqiang et al., 2009). They transport mud, sand, and gravel from the continental margin to the deep ocean (Bouma et al., 1985; Normark, 1970; Pirmez, 2003). Within a single channel-levee system, relatively coarse sediment is confined within the channel axis, and relatively fine-grained sediment constructs gull-wing shaped levees that thin away from the channel (Flood and Damuth, 1987; Kane et al., 2009; Peakall et al., 2000; Pirmez, 1994; Straub and Mohrig, 2008). Length scales of channel-levee systems can be on the order of 100-1000 km long and 1-10 km wide. Channels can be purely aggradational with no erosion of subsurface, or highly erosional with deep excavations into the subsurface (Labourdette and Bez, 2010). Levees record Earth’s climate history (Damuth et al., 1983b; Prins and Postma, 2000; Weber et al., 1997; Zühlsdorff et al., 2007) and can be productive hydrocarbon reservoirs (Abreu et al., 2003; Hackbarth and Shew, 1994; Mahaffie, 1994; Mayall et al., 2006; Steffens et al., 2004).

Stability of levees is required for the channel to maintain an open conduit for turbidity flows. Slope failure can occur in two modes: shallow-seated slope failure or deep-seated base failure. In slope failure, sidewall sediment fails directly into the channel and the failure plane intersects at, or above, the toe-of-slope (Terzaghi and Peck, 1948). Slope failures are commonly observed in seismic data (Deptuck et al., 2007; Labourdette and Bez, 2010) and in outcrops (Kane et al., 2007; Morris and Busby-Spera, 1990) of submarine channel-levee systems. In base failure, the failure plane passes below the toe-of-slope because the soil is unable to support the weight of the overlying soil and the failed material yields toward the open space (Terzaghi and Peck, 1948). Base failure has been observed in geotechnical construction of embankments and excavations (Bishop and Bjerrum, 1960; Bjerrum and Eide, 1956; Terzaghi and Peck, 1948), including the Panama Canal (Binger, 1948). Historical accounts in the Culebra Cut of the Panama Canal included railroad tracks being pushed up tens of feet from below by the toe thrusts of the deep-seated failures. Base failure has been observed in subaerial channel systems (Brooks, 2003; Laury, 1971; Williams and Flint, 1990) but the authors are unaware of published examples in submarine channel-levee systems other than those presented here.

Here I describe and forward model base failure in Late Pleistocene channel-levee systems in the upper Mississippi Fan in the Gulf of Mexico. I use a finite element soil model to simulate the initiation of base failure with soil properties constrained by core and logging data, and geometry constrained by 3-D seismic reflection data. I discuss the important role of excess pore pressure in driving base failures, and the implications for hydraulic connectivity of deepwater channel sands and the stratigraphic consequences of base failure.

4.2 BASE FAILURE IN MISSISSIPPI FAN CHANNELS

Base failures occurred in two Late Pleistocene channel-levee systems in the Ursa Region on the upper Mississippi Fan (Figure 4.1). These channels were active in the last 65 ky and lie within 300 meters of the present day seafloor where they are imaged with 3-D seismic reflection data. *Winker and Shipp* [2002], *Flemings et al.,* [2006], and *Sawyer et al.,* [2007a] describe the regional stratigraphy.

The Ursa Canyon channel-levee system is defined in seismic cross section by the high-amplitude reflections (HARs) in the channel axis and the presence of flanking levees (Figure 4.2). The channel axis is approximately 1000 meters wide and HARs are sub-horizontal and onlap the channel margin (Figure 4.2). The channel sands are surrounded by a listric fault-bounded semi-transparent seismic facies that is composed of steeply-dipping internal reflections. The angle of inclination of internal reflections increases from near-horizontal at the top of the facies, to near-vertical underneath the channel axis. The semi-transparent facies is, in turn, unique from the Blue Unit on which the channel system developed. The semi-transparent facies is composed entirely of mud, as documented by well MC 942-1, whereas the Blue Unit contains laterally continuous sands interbedded with mud, shown by well MC 899-1 (Figure 4.2). The semi-transparent facies has completely compartmentalized the Blue Unit. The total width of the Ursa channel and margin slides is approximately 5000 meters.

The listric faults occur on both margins of the channel. In cross section view, listric fault surfaces extend into the subsurface 200-300 meters to the base of the Blue Unit, become bed-parallel, and link to thrusts that reemerge into the channel axis from below (Figure 4.2). In map view, the listric faults have preserved a cuspate morphology with individual widths of approximately 500 meters (Figure 4.3). Overall however, adjacent faults linked up and formed complex cross-cutting relationships. The result is a zone of channel-margin slides that occur along the channel margins over a ~40 km length for which we have seismic coverage (Figure 4.2).

In addition to these channel-margin slides, numerous other slope failures have occurred throughout the Pleistocence section in the Ursa Region, and their origin has been linked with high overpressure induced by rapid sedimentation (Flemings et al., 2008; Sawyer et al., 2009; Stigall and Dugan, 2010; Urgeles et al., 2009). Significant present-day overpressure was measured during Integrated Ocean Drilling Program Expedition 308 (Dugan and Germaine, 2008; Flemings et al., 2008; Long et al., in review). In the 1990s, installation of the Ursa tension-leg platform and numerous well penetrations encountered high overpressure in the Blue Unit and the underlying mud (Eaton, 1999; Ostermeier et al., 2000; Pelletier et al., 1999; Winker and Shipp, 2002). I explore the role of overpressure in the finite element modeling analysis of channel margin slides.

4.3 CONCEPTUAL MODEL OF SYSTEM EVOLUTION

Sawyer et al, (2007) presented a conceptual model of the channel-margin base failures (Figure 4.4). The Blue Unit basin-floor fan was deposited rapidly above a clay unit with laterally continuous sands and mud. The Ursa Channel system then developed in 4 phases. In Phase 1, the turbidity flows scoured the Blue Unit, which established the channel. The subsequent bypass phase involved turbidity flows that continued to erode the channel and fine-grained sediment overspill constructed thick levees on the channel margins (Figure 4.4A). In Phase 2, base failure formed in response to the weight of the levees and the lack of lateral support adjacent to the channel axis (Figure 4.4B). Each failure plane defined a foot-wall slide block that was composed of both levee and underlying Blue Unit sediment. Displacement along the fault produced a toe thrust into the adjacent channel axis. Subsequent turbidity currents eroded this material down-channel. The erosion of this toe-thrust material, coupled with continued levee growth, promoted a dynamic equilibrium: turbidity currents flushed the channel axis while simultaneously depositing new levee on the margins, thereby inducing displacement along the fault into the channel (Figure 4.4C). Fault displacement was suppressed and eventually ceased as the channel switched from a bypass phase to a fill phase. The filling and onlapping sands suppressed displacement along the fault and eventually filled the channel with onlapping sands. (Figure 4.4D).

4.4 MODEL OF SYSTEM EVOLUTION

To test the conceptual model, I use a two-dimensional finite element soil modeling package PLAXIS (Brinkgreve, 2002). PLAXIS solves the governing equation of consolidation (Biot, 1941) in response to applied loading or unloading and links soil behavior with a constitutive soil model (e.g. Mohr-Coulomb). For plane strain, the mean total stress is (p) is

$$p = \frac{\sigma_1 + \sigma_3}{2},$$

and the maximum shear stress (q) is

$$q = \frac{\sigma_1 - \sigma_3}{2},$$

where σ_1 and σ_3 are the principal stresses. The mean effective stress (p') controls soil behavior and is equal to the total stress less the pore pressure (u)

$$p' = p - u .$$

The excess pore pressure (u_e) is the pore pressure less hydrostatic pressure (u_h)

$$u_e = u - u_h.$$

For a change in total mean stress (Δp), the change in pore pressure (Δu) is

$$\Delta u = B \Delta p ,$$

where B is Skempton’s pore pressure parameter. The value of B is 1 for saturated soils, but is set to 0.99 for numerical stability in PLAXIS (Brinkgreve, 2002). The diffusion of excess pore pressure with time (t) is solved with the consolidation equation (Biot, 1941)

$$\frac{\delta u_e}{\delta t} = c_v \left(\frac{\delta^2 u_e}{\delta x^2} + \frac{\delta^2 u_e}{\delta y^2} \right).$$

For each lithology I define a single value of hydraulic conductivity (K) and compressibility (m_v), which are related to the coefficient of consolidation (c_v):

$$c_v = \frac{K}{m_v * \gamma_w},$$

where γ_w is the unit weight of water. The hydraulic conductivity is related to absolute permeability (k) by

$$k = \frac{K\mu}{\gamma_w},$$

where μ is the dynamic viscosity of water. I do not model the change in permeability or compressibility with effective stress.

To link effective stress to soil strain I used the well-known Mohr-Coulomb model (MC). MC is an elastic-perfectly plastic constitutive model in which a yield function separates elastic (recoverable) strain and plastic (irreversible) strain. Elastic strain obeys Hooke's Law of linear elasticity, with the input parameters Young's modulus (E) and Poisson's ratio (υ). The yield function is the extension of Mohr-Coulomb theory to general states of stress with the effective stress input parameters of angle of internal friction (ϕ) and cohesion (c). Non-associated flow is assumed and defined with the dilatancy angle (ψ). The angle of internal friction also defines the value of the lateral stress ratio (K_0) according to Jaky's formula ($K_0 = 1\text{-}\sin\phi$).

I define model geometry from seismic data, and lithology and material properties from cores recovered on IODP Expedition 308. The model domain is 5000 meters wide with maximum soil thickness of 1400 meters at the levee crest (Figure 4.5). From bottom to top, the model consists of a layer of clay (1000 m thick) that is overlain by a sand (150 m thick) and capped by a clay levee (200 m crest thickness) (Figure 4.5). Water depth is 1000 meters measured from the top of the sand. We do not know the initial incision depth or the original levee height. However, a horizontal line drawn from the top of the Blue

Unit to the base of the HARs in the channel axis provides a minimum incision depth of 50-75 meters. We also do not know the original levee thickness prior to base failure because of post-channel erosion by adjacent channel-levee systems. However, levee thicknesses measured in other channels in the region are on the order of 100-300 meters. For the clay lithology, I assign permeability constrained from consolidation experiments (Long et al., 2008), and shear strength from triaxial experiments (Dugan and Germain, 2009) (Table 4.1). To simplify the model, I assume that the entire Blue Unit is composed of a single sand unit and assign typical sand material properties (Table 1).

I model the depositional history in the following steps (Figure 4.5): 1) uniaxial consolidation of the deep clay, 2) uniaxial consolidation of the Blue Unit, 3) instantaneous excavation of a 75-meter deep channel with 10° sidewall angles, and 4) instantaneous deposition of a 200-meter thick levee with 10° sidewall angles. I assume plane strain conditions and vertical symmetry at the channel midline. No flow is allowed across the left, right, and bottom boundaries. No lateral displacement is allowed across the left and right boundaries, and no displacements are allowed across the right, left, and bottom boundaries. The finite element mesh is composed of 15-node elements with over 3.2×10^5 nodes. I tested sensitivity of the solution to mesh size and boundary conditions.

The most sensitive parameter controlling slope stability of the model is the development of excess pore pressure in the deep clay that underlies the Blue Unit. I first run the simulation with hydrostatic pore pressure conditions everywhere (Figure 4.5). This case simulates one end member in which sedimentation is slow enough to allow complete drainage for all loading phases. I then analyze a case in which the deep clay is allowed to develop overpressure (Figure 4.5B). To do this, I use PLAXIS to simulate instantaneous deposition of the Blue Unit followed by consolidation for 1000 years. The

Ursa Channel is excavated as an undrained unloading. Finally, the levee is deposited as an undrained loading.

4.5 RESULTS

Hydrostatic Example

Base failure is not predicted in the hydrostatic example (Figure 4.6). The geometry is not under failure but it does adjust to the imposed unloading (channel excavation) and loading (levee) by vertically consolidating beneath the levee and uplifting in the channel axis. Vertical profiles beneath the levee crest (A-A') and the channel floor (B-B') illustrate the magnitude of excess pore pressure (u_e) and hydrostatic vertical effective stress (σ_{vh}') with depth at the end of simulation. σ_{vh}' is the total vertical stress less the hydrostatic pore pressure. This difference between u_e and σ_{vh}' is the vertical effective stress σ_v'. Note the vertical profiles are plotted with respect to meters below sea level and are not updated to reflect consolidation or uplift.

The evolution of pressure and stress curing the channel excavation and levee loading is captured in the stress path plot (Figure 4.6B). Points 1 and 2 are located in the deep clay beneath the levee crest and channel floor, respectively. Before channel excavation, both points start from an initial condition on the k_0 consolidation line. This is the result of one-dimensional deposition of the deep clay and the Blue Unit. The effect of the channel excavation is most pronounced in point 2. The reduction of the vertical stress caused by the excavation (75 m) reduced the mean effective stress (p') and shear stress (q). The shear stress (q) has been reduced because the vertical effective stress drops to a value closer to the horizontal effective stress, therefore the difference decreases. Point 1 is located relatively far from the channel excavation and therefore the stress path changes only slightly up and to the left. This indicates a slight decrease in p' and a slight increase in q, driven by a slight decrease in horizontal effective stress. The loading of the levee is most pronounced in point 1.Here, the vertical stress has increased much more than the horizontal stress, which increased both p’ and q. The stress path rises up, and to the right, towards the failure envelope (Figure 4.6B). Point 2 is relatively far from the levee loading and the primary effect is an increase in the horizontal effective stress. The stress path moves only slightly down (decreasing q) and to the right (increasing p’).

Overpressured Example

Base failure occurs in the deep clay in the overpressured example (Figure 4.7). The shape of the failure surface is illustrated in the deformed mesh, although displacements are not to scale. The failure plane soles out in the deep clay layer beneath the sand. It does not extend significantly deep into the deep clay because this is the depth where the lowest effective stress occurs, shown by the vertical profiles A-A’ and B-B’. In the model the total load of the sand is applied instantaneously (undrained), thus the total stress increase is transferred directly to excess pore pressure. Without further loading, consolidation (drainage) is allowed to occur for a period of 1000 years. However, the low permeability of the clays at Ursa prohibits complete drainage to occur during this time period. As a result, only the top several meters of the clay have experienced some amount of drainage, illustrated in the slight increase in vertical effective stress beneath the sand in profile A-A’ (Figure 4.7B). If no consolidation time were allowed into the model, the lowest effective stress, and thus failure, would occur at the sand/clay interface. Furthermore, if complete consolidation was allowed, the solution would converge to the hydrostatic example and no failure would occur. For deep failure to occur, a zone of high overpressure and low effective stress must be present.

The stress path plot shows how deep-sated failure evolved (Figure 4.7B). Points 1 and 2 both start from the k_0 consolidation line, as in the hydrostatic example. The key difference in this case, however, is the sand is not included in the initial k_0 stress condition. The loading of the sand is modeled as an undrained horizontal load uniformly distributed above the deep clay. The result at both points is no change in the stress path because the sand load is applied to the pore pressure. However, the slight deviation up and to the right observed in both points is due to the consolidation phase. The excavation of the channel at point 2 resulted in a vertical drop in the stress path. The mean effective stress does not change because the unloading is applied to the pore pressure. The shear stress (q) drops because the vertical stress has decreased and the horizontal stress has not changed. At point 1, the stress path rises vertically upward in response to the excavation because the horizontal stress has dropped relative to the vertical stress. At both points, it is worth noting that that the excavation itself, even when applied instantaneously, is not enough to drive failure. Although, given a deep enough excavation, points 1 and 2 would eventually intersect the failure envelope. The subsequent instantaneous loading of the levee pushes the stress paths at both points to the failure envelope. At this point, the calculation phase terminates and no further loading or unloading can be applied.

4.6 DISCUSSION

High excess pore pressure was necessary to trigger base failure of Late Pleistocene levees in the Gulf of Mexico. If pore pressure remained hydrostatic throughout the depositional history, no base failure would have occurred (Figure 4.6). However, the low permeability clay was buried rapidly by a basin-floor fan so that excess pore pressure could not fully dissipate except for the top few meters. The subsequent excavation of the channel provided an increased in shear stress in the subsurface but not enough to induce base failure. The deposition of the levee provided the additional loading necessary to trigger failure (Figure 4.7B). Another potential process that could have contributed to excess pore pressure in the deep clay is rapid sedimentation in the clay unit itself. In a high deposition rate region such as the Ursa Region and with such low permeability clays, it is reasonable to suggest this unit could have had significant overpressure even before deposition of the basin-floor fan and channel system. If this was the case, the starting condition on the stress path plot would be farter down the k_0 line, and therefore would have less vertical distance to the failure line. In other words, deep-failure would have been achieved with less total stress changes.

The simulation captures the initiation of the system but the Ursa Canyon clearly records numerous failure planes that suggest multiple occurrences of this type of failure (Figure 4.2 and 4.3). It is also clear from seismic data that this system continued to evolve after the initial deep-seated failure. If the failures ceased after this initial stage, we would observe Blue Unit Sands in the facies penetrated at well MC942-1. The fact that the Blue Unit has been completely displaced by failed levee shows that these faults were active long enough to at least convey the entire Blue Unit vertical thickness (~200 meters), and perhaps more, through the system and ultimately downslope as proposed in Figure 4.4.

Base failure in submarine channel-levee systems is potentially a common process despite the paucity of published examples because of the common deepwater succession of a sandy basin floor fan rapidly deposited above fine-grained units and ultimately overlain by channel-levee systems (Posamentier, 2003; Winker and Booth, 2000). Therefore the geomechanical conditions required for base failure are common. However, the steady-state levee deposition- failure-erosion process that occurred in these Gulf of Mexico channels is likely to be the result of a delicate balance between erosion rate of turbidity flows to maintain an open channel and continual levee deposition to drive active displacement along the fault. If turbidity flow erosion rate is exceeded by the volumetric influx rate of failed material entering the channel, the channel axis become progressively filled and therefore susceptible to channel avulsion before a steady state can be reached. On the other hand, in very deep channels, turbidity flows may scour too deeply into the subsurface thus preventing construction of thick levees, which supply the necessary driving force for continual fault displacement. It is interesting to note that it is unnecessary to invoke a special “weak” layer at depth with unique soil properties. In fact the “weak” layer is as a result of the high pore pressure and low effective stress developed in the basal clay as opposed to having a unique mineralogy, for example.

Base failure in submarine channel-levee systems has important implications for hydraulic connectivity in deepwater reservoirs, channel avulsions, and interpreting stratigraphy. First, base failure of levees such as those observed in the Gulf of Mexico results in a low-permeable mud core that disconnects the permeable sand layers within the basin floor fan. This dramatically affects the lateral connectivity and bulk permeability structure of the sand-rich basin floor fan. In analog deepwater reservoirs, this is an important consideration when assessing reservoir connectivity. Secondly, if base failure plugs the channel, an avulsion may occur if turbidity flow erosion rate is not high enough to maintain an open channel. If frequent avulsions occur, thin sand bodies will be distributed across many short-lived channels as opposed to thick amalgamated sands within long-lived channels. The stratigraphic consequence of base failure is that older strata are exhumed and emplaced above younger strata, a violation of the Law of Superposition.

4.7 CONCLUSIONS

The levees of at least two major Late Pleistocene channels on the Mississippi Fan failed repeatedly along deep-seated failures on both sides of the channel axis. I propose a steady state system evolved where sedimentation on the levee was accommodated by displacement along the fault (at least 200 meters), and erosion of the toe thrusts by turbidity flows. Thus sediment was temporarily deposited on the levee but eventually conveyed through the failure zone and flushed down-system. Deep-seated failure was caused by high excess pore pressure (low effective stress) in a deep clay that underlies the channel system. This style of levee failure exerts a first-order control on fan morphology and the distribution of sand and mud in leveed channel zones in deep-sea fans. If slumped levees plug the channel axis, avulsion may occur and reroute sandy flows elsewhere in the fan. A stratigraphic consequence of base failure is the violation of the Law of Superposition in which older strata overlie younger strata. This study contributes to our understanding of the linkages between channel morphology, flow, and deposits in present-day and ancient submarine channel-levee systems.

4.8 ACKNOWLEDGEMENTS

I thank R. Craig Shipp and Charlie Winker (Shell) for discussions of the channel-margin slides at Ursa. Maria Nikolinakou provided expertise in both PLAXIS and soil mechanics.

Parameter	Symbol	Unit	Ursa Silty Clay	Sand
Material Model			MC	MC
Saturated Unit Weight	γ_{sat}	kN/m^3	18.6	20
Initial void ratio	e_i		1	0.5
Horizontal hydraulic conductivity	K_x	m/s	$1\text{x}10^{-10}$	$1\text{x}10^{-5}$
Vertical hydraulic conductivity	K_y	m/s	$1\text{x}10^{-10}$	$1\text{x}10^{-5}$
compressibility	mv	1/Pa	$7\text{x}10^{-7}$	$1\text{x}10^{-5}$
Coefficient of consolidation	c_v	m^2/sec	$1\text{x}10^{-8}$	$1\text{x}10^{-3}$
Young's modulus	E	kPa	$1\text{x}10^{3}$	$8\text{x}10^{4}$
Poisson's ratio	ν	-	0.3	0.3
Cohesion	c	kPa	0.5	0
Friction angle	ϕ	°	23	30
Lateral stress ratio	k_0	-	0.6	0.5

Table 4.1 Material Properties

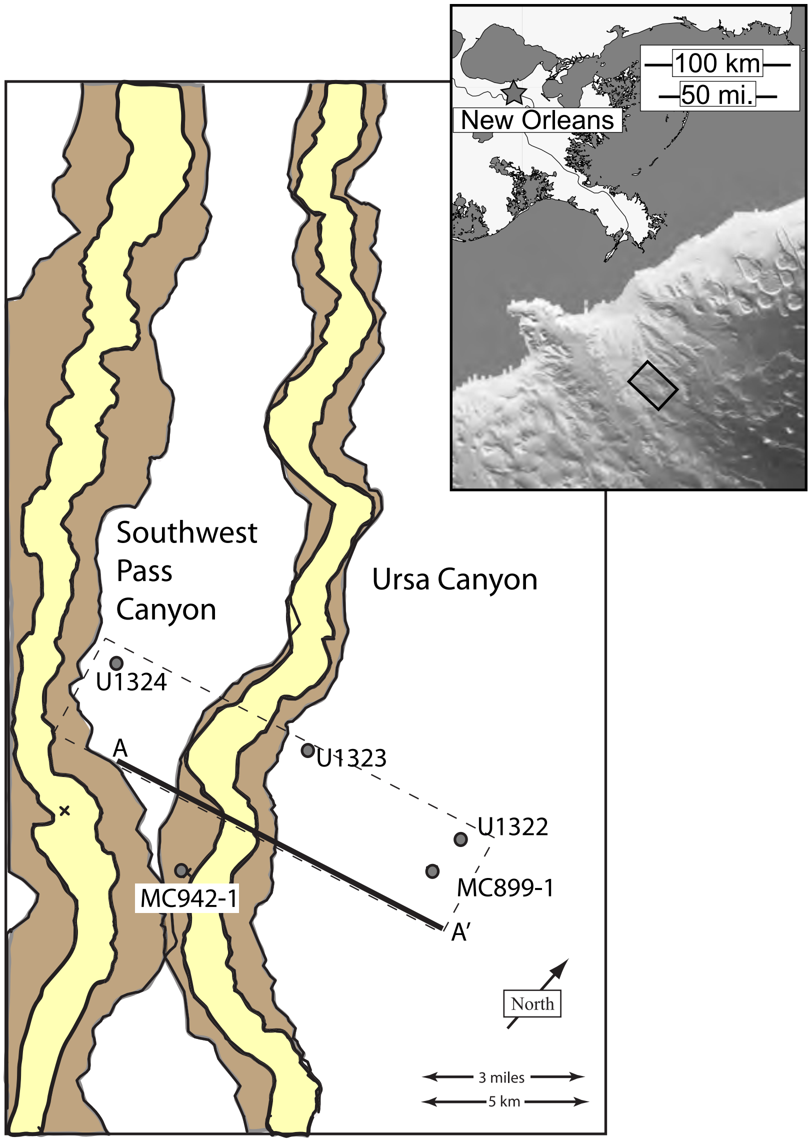

Figure 4.1
Base map of two late Pleistocene submarine channel-levee systems in northern Gulf of Mexico. The Ursa Canyon and Southwest Pass Canyon channel-levee systems contain a wide zone of channel-margin slides (light gray) that surround channel-axis sands (dark gray). Dashed polygon delineates high-resolution 3-dimensional seismic data. Circles represent industry wells and IODP Expedition 308 wells (U1324-U1322). Seismic cross-section A-A′ is shown in Figure 4.2

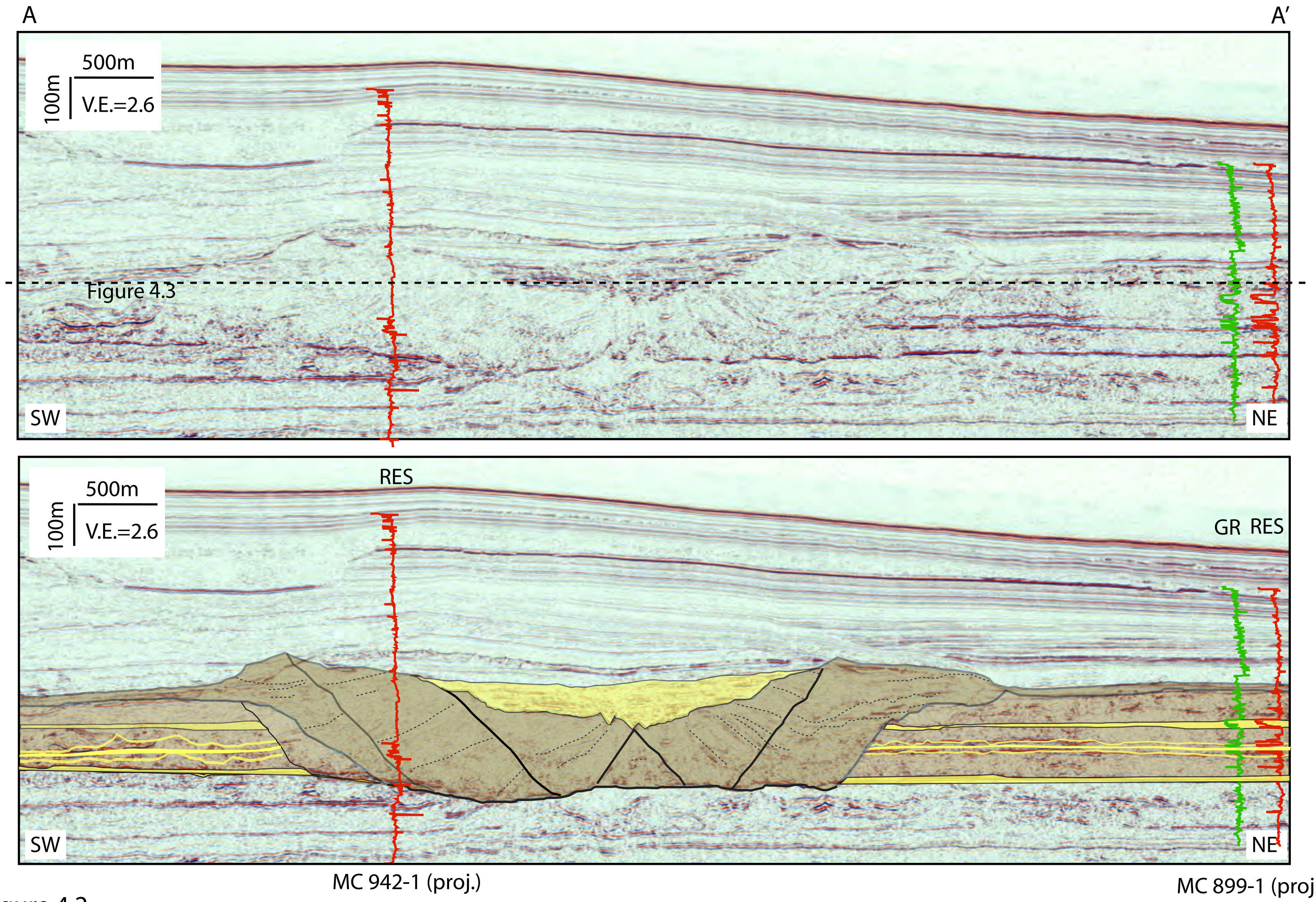

Figure 4.2
Deep-seated channel-margin slides of the Ursa Canyon are imaged in seismic cross section A-A′ and tied to industry wells. Channel-margin slides are composed of steeply dipping reflectors that are composed of mud, documented by MC 942-1. The slides zone thickness is over 200 meters and completely compartmentalizes the sandy Blue Unit basin-floor fan. A thick clay unit lies beneath the channel-levee system and Blue Unit.

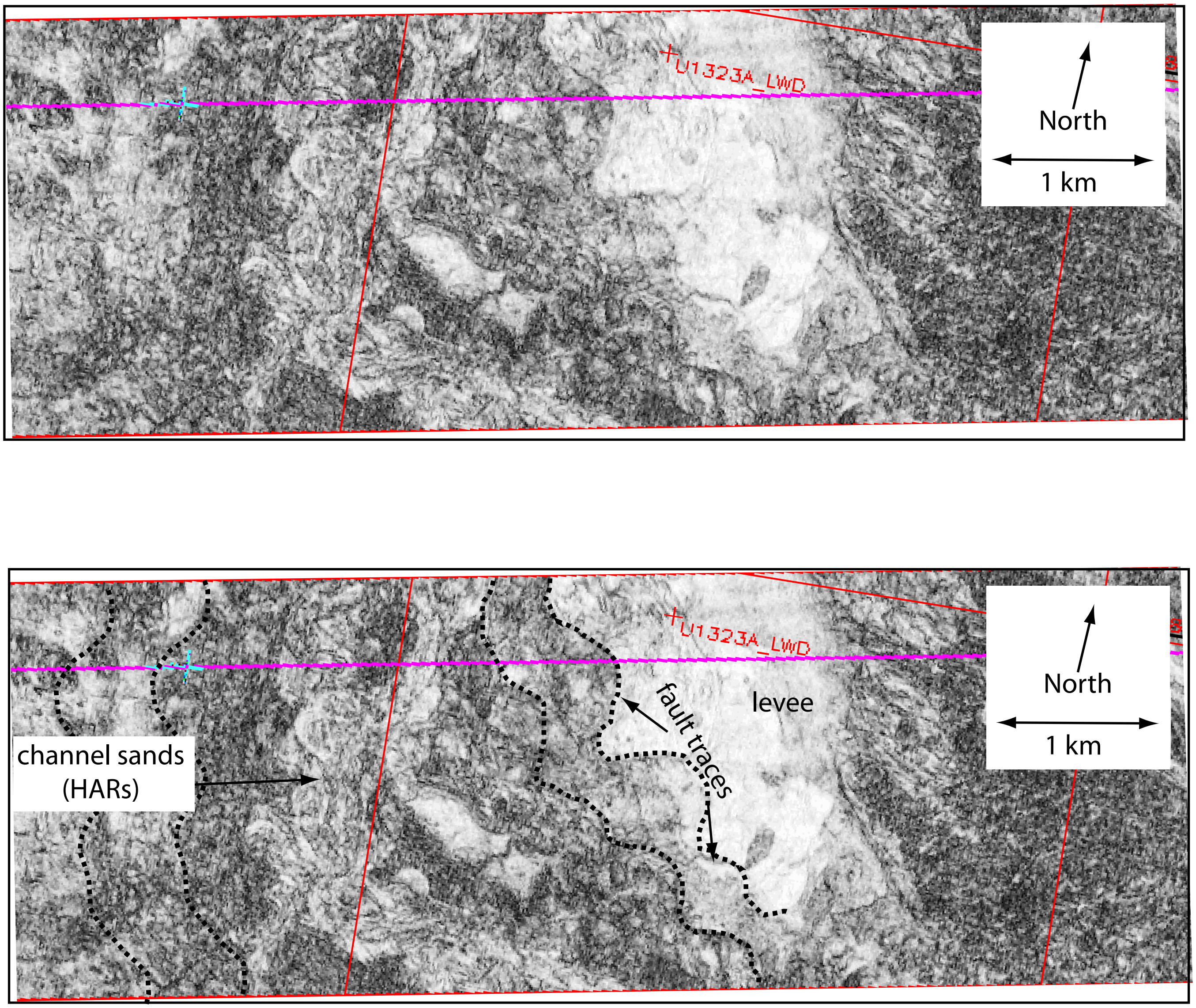

Figure 4.3
Map view of channel-levee system (time slice indicated by dashed line in Figure 4.2) shows the cuspate morphology of the listric normal faults o nthe margins of the Ursa Canyon channel-levee system. Faults bound the classic signature of channel sands (HARs).

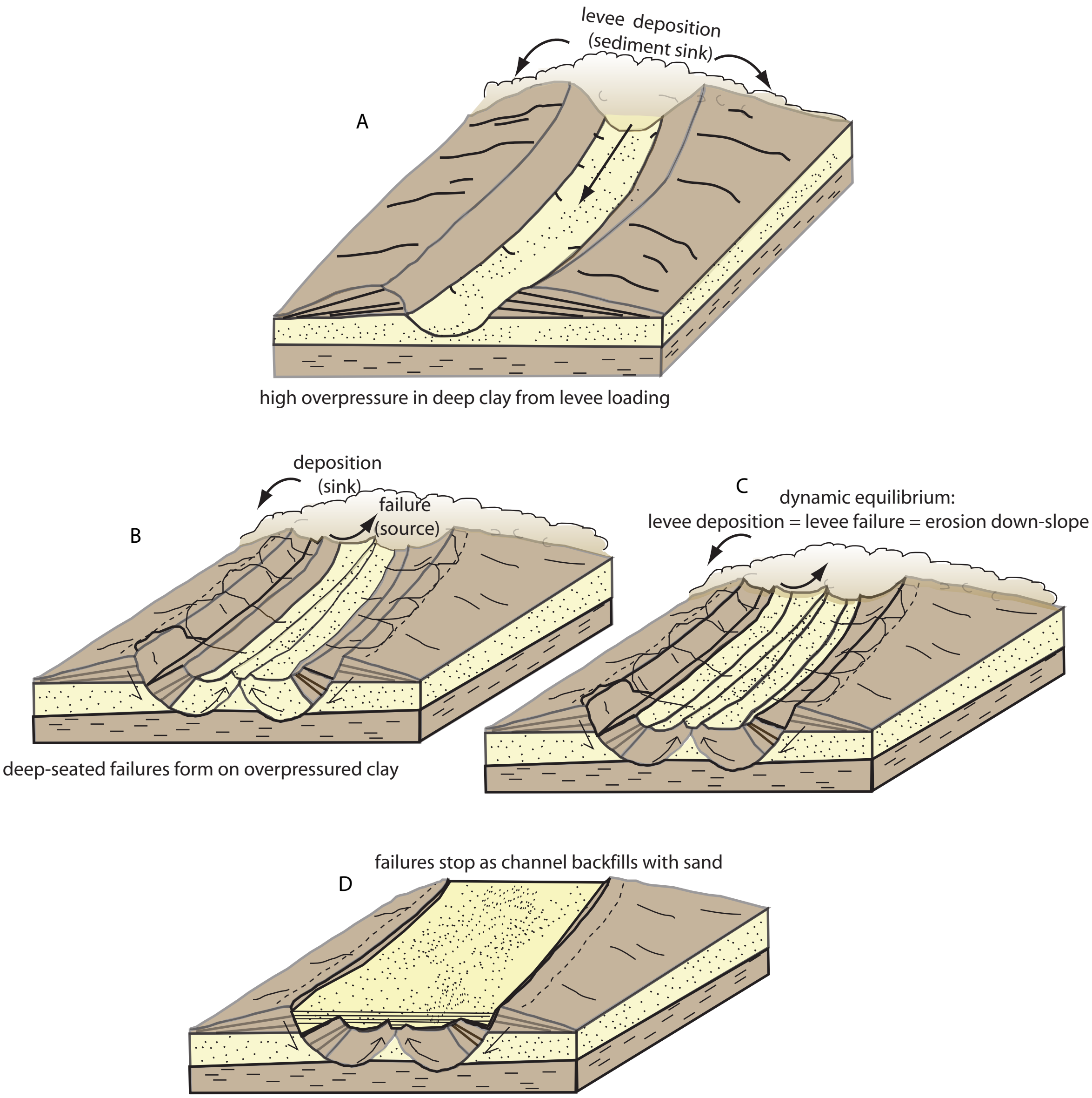

Figure 4.4
Evolution of base failure in channel-levee systems (adapted form Sawyer et al, 2007). (A) Turbidity currents incised the Blue Unit and deposited thick levees in Phase 1. (B) Weight of levees induced base failure and forced Blue Unit and levee material to slide down on circular failure planes, and force toe thrust up through the channel floor. (C) Levee growth, rotational sliding, and channel excavation continued in dynamic equilibrium to maintain a conveyor belt process in Phase 4 until the system ended (D).

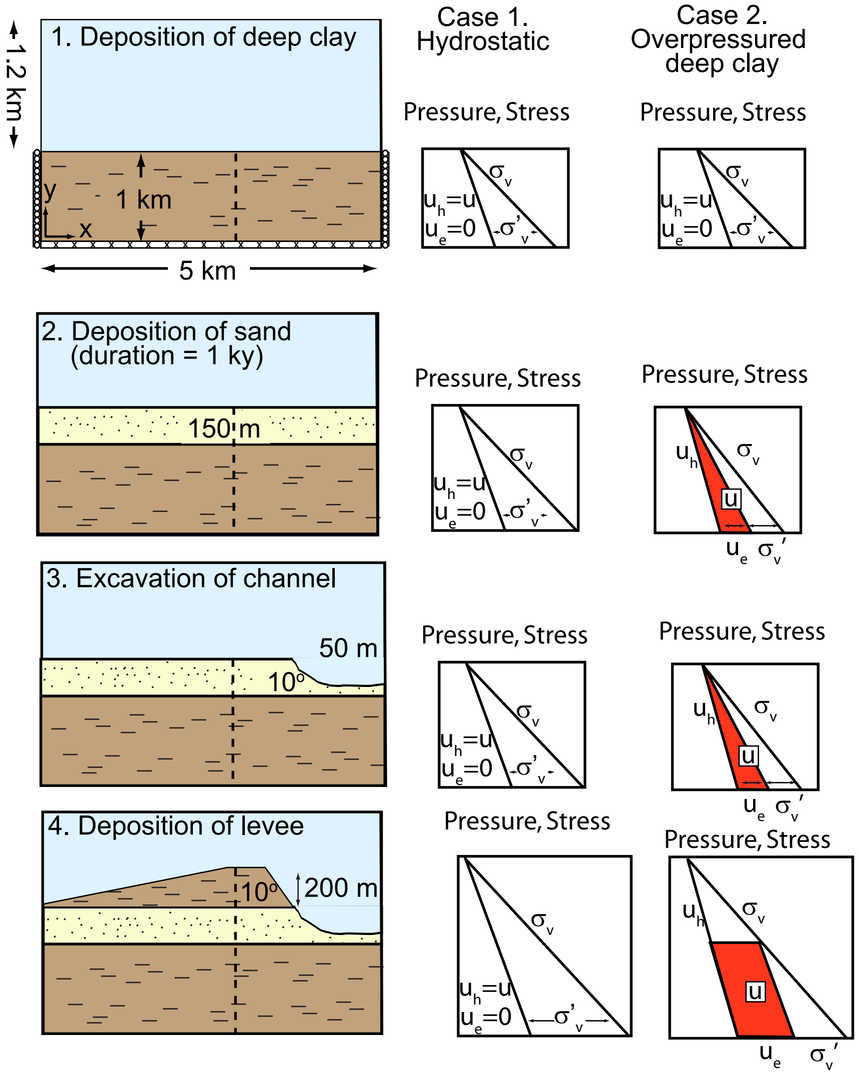

Figure 4.5 Simulation phases for forward model.
In step 1, a clay unit is deposited one-dimensionally. In step2, a sand (150 m thick) is deposited above the clay. in step 3, a 75 m deep excavation is cut in to the sand. In step 4, a 200 m thick levee is deposited above the sand and to the side of the escavation. Case 1 is hydrostatic pressure everywhere in the mdoel (no excess proe pressure). Two end member cases are simulated with respect to the pore pressure. A hydrostatic case assumes pore pressure is hydrostatic everywhere and for all loading steps. The overpressured case allows excess pore pressure to develop in the deep clay in response to the deposition of the sand unit and the loading of the channel system.

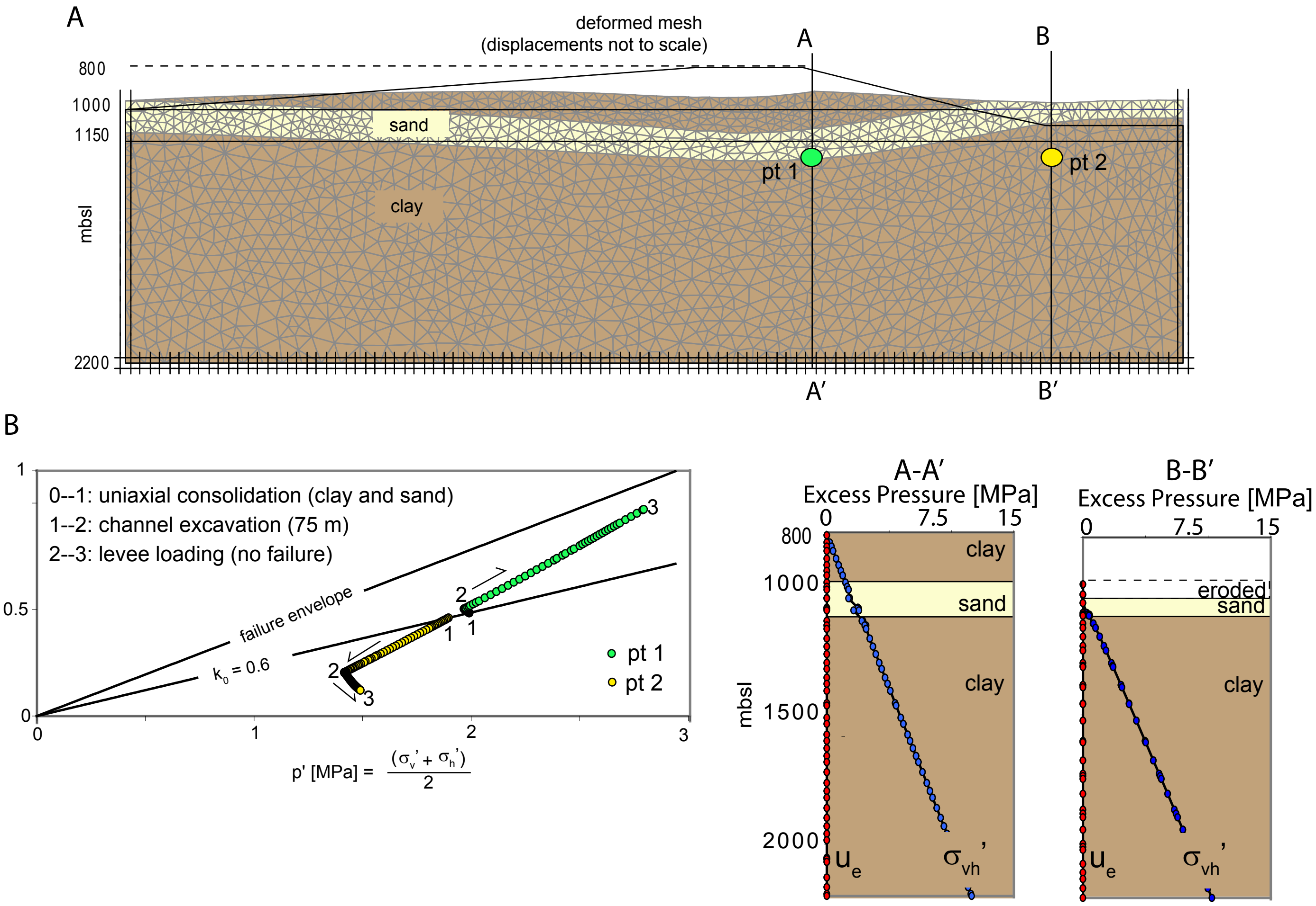

Figure 4.6 Hydrostatic example (no failure).
The channel-levee system can accommodate the excavation of the channel and the loading of the levee without triggering base failure. The deformed mesh (A) illustrates that most of the deformation is associated with vertical consolidation beneath the thick levee and some uplift into the channel from unloading. Vertical profiles A-A' and B-B' show excess pore pressure ($u_e = 0$) and hydrostatic vertical effective stress (σ_{vh}') with depth. B) Stress paths of points 1 and 2 plot the stress state with each calculation phase. Phase 1 is uniaxial consolidation of the deep clay and sand. Phase 2 is drained excavation of the channel (75 m). Phase 3 is drained loading of the clay levee, which ultimately does not produce base failure.

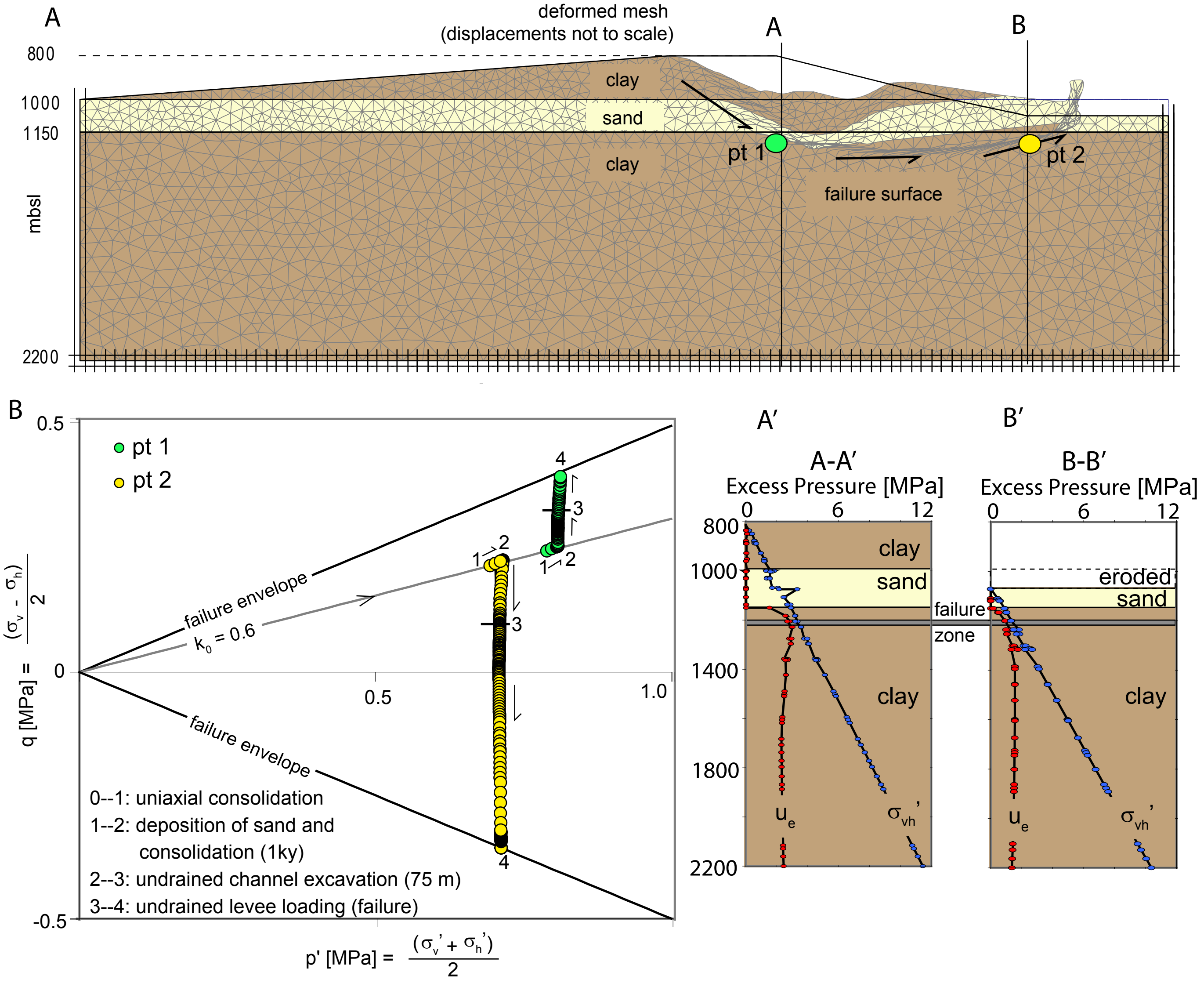

Figure 4.7. Overpressured example (base failure).
A) Deformed mesh illustrates the failure surface that developed after loading of levee, (displacements not to scale). Vertical profiles A-A′ and B-B′ show the excess pore pressure (u_e) and hydrostatic vertical effective stress (σ_{vh}') with depth. Failure occurs where effective stress is lowest (difference between u_e and σ_{vh}'). (B) Stress paths of points 1 and 2 plot the stress state with each calculation phase. Phase 1 is uniaxial consolidation. Phase 2 is instaneous deposition of sand, followed by 1ky of consolidation. Phase 3 is undrained excavation of channel. Phase 4 is undrained deposition of levee, which ultimately pushes the stress state of both points to the failure envelope.

4.9 REFERENCES

Abreu, V., Sillivan, M., Pirmez, C. and Mohrig, D., 2003. Lateral accretion packages (LAPs): and important reservoir element in deep water sinuous channels. Marine and Petroleum Geology, 20: 631-648.

Babonneau, N., Savoye, B., Cremer, M. and Klein, B., 2002. Morphology and architecture of the present canyon and channel system of the Zaire deep-sea fan. Marine and Petroleum Geology, 19(4): 445-467.

Binger, W.V., 1948. Analytical Studies of Panama Canal Slides, Proceedings of the 2nd International Conference on Soil Mechanics and Foundation Engineering, Rotterdam, the Netherlands, pp. 54-60.

Biot, M.A., 1941. General Theory of Three-Dimensional Consolidation. Journal of Applied Physics, 12(2): 155-164.

Bishop, A.W. and Bjerrum, L., 1960. The relevance of the triaxial test to the solution of stability problems, Proceedings of the ASCE Research Conference on Shear Strength of Cohesive Soils. American Society of Civil Engineers, Boulder, CO, pp. 437-501.

Bjerrum, L. and Eide, O., 1956. Stability of strutted excavations in clay. Geotechnique, 6(1): 32-47.

Bouma, A.H., Coleman, J.M. and Scientists, D.L.S., 1985. Mississippi Fan: Leg 96 Program and Principal Results. In: A.H. Bouma, W.R. Normark and N.E. Barnes (Editors), Submarine Fans and Related Turbidite Systems. Springer-Verlag, New York, pp. 247-252.

Brinkgreve, R.B.J. (Editor), 2002. PLAXIS 2D, Finite Element Code for Soil and Rock Analyses, Version 8. A.A. Balkema Publishers, Netherlands.

Brooks, G.B., 2003. Alluvial Deposits of a mud-dominated stream: The Red River, Manitoba, Canada. Sedimentology, 50: 441-458.

Damuth, J.E., Kolla, V., Flood, R.D., Kowsmann, R.O., Monteiro, M.C., Gorini, M.A., Palma, J.J.C. and Belderson, R.H., 1983a. Distributary Channel Meandering and Bifurcation Patterns on the Amazon Deep-Sea Fan as Revealed by Long-Range Side-Scan Sonar (GLORIA). Geology, 11(2): 94-98.

Damuth, J.E., Kowsmann, R.O., Flood, R.D., Belderson, R.H. and Gorini, M.A., 1983b. Age Relationships of Distributary Channels on Amazon Deep-Sea Fan - Implications for Fan Growth-Pattern. Geology, 11(8): 470-473.

Deptuck, M.E., Sylvester, Z., Pirmez, C. and O'Byrne, C., 2007. Migration-aggradation history and 3-D seismic geomorphology of submarine channels in the Pleistocene Benin-major Canyon, western Niger Delta slope. Marine and Petroleum Geology, 24(6-9): 406-433.

Droz, L., Marsset, T., Ondreas, H., Lopez, M., Savoye, B. and Spy-Anderson, F.L., 2003. Architecture of an active mud-rich turbidite system: The Zaire Fan (Congo-Angola margin southeast Atlantic): Results from ZaiAngo 1 and 2 cruises. AAPG Bulletin, 87(7): 1145-1168.

Dugan, B. and Germain, J.T., 2009. Data report: strength characteristics of sediments from IODP Expedition 308, Sites U1322 and U1324. In: P.B. Flemings, J.H. Behrmann, C.M. John and E. Scientists (Editors), Proc. IODP 308, College

Station, TX, (Integrated Ocean Drilling Program Management International, Inc.), doi:10.2204/iodp.proc.308.210.2009.

Dugan, B. and Germaine, J.T., 2008. Near-seafloor overpressure in the deepwater Mississippi Canyon, northern Gulf of Mexico. Geophys. Res. Lett., 35(L02304, 10.1029/2007GL032275).

Eaton, L.F., 1999. Drilling Through Deepwater Shallow Water Flow Zones at Ursa, SPE/IADC, Amsterdam, Holland, pp. 153-164.

Emmel, F.J. and Curray, J.R., 1985. Bengal Fan, Indian Ocean. In: A.H. Bouma, W.R. Normark and N.E. Barnes (Editors), Submarine Fans and Related Turbidite Systems. Springer-Verlag, New York, pp. 107-112.

Flemings, P.B., Long, H., Dugan, B., Germaine, J., John, C., Behrmann, J.H., Sawyer, D. and Scientists, I.E., 2008. Pore pressure penetrometers document high overpressure near the seafloor where multiple submarine landslides have occurred on the continental slope, offshore Louisiana, Gulf of Mexico. Earth and Planetary Science Letters, 269(3-4): 309-324.

Flood, R.D. and Damuth, J.E., 1987. Quantitative characteristics of sinuous distributary channels on the Amazon Deep-Sea Fan. Geological Society of America Bulletin, 98: 728-738.

Gervais, A., Mulder, T., Savoye, B., Migeon, S. and Cremer, M., 2001. Recent processes of levee formation on the Zaire deep-sea fan. Comptes Rendus De L Academie Des Sciences Serie Ii Fascicule a-Sciences De La Terre Et Des Planetes, 332(6): 371-378.

Hackbarth, C.J. and Shew, R.D., 1994. Morphology and Stratigraphy of a Mid-Pleistocene Turbidite Leveed Channel From Seismic, Core, and Log Data, Northeastern Gulf of Mexico, Submarine Fans and Turbidite Systems GCSSEPM Foundation 15th Annual Research Conference, pp. 127-133.

Heinio, P. and Davies, R.J., 2007. Knickpoint migration in submarine channels in response to fold growth, western Niger Delta. Marine and Petroleum Geology, 24(6-9): 434-449.

Kane, I.A., Kneller, B.C., Dykstra, M., Kassem, A. and McCaffrey, W.D., 2007. Anatomy of a submarine channel-levee: An example from Upper Cretaceous slope sediments, Rosario Formation, Baja California, Mexico. Marine and Petroleum Geology, 24(6-9): 540-563.

Kane, I.A., McCaffrey, W.D., Peakall, J. and Kneller, B.C., 2009. Submarine channel levee shape and sediment waves from physical experiments. Sedimentary Geology, 223(1-2): 75-85.

Labourdette, R. and Bez, M., 2010. Element migration in turbidite systems: Random or systematic depositional processes? AAPG Bulletin, 94(3): 345-368.

Laury, R.L., 1971. Stream Bank Failure and Rotational Slumping: Preservation and Significance in the Geologic Record. Geological Society of America Bulletin, 82(5): 1251-1266.

Long, H., Flemings, P.B., Germain, J.T., Saffer, D. and Dugan, B., 2008. Data Report: Consolidation Characteristics of Sediments from IODP Expedition 308, Ursa Basin, Gulf of Mexico. In: P.B. Flemings, J.H. Behrmann, C. John and E.

Scientists (Editors), Proc. IODP, 308, College Station, TX, (Integrated Ocean Drilling Program Management International, Inc.),doi:10.2204/iodp.proc.308.204.2008.

Long, H., Flemings, P.B., Germaine, J.T. and Saffer, D.M., in review. Consolidation and Pore Fluid Pressure of Ursa Sediments, Deepwater Gulf of Mexico. Earth and Planetary Science Letters.

Mahaffie, M.J., 1994. Reservoir classification for turbidite intervals at the Mars discovery, Mississippi Canyon 807, Gulf of Mexico. In: P. Weimer, A.H. Bouma and B.G. Perkins (Editors), Submarine fans and turbidite systems: Gulf Coast Section SEPM Foundation 15th Annual Research Conference, pp. 233-244.

Mayall, M., Jones, E. and Casey, M., 2006. Turbidite channel reservoirs--Key elements in facies prediction and effective development. Marine and Petroleum Geology, 23(8): 821-841.

McHargue, T.R. and Webb, J.E., 1986. Internal Geometry, Seismic Facies, and Petroleum Potential of Canyons and Inner Fan Channels of the Indus Submarines Fan. American Association of Petroleum Geologists, 70(2): 161-180.

Migeon, S., Savoye, B., Babonneau, N. and Andersson, F.L.S., 2004. Processes of Sediment-Wave Construction Along the Present Zaire Deep-Sea Meandering Channel: Role of Meanders and Flow Stripping. Journal of Sedimentary Research, 74(4): 580-598.

Morris, W. and Busby-Spera, C., 1990. A submarine-fan valley-levee complex in the Upper Cretaceous Rosario Formation: Implication for turbidite facies models. Geological Society of America Bulletin, 102(7): 900-914.

Normark, W.R., 1970. Growth patterns of deep-sea fans, American Association of Petroleum Geologists Bulletin. American Association of Petroleum Geologists : Tulsa, OK, United States, United States, pp. 2170-2195.

Ostermeier, R.M., Pelletier, J.H., Winker, C.D., Nicholson, J.W., Rambow, F.H. and Cowan, C.K., 2000. Dealing with Shallow-Water Flow in the Deepwater Gulf of Mexico, Offshore Technology Conference, Houston, TX, pp. 75-86.

Peakall, J., McCaffrey, B. and Kneller, B., 2000. A process Model for the Evolution, Morphology, and Architecture of Sinuous Submarine Channels. Journal of Sedimentary Research, 70(3): 434-448.

Pelletier, J.H., Ostermeier, R.M., Winker, C.D., Nicholson, J.W. and Rambow, F.H., 1999. Shallow Water Flow Sands in the Deepwater Gulf of Mexico: Some Recent Shell Experience, 1999 International Forum on Shallow Water Flows Conference Proceedings, League City, TX.

Pirmez, C., 1994. Growth of a Submarine Meandering Channel-Levee System on the Amazon Fan, Columbia University, New York, 587 pp.

Pirmez, C., Isram, J., 2003. Reconstruction of turbidity currents in Amazon Channel. Marine and Petroleum Geology, 20: 823-849.

Posamentier, H.W., 2003. Depositional elements associated with a basin floor channel-levee system: case study from the Gulf of Mexico. Marine and Petroleum Geology, 20: 677-690.

Prins, M.A. and Postma, G., 2000. Effects of climate, sea level, and tectonics unraveled for last deglaciation turbidite records of the Arabian Sea. Geology, 28(4): 375-378.

Sawyer, D.E., Flemings, P.B., Dugan, B. and Germaine, J.T., 2009. Retrogressive failures recorded in mass transport deposits in the Ursa Basin, Northern Gulf of Mexico. J. Geophys. Res., 114.

Shengqiang, Y., Shiguo, W., Thomas, L., Genshun, Y., Fuliang, L., Feng, C., Hairong, W. and Li, L., 2009. Fine-grained Pleistocene deepwater turbidite channel system on the slope of Qiongdongnan Basin, northern South China Sea. Marine and Petroleum Geology, 26(8): 1441-1451.

Steffens, G.S., Shipp, R.C., Prather, B.E., Nott, J.A., Gibson, J.L. and Winker, C.D., 2004. The Use of Near-Seafloor 3D Seismic Data in Deepwater Exploration and Production. Geological Society, London, Memoirs, 29(1): 35-43.

Stigall, J. and Dugan, B., 2010. Overpressure and earthquake initiated slope failure in the Ursa region, northern Gulf of Mexico. J. Geophys. Res., 115(B4): B04101.

Straub, K.M. and Mohrig, D., 2008. Quantifying the morphology and growth of levees in aggrading submarine channels. J. Geophys. Res., 113.

Terzaghi, K. and Peck, R.B., 1948. Soil Mechanics in Engineering Practice. John Wiley & Sons, Inc., 566 pp.

Urgeles, R., Locat, J., Sawyer, D.E., Flemings, P.B., Dugan, B. and Binh, N.T.T., 2009. History of Pore Pressure Build Up and Slope Instability in Mud-Dominated Sediments of Ursa Basin, Gulf of Mexico Continental Slope. In: D.C. Mosher et al. (Editors), Submarine Mass Movements and Their Consequences. Advances in Natural and Technological Hazards Research. Springer, Dordrecht, pp. 179-190.

Weber, M.E., Wiedicke, M.H., Kudrass, H.R., Hubscher, C. and Erlenkeuser, H., 1997. Active growth of the Bengal Fan during sea-level rise and highstand. Geology, 25(4): 315-318.

Weimer, P. and Buffler, R.T., 1988. Distribution and seismic facies of Mississippi fan channels. Geology, 16: 900-903.

Williams, H. and Flint, S., 1990. Anatomy of a channel-bank collapse structure in Tertiary fluvio-lacustrine sediments of the Lower Rhine Basin, Germany. Geological Magazine, 127(5): 445-451.

Winker, C.D. and Booth, J.R., 2000. Sedimentary Dynamics of the Salt-Dominated Continental Slope, Gulf of Mexico: Integration of Observations from the Seafloor, Near-Surface, and Deep Subsurface, GCSSEPM Foundation 20th Annual Research Conference, pp. 1059-1086.

Winker, C.D. and Shipp, R.C., 2002. Sequence Stratigraphic Framework for Prediction of Shallow Water Flow in the Greater Mars-Ursa Area, Mississippi Canyon Area, Gulf of Mexico Continental Slope, 22nd Annual GCSSEPM Foundation Bob F. Perkins Research Conference, abs., pp. 1.

Zühlsdorff, C., Wien, K., Stuut, J.B.W. and Henrich, R., 2007. Late Quaternary sedimentation within a submarine channel-levee system offshore Cap Timiris, Mauritania. Marine Geology, 240(1-4): 217-234.

References

Abreu, V., Sillivan, M., Pirmez, C. and Mohrig, D., 2003. Lateral accretion packages (LAPs): and important reservoir element in deep water sinuous channels. Marine and Petroleum Geology, 20: 631-648.

Aksu, A., 1984. Subaqueous debris flow deposits in Baffin Bay. Geo-Marine Letters, 4(2): 83.

Ancey, C. and Cochard, S., 2009. The dam-break problem for Herschel-Bulkley viscoplastic fluids down steep flumes. Journal of Non-Newtonian Fluid Mechanics, 158(1-3): 18-35.

ASTM, 2007. Standard D422, Standard Test Method for Particle-Size Analysis of Soils, West Conshohocken, PA.

Babonneau, N., Savoye, B., Cremer, M. and Klein, B., 2002. Morphology and architecture of the present canyon and channel system of the Zaire deep-sea fan. Marine and Petroleum Geology, 19(4): 445-467.

Bardet, J.P., Synolakis, C.E., Davies, H.L., Imamura, F. and Okal, E.A., 2003. Landslide tsunamis: Recent findings and research directions. Pure and Applied Geophysics, 160(10-11): 1793-1809.

Binger, W.V., 1948. Analytical Studies of Panama Canal Slides, Proceedings of the 2nd International Conference on Soil Mechanics and Foundation Engineering, Rotterdam, the Netherlands, pp. 54-60.

Biot, M.A., 1941. General Theory of Three-Dimensional Consolidation. Journal of Applied Physics, 12(2): 155-164.

Bishop, A.W., 1973. The stability of tips and spoil heaps, Quarterly Journal of Engineering Geology. Scottish Academic Press; Geological Society of London : Edinburgh, United Kingdom, United Kingdom, pp. 335-376.

Bishop, A.W. and Bjerrum, L., 1960. The relevance of the triaxial test to the solution of stability problems, Proceedings of the ASCE Research Conference on Shear Strength of Cohesive Soils. American Society of Civil Engineers, Boulder, CO, pp. 437-501.

Bjerrum, L. and Eide, O., 1956. Stability of strutted excavations in clay. Geotechnique, 6(1): 32-47.

Bondevik, S., Løvholt, F., Harbitz, C., Mangerud, J., Dawson, A. and Inge Svendsen, J., 2005. The Storegga Slide tsunami--comparing field observations with numerical simulations. Marine and Petroleum Geology, 22(1-2): 195-208.

Booth, J.S., O'Leary, D.W., Popenoe, P. and Danforth, W.W., 1993. U.S. Atlantic Continental Slope Landslides: Their Distribution, General Attributes, and Implications. U.S. Geological Survey Bulletin, 2002: 14-22.

Bouma, A.H., Coleman, J.M. and Scientists, D.L.S., 1985. Mississippi Fan: Leg 96 Program and Principal Results. In: A.H. Bouma, W.R. Normark and N.E. Barnes (Editors), Submarine Fans and Related Turbidite Systems. Springer-Verlag, New York, pp. 247-252.

Brand, J.R., Lanier, D.L., Berger III, W.J., Kasch, V.R. and Young, A.G., 2003. Relationship Between Near Seafloor Seismic Amplitude, Impedance, and Soil Shear Strength Properties and Use in Prediction of Shallow Seated Slope Failure, Offshore Technology Conference, pp. 1-8.

Brinkgreve, R.B.J. (Editor), 2002. PLAXIS 2D, Finite Element Code for Soil and Rock Analyses, Version 8. A.A. Balkema Publishers, Netherlands.

Brodsky, E.E., Gordeev, E. and Kanamori, H., 2003. Landslide basal friction as measured by seismic waves. Geophysical Research Letters, 30(24, doi: 10.1029/2003GL018).

Brooks, G.B., 2003. Alluvial Deposits of a mud-dominated stream: The Red River, Manitoba, Canada. Sedimentology, 50: 441-458.

Bryn, P., Berg, K., Forsberg, C.F., Solheim, A. and Kvalstad, T.J., 2005. Explaining the Storegga Slide. Marine and Petroleum Geology, 22(1-2): 11-19.

Bunz, S., Mienert, J., Bryn, P. and Berg, K., 2005. Fluid flow impact on slope failure from 3D seismic data: a case study in the Storegga Slide. Basin Research, 17(1): 109-122.

Burland, J.B., 1990. On the Compressibility and Shear Strength of Natural Clays. Geotechnique, 40(3): 329-378.

Butenko, J. and Barbot, J.P., 1980. Geologic Hazards Related To Offshore Drilling And Construction In The Orinoco River Delta Of Venezuela. Journal Of Petroleum Technology, 32(5): 764-770.

Chandler, R.J., 2000. Clay sediments in depositional basins: The geotechnical cycle. Quarterly Journal of Engineering Geology and Hydrogeology, 33: 7-39.

Cochard, S. and Ancey, C., 2009. Experimental investigation of the spreading of viscoplastic fluids on inclined planes. Journal of Non-Newtonian Fluid Mechanics, 158(1-3): 73-84.

Coleman, J.M. and Prior, D.B., 1988. Mass-Wasting On Continental Margins. Annual Review Of Earth And Planetary Sciences, 16: 101-119.

Coleman, J.M. and Roberts, H.H., 1988. Late Quaternary Depositional Framework of the Louisiana Continental Shelf and Upper Continental Slope, Transactions GCAGS, pp. 407-419.

Corthay II, J.E. and Aliyev, A.A., 2000. Delineation of a Mud Volcano Complex, Surficial Mudflows, Slump Blocks, and Shallow Gas Reservoirs, Offshore Azerbaijan, Offshore Technology Conference, Houston, TX, pp. 1-11.

Coussot, P., Laigle, D., Arattano, M., Deganutti, A. and Marchi, L., 1998. Direct determination of rheological characteristics of debris flow. Journal Of Hydraulic Engineering-Asce, 124(8): 865-868.

Coussot, P. and Proust, S., 1996. Slow, unconfined spreading of a mudflow. J. Geophys. Res., 101(B11)(25): 25,217–25,229.

Coussot, P., Proust, S. and Ancey, C., 1996. Rheological interpretation of deposits of yield stress fluids. Journal of Non-Newtonian Fluid Mechanics, 66(1): 55-70.

Craig, R.F., 1992. Soil Mechanics. Chapman & Hall, London, 427 pp.

Damuth, J.E., Kolla, V., Flood, R.D., Kowsmann, R.O., Monteiro, M.C., Gorini, M.A., Palma, J.J.C. and Belderson, R.H., 1983a. Distributary Channel Meandering and Bifurcation Patterns on the Amazon Deep-Sea Fan as Revealed by Long-Range Side-Scan Sonar (GLORIA). Geology, 11(2): 94-98.

Damuth, J.E., Kowsmann, R.O., Flood, R.D., Belderson, R.H. and Gorini, M.A., 1983b. Age Relationships of Distributary Channels on Amazon Deep-Sea Fan - Implications for Fan Growth-Pattern. Geology, 11(8): 470-473.

Dan, G., Sultan, N. and Savoye, B., 2007. The 1979 Nice harbour catastrophe revisited: Trigger mechanism inferred from geotechnical measurements and numerical modelling. Marine Geology, 245(1-4): 40-64, doi: 10.1016/j.margeo.2007.06.011

De Blasio, F.V., Elverhoi, A., Issler, D., Harbitz, C.B., Bryn, P. and Lien, R., 2005. On the dynamics of subaqueous clay rich gravity mass flows - the giant Storegga slide, Norway. Marine And Petroleum Geology, 22(1-2): 179-186.

De Blasio, R., Elverhoi, A., Issler, D., Harbitz, C.B., Bryn, P. and Lien, R., 2004. Flow models of natural debris flows originating from overconsolidated clay materials. Marine Geology, 213(1-4): 439-455.

Deptuck, M.E., Sylvester, Z., Pirmez, C. and O'Byrne, C., 2007. Migration-aggradation history and 3-D seismic geomorphology of submarine channels in the Pleistocene Benin-major Canyon, western Niger Delta slope. Marine and Petroleum Geology, 24(6-9): 406-433.

Droz, L., Marsset, T., Ondreas, H., Lopez, M., Savoye, B. and Spy-Anderson, F.L., 2003. Architecture of an active mud-rich turbidite system: The Zaire Fan (Congo-Angola margin southeast Atlantic): Results from ZaiAngo 1 and 2 cruises. AAPG Bulletin, 87(7): 1145-1168.

Dugan, B. and Flemings, P.B., 2000. Overpressure and Fluid Flow in the New Jersey Continental Slope: Implications for Slope Failure and Cold Seeps. Science, 289: 288-291.

Dugan, B., Flemings, P.B., Urgeles, R., Sawyer, D.E., Iturrino, G.J., Moore, J.C. and Schneider, J., 2007a. Physical properties of mass transport complexes in the Ursa Region, northern Gulf of Mexico (IODP Expedition 308) determined from log, core, and seismic data, OTC 18704, Offshore Technology Conference, Houston, TX, pp. 1-13.

Dugan, B., Flemings, P.B., Urgeles, R., Sawyer, D.E., Iturrino, G.J., Moore, J.C. and Schneider, J., 2007b. Physical Properties of Stacked Slumps in the Ursa Region, Northern Gulf of Mexico (IODP Expedition 308) Determined from Log, Core, and Seismic Data, Paper #18704, Proceedings of the Offshore Technology Conference, Houston, TX.

Dugan, B. and Germain, J.T., 2009. Data report: strength characteristics of sediments from IODP Expedition 308, Sites U1322 and U1324. In: P.B. Flemings, J.H. Behrmann, C.M. John and E. Scientists (Editors), Proc. IODP 308, College Station, TX, (Integrated Ocean Drilling Program Management International, Inc.), doi:10.2204/iodp.proc.308.210.2009.

Dugan, B. and Germaine, J.T., 2008. Near-seafloor overpressure in the deepwater Mississippi Canyon, northern Gulf of Mexico. Geophys. Res. Lett., 35(L02304, 10.1029/2007GL032275).

Dugan, B. and Germaine, J.T., 2009. Data Report: Strength Characteristics of Sediments from IODP Expedition 308, Sites U1322 and U1324. In: P.B. Flemings, J.H. Behrmann, C.M. John and a.t.E. Scientists (Editors), Proc. IODP, 308. Integrated Ocean Drilling Program Management International, Inc., College Station, TX, doi:10.2204/iodp.proc.308.210.2009.

Eaton, L.F., 1999. Drilling Through Deepwater Shallow Water Flow Zones at Ursa, SPE/IADC, Amsterdam, Holland, pp. 153-164.

Einsele, G., 1974. Mass physical properties, sliding and erodibility of experimentally deposited and differently consolidated clayey muds (approach, equipment, and first results). In: R. Overbeck, H.U. Schwarz and G. Unsoeld (Editors), Sedimentology. Blackwell : Oxford-Boston, International, International, pp. 339-372.

Einsele, G., 1990. Deep-reaching liquefaction potential of marine slope sediments as a prerequisite for gravity mass flows? (Results from the DSDP). Marine Geology, 91: 267-279.

Elverhoi, A., De Blasio, F.V., Butt, F.A., Issler, D., Harbitz, C., Engvik, L., Solheim, A. and Marr, J., 2002. Submarine mass-wasting on glacially-influenced continental slopes: processes and dynamics. In: J.A. Dowdeswell and C.O. Cofaigh (Editors), Glacier-influenced sedimentation on high-latitude continental margins, Geological Society of London Special Publication no. 203. The Geological Society of London, London, pp. 73-87.

Elverhoi, A., Norem, H., Andersen, E.S., Dowdeswell, J.A., Fossen, I., Haflidason, H., Kenyon, N.H., Laberg, J.S., King, E.L., Sejrup, H.P., Solheim, A. and Vorren, T., 1997. On the origin and flow behavior of submarine slides on deep-sea fans along the Norwegian Barents Sea continental margin. Geo-Marine Letters, 17(2): 119-125.

Embley, R.W., 1976. New Evidence For Occurrence Of Debris Flow Deposits In Deep-Sea. Geology, 4(6): 371-374.

Emmel, F.J. and Curray, J.R., 1985. Bengal Fan, Indian Ocean. In: A.H. Bouma, W.R. Normark and N.E. Barnes (Editors), Submarine Fans and Related Turbidite Systems. Springer-Verlag, New York, pp. 107-112.

Flemings, P.B., Behrmann, J.H., John, C.M. and Scientists, E. (Editors), 2006. Gulf of Mexico Hydrogeology. Proceedings of the Integrated Ocean Drilling Program, 308. Integrated Ocean Drilling Program Management International, Inc., College Station TX.

Flemings, P.B., Long, H., Dugan, B., Germaine, J., John, C., Behrmann, J.H., Sawyer, D. and Scientists, I.E., 2008. Pore pressure penetrometers document high overpressure near the seafloor where multiple submarine landslides have occurred on the continental slope, offshore Louisiana, Gulf of Mexico. Earth and Planetary Science Letters, 269(3-4): 309-324.

Flood, R.D. and Damuth, J.E., 1987. Quantitative characteristics of sinuous distributary channels on the Amazon Deep-Sea Fan. Geological Society of America Bulletin, 98: 728-738.

Fryer, G.J., Watts, P. and Pratson, L.F., 2004. Source of the great tsunami of 1 April 1946: a landslide in the upper Aleutian forearc. Marine Geology, 203(3-4): 201-218.

Garziglia, S., Migeon, S., Ducassou, E., Loncke, L. and Mascle, J., 2008. Mass-transport deposits on the Rosetta province (NW Nile deep-sea turbidite system, Egyptian margin): Characteristics, distribution, and potential causal processes. Marine Geology, 250(3-4): 180-198, doi: 10.1016/j.margeo.2008.01.016.

Gauer, P., Kvalstad, T.J., Forsberg, C.F., Bryn, P. and Berg, K., 2005. The last phase of the Storegga Slide: simulation of retrogressive slide dynamics and comparison with slide-scar morphology. Marine and Petroleum Geology, 22(1-2): 171-178, doi: 10.1016/j.marpetgeo.2004.10.004

Gee, M.J.R., Gawthorpe, R.L. and Friedmann, S.J., 2006. Triggering and evolution of a giant submarine landslide, offshore Angola, revealed by 3D seismic stratigraphy and geomorphology. Journal Of Sedimentary Research, 76(1-2): 9-19, doi: 10.2110/jsr.2006.02

Gee, M.J.R., Masson, D.G., Watts, A.B. and Allen, P.A., 1999. The Saharan debris flow: an insight into the mechanics of long runout submarine debris flows. Sedimentology, 46(2): 317-335.

Gervais, A., Mulder, T., Savoye, B., Migeon, S. and Cremer, M., 2001. Recent processes of levee formation on the Zaire deep-sea fan. Comptes Rendus De L Academie Des Sciences Serie Ii Fascicule a-Sciences De La Terre Et Des Planetes, 332(6): 371-378.

Graham, J., 1984. Methods of Stability Analysis. In: D. Brundsen and D.B. Prior (Editors), Slope Instability. Landscape Systems: A Series in Geomorphology. John Wiley & Sons Ltd., pp. 171-215.

Hackbarth, C.J. and Shew, R.D., 1994. Morphology and Stratigraphy of a Mid-Pleistocene Turbidite Leveed Channel From Seismic, Core, and Log Data, Northeastern Gulf of Mexico, Submarine Fans and Turbidite Systems GCSSEPM Foundation 15th Annual Research Conference, pp. 127-133.

Hampton, M.A., 1972. The role of subaqueous debris flow in generating turbidity currents. Journal of Sedimentary Research, 42(4): 775-793.

Hampton, M.A., 1996. Submarine Landslides. Reviews of Geophysics, 34(1): 33-59.

Heinio, P. and Davies, R.J., 2007. Knickpoint migration in submarine channels in response to fold growth, western Niger Delta. Marine and Petroleum Geology, 24(6-9): 434-449.

Henrich, R., Hanebuth, T.J.J., Krastel, S., Neubert, N. and Wynn, R.B., 2008. Architecture and sediment dynamics of the Mauritania Slide Complex. Marine and Petroleum Geology, 25(1): 17-33.

Homza, T.X., 2004. A Structural Interpretation of the Fish Creek Slide (Lower Cretaceous), northern Alaska. AAPG Bulletin, 88(3): 265-278.

Hornbach, M.J., Braudy, N., Briggs, R.W., Cormier, M.-H., Davis, M.B., Diebold, J.B., Dieudonne, N., Douilly, R., Frohlich, C., Gulick, S.P.S., Johnson Iii, H.E., Mann, P., McHugh, C., Ryan-Mishkin, K., Prentice, C.S., Seeber, L., Sorlien, C.C., Steckler, M.S., Symithe, S.J., Taylor, F.W. and Templeton, J., High tsunami frequency as a result of combined strike-slip faulting and coastal landslides. Nature Geosci, 3(11): 783-788.

Huang, X. and García, M.H., 1999. Modeling of non-hydroplaning mudflows on continental slopes. Marine Geology, 154(1-4): 131-142.

Ilstad, T., Elverhoi, A., Issler, D. and Marr, J.G., 2004a. Subaqueous debris flow behaviour and its dependence on the sand/clay ratio: a laboratory study using particle tracking. Marine Geology, 213(1-4): 415-438, doi: 10.1016/j.margeo.2004.10.017

Ilstad, T., Marr, J.G., Elverhoi, A. and Harbitz, C.B., 2004b. Laboratory studies of subaqueous debris flows by measurements of pore-fluid pressure and total stress. Marine Geology, 213(1-4): 403-414, doi: 10.1016/j.margeo.2004.10.016

Imran, J., Harff, P. and Parker, G., 2001. A numerical model of submarine debris flow with graphical user interface. Computers & Geosciences, 27(6): 717-729.

Iverson, R.M., 1997. The Physics of Debris Flows. Reviews of Geophysics, 35(3): 245-296.

Iverson, R.M., 2005. Regulation of landslide motion by dilatancy and pore pressure feedback. Journal of Geophysical Research, 110(F02015, doi:10.1029/2004JF000268).

Iverson, R.M., Reid, M.E. and LaHusen, R.G., 1997. Debris-flow mobilization from landslides. Annual Review of Earth and Planetary Sciences, 25: 85-138.

Jansen, E., Befring, S., Bugge, T., Eidvin, T., Holtedahl, H. and Sejrup, H.P., 1987. Large Submarine Slides on the Norwegian Continental-Margin - Sediments, Transport and Timing. Marine Geology, 78(1-2): 77-107.

Jeanjean, P., Hill, A. and Thomson, J., 2003. The Case for Confidently Siting Facilities along the Sigsbee Escarpment in the Southern Green Canyon Area of the Gulf of Mexico: Summary and Conclusions from Integrated Studies, Offshore Technology Conference.

Jenner, K.A., Piper, D.J.W., Campbell, D.C. and Mosher, D.C., 2007. Lithofacies and origin of late Quaternary mass transport deposits in submarine canyons, central Scotian Slope, Canada. Sedimentology, 54(1): 19-38, doi: 10.1111/j.1365-3091.2006.00819.x

Johnson, A.M., 1970. Physical Processes in Geology. Freeman Cooper, San Francisco, CA.

Kane, I.A., Kneller, B.C., Dykstra, M., Kassem, A. and McCaffrey, W.D., 2007. Anatomy of a submarine channel-levee: An example from Upper Cretaceous slope sediments, Rosario Formation, Baja California, Mexico. Marine and Petroleum Geology, 24(6-9): 540-563.

Kane, I.A., McCaffrey, W.D., Peakall, J. and Kneller, B.C., 2009. Submarine channel levee shape and sediment waves from physical experiments. Sedimentary Geology, 223(1-2): 75-85.

Kayen, R.E., Schwab, W.C., Lee, H.J., Torresan, M.E., Hein, J.R., Quinterno, P.J. and Levin, L.A., 1989. Morphology Of Sea-Floor Landslides On Horizon Guyot - Application Of Steady-State Geotechnical Analysis. Deep-Sea Research Part A-Oceanographic Research Papers, 36(12): 1817-1839.

Keller, G.H., Lambert, D.N. and Bennett, R.H., 1979. Geotechnical properties of continental slope deposits; Cape Hatteras to Hydrographer Canyon, Special Publication - Society of Economic Paleontologists and Mineralogists. SEPM (Society for Sedimentary Geology) : Tulsa, OK, United States, United States, pp. 131-151.

Kennett, J.P. and Huddlestun, P., 1972. Late Pleistocene paleoclimatology, foraminiferal biostratigraphy and tephrochronology, western Gulf of Mexico. Quaternary Research, 2(1): 38-69.

Kvalstad, T.J., Andresen, L., Forsberg, C.F., Berg, K., Bryn, P. and Wangen, M., 2005. The Storegga slide: evaluation of triggering sources and slide mechanics. Marine and Petroleum Geology, 22(1-2): 245-256, doi: 10.1016/j.marpetgeo.2004.10.019

L'Hereux, J.S., Leroueil, S. and Laflamme, J.F., in press. Evolution of the Factor of Safety Following Excavation in Clay. Canadian Geotechnical Journal.

Laberg, J.S. and Vorren, T.O., 2000. Flow behaviour of the submarine glacigenic debris flows on the Bear Island Trough Mouth Fan, western Barents Sea. Sedimentology, 47(6): 1105-1117.

Labourdette, R. and Bez, M., 2010. Element migration in turbidite systems: Random or systematic depositional processes? AAPG Bulletin, 94(3): 345-368.

Lambe, T.W. and Whitman, R.V., 1969. Soil Mechanics. Series in Soil Engineering. John Wiley & Sons, New York, 553 pp.

Laury, R.L., 1971. Stream Bank Failure and Rotational Slumping: Preservation and Significance in the Geologic Record. Geological Society of America Bulletin, 82(5): 1251-1266.

Lee, H. and Baraza, J., 1999. Geotechnical characteristics and slope stability in the Gulf of Cadiz. Marine Geology, 155(1-2): 173-190.

Leroueil, S., 2001. Natural Slopes and Cuts: Movement and Failure Mechanisms. Geotechnique, 51(No. 3): 197-243, doi: 10.1680/geot.51.3.197.39365.

Li, Q., Xiang, R. and Zheng, F., 2007. Data report: planktonic and benthic foraminifers from IODP Hole U1322B. In: P.B. Flemings, Behrmann, J.H., John, C.M., and the Expedition 308 Scientists (Editor), Proc. IODP, 308. Integrated Ocean Drilling Program Management International, Inc., College Station, TX, doi:10.2204/iodp.proc.308.202.2007, pp. 1-8.

Locat, J., 1997. Normalized rheological behaviour of fine muds and their flow properties in a pseudoplastic regime. Debris-Flow Hazards Mitigation: Mechanics, Prediction & Assessment. Amer Soc Civil Engineers, New York, 260-269 pp.

Locat, J. and Demers, D., 1988. Viscosity, Yield Stress, Remolded Strength, And Liquidity Index Relationships For Sensitive Clays. Canadian Geotechnical Journal, 25(4): 799-806.

Long, H., Flemings, P.B., Germain, J.T., Saffer, D. and Dugan, B., 2008. Data Report: Consolidation Characteristics of Sediments from IODP Expedition 308, Ursa Basin, Gulf of Mexico. In: P.B. Flemings, J.H. Behrmann, C. John and E. Scientists (Editors), Proc. IODP, 308, College Station, TX, (Integrated Ocean Drilling Program Management International, Inc.),doi:10.2204/iodp.proc.308.204.2008.

Long, H., Flemings, P.B., Germaine, J.T. and Saffer, D.M., in review. Consolidation and Pore Fluid Pressure of Ursa Sediments, Deepwater Gulf of Mexico. Earth and Planetary Science Letters.

Løvholt, F., Harbitz, C.B. and Haugen, K.B., 2005. A parametric study of tsunamis generated by submarine slides in the Ormen Lange/Storegga area off western Norway. Marine and Petroleum Geology, 22(1-2): 219-231.

Lucente, C.C. and Pini, G.A., 2003. Anatomy and emplacement mechanism of a large submarine slide within a Miocene foredeep in the northern Apennines, Italy: A field perspective. American Journal Of Science, 303(7): 565-602.

Lucente, C.C. and Pini, G.A., 2008. Basin-wide mass-wasting complexes as markers of the Oligo-Miocene foredeep-accretionary wedge evolution in the Northern Apennines, Italy. Basin Research, 20(1): 49-71, doi:10.1111/j.1365-2117.2007.00344.x.

Mahaffie, M.J., 1994. Reservoir classification for turbidite intervals at the Mars discovery, Mississippi Canyon 807, Gulf of Mexico. In: P. Weimer, A.H. Bouma and B.G. Perkins (Editors), Submarine fans and turbidite systems: Gulf Coast Section SEPM Foundation 15th Annual Research Conference, pp. 233-244.

Major, J.J., 1996. Experimental studies of deposition by debris flows: Process, characteristics of deposits, and effects of pore-fluid pressure. Ph.D. Thesis, University of Washington, United States -- Washington.

Major, J.J., 2000. Gravity-driven consolidation of granular slurries - Implications for debris-flow deposition and deposit characteristics. Journal Of Sedimentary Research, 70(1): 64-83.

Major, J.J. and Iverson, R.M., 1999. Debris-flow deposition: Effects of pore-fluid pressure and friction concentrated at flow margins. GSA Bulletin, 111(10): 1424-1434.

Major, J.J. and Pierson, T.C., 1992. Debris Flow Rheology: Experimental Analysis of Fine-Grained Slurries. Water Resour. Res., 28(3): 841-857.

Marr, J.G., Harff, P.A., Shanmugam, G. and Parker, G., 2001. Experiments on subaqueous sandy gravity flows: The role of clay and water content in flow dynamics and depositional structures. Geological Society of America Bulletin, 113(11): 1377-1386.

Martinez, J.F., Cartwright, J. and Hull, B., 2005. 3D seismic interpretation of slump complexes: examples from the continental margin of Israel. Basin Research, 17(1): 83-108, doi: 10.1111/j.1365-2117.2005.00255.x.

Martinez, J.F., Cartwright, J. and James, D., 2006. Frontally confined versus frontally emergent submarine landslides: A 3D seismic characterisation. Marine and Petroleum Geology, 23(5): 585-604.

Martinsen, O.J. and Bakken, B., 1990. Extensional and compressional zones in slumps and slides in the Namurian of County Clare, Ireland. Journal of the Geological Society, 147(1): 153-164.

Masson, D.G., Canals, M., Alonso, B., Urgeles, R. and Huhnerbach, V., 1998. The Canary Debris Flow: source area morphology and failure mechanisms. Sedimentology, 45(2): 411-432.

Masson, D.G., Harbitz, C.B., Wynn, R.B., Pedersen, G. and Lovholt, F., 2006. Submarine landslides: processes, triggers and hazard prediction. Philosophical Transactions of the Royal Society -Mathematical Physical and Engineering Sciences, 364(1845): 2009-2039.

Masson, D.G., vanNiel, B. and Weaver, P.P.E., 1997. Flow processes and sediment deformation in the Canary debris flow on the NW African continental rise. Sedimentary Geology, 110(3-4): 163-179.

Masson, D.G., Watts, A.B., Gee, M.J.R., Urgeles, R., Mitchell, N.C., Le Bas, T.P. and Canals, M., 2002. Slope failures on the flanks of the western Canary Islands. Earth-Science Reviews, 57(1-2): 1-35.

Mayall, M., Jones, E. and Casey, M., 2006. Turbidite channel reservoirs--Key elements in facies prediction and effective development. Marine and Petroleum Geology, 23(8): 821-841.

McAdoo, B.G., Pratson, L.F. and Orange, D.L., 2000. Submarine landslide geomorphology, US continental slope. Marine Geology, 169: 103-136.

McArdell, B.W., Bartelt, P. and Kowalski, J., 2007. Field observations of basal forces and fluid pore pressure in a debris flow. Geophysical Research Letters, 34(L07406, doi:10.1029/2006GL029183): 1-4.

McFarlan, E. and LeRoy, D.O., 1988. Subsurface geology of the Late Tertiary and Quaternary deposits, coastal Louisiana, and the adjacent continental shelf, Gulf Coast Association of the Geological Societies Transactions, pp. 421-433.

McHargue, T.R. and Webb, J.E., 1986. Internal Geometry, Seismic Facies, and Petroleum Potential of Canyons and Inner Fan Channels of the Indus Submarines Fan. American Association of Petroleum Geologists, 70(2): 161-180.

McMurtry, G.M., Watts, P., Fryer, G.J., Smith, J.R. and Imamura, F., 2004. Giant landslides, mega-tsunamis, and paleo-sea level in the Hawaiian Islands. Marine Geology, 203(3-4): 219-233.

Migeon, S., Savoye, B., Babonneau, N. and Andersson, F.L.S., 2004. Processes of Sediment-Wave Construction Along the Present Zaire Deep-Sea Meandering Channel: Role of Meanders and Flow Stripping. Journal of Sedimentary Research, 74(4): 580-598.

Minisini, D., Trincardi, F., Asioli, A., Canu, M. and Foglini, F., 2007. Morphologic variability of exposed mass-transport deposits on the eastern slope of Gela Basin (Sicily channel). Basin Research, 19(2): 217-240, doi: 10.1111/j.1365-2117.2007.00324.x.

Mitchell, J.K., 1993. Fundamentals of Soil Behavior. John Wiley & Sons, Inc., New York, NY, 437 pp.

Mohrig, D., Elverhoi, A. and Parker, G., 1999. Experiments on the relative mobility of muddy subaqueous and subaerial debris flows, and their capacity to remobilize antecedent deposits. Marine Geology, 154(1-4): 117-129.

Mohrig, D., Whipple, K.X., Hondzo, M., Ellis, C. and Parker, G., 1998. Hydroplaning of subaqueous debris flows. Geological Society Of America Bulletin, 110(3): 387-394.

Moore, J.G., Clague, D.A., Holcomb, R.T., Lipman, P.W., Normark, W.R. and Torresan, M.E., 1989. Prodigious Submarine Landslides on the Hawaiian Ridge. Journal of Geophysical Research-Solid Earth and Planets, 94(B12): 17465-17484.

Morgenstern, N.R., 1967. Submarine Slumping and the Initiation of Turbidity Currents. Geotechnique: 189-220.

Morris, W. and Busby-Spera, C., 1990. A submarine-fan valley-levee complex in the Upper Cretaceous Rosario Formation: Implication for turbidite facies models. Geological Society of America Bulletin, 102(7): 900-914.

Moscardelli, L. and Wood, L., 2008. New classification system for mass transport complexes in offshore Trinidad. Basin Research, 20(1): 73-98.

Moscardelli, L., Wood, L. and Mann, P., 2006. Mass-transport complexes and associated processes in the offshore area of Trinidad and Venezuela. AAPG Bulletin, 90(7): 1059-1088, doi: 10.1306/02210605052.

Mosher, D.C., Piper, D.J.W., Campbell, D.C. and Jenner, K.A., 2004. Near-surface geology and sediment-failure geohazards of the central Scotian Slope. AAPG Bulletin, 88(6): 703-723.

Mulder, T. and Alexander, J., 2001. The physical character of subaqueous sedimentary density flows and their deposits. Sedimentology, 48: 269-299.

Mulder, T., Berry, J.A. and Piper, D.J.W., 1997. Links between morphology and geotechnical characteristics of large debris flow deposits in the Albatross area on the Scotian Slope (SE Canada). Marine Georesources & Geotechnology, 15(3): 253-281.

Newton, S., Mosher, D., Shipp, C. and Wach, G., 2004. Importance of mass transport complexes in the Quaternary development of the Nile Fan, Egypt, Offshore Technology Conference, Houston, TX.

Niedoroda, A.W., Reed, C.W., Hatchett, L., Young, A., Lanier, D., Kasch, V., Jeanjean, P., Orange, D. and Bryant, W., 2003. Analysis of Past and Future Debris Flows and Turbidity Currents Generated by Slope Failures Along the Sigsbee Escarpment in the Deep Gulf of Mexico, Offshore Technology Conference, Houston, TX, pp. 1-7.

Normark, W.R., 1970. Growth patterns of deep-sea fans, American Association of Petroleum Geologists Bulletin. American Association of Petroleum Geologists : Tulsa, OK, United States, United States, pp. 2170-2195.

O'Brien, J.S. and Julien, P.Y., 1988. Laboratory Analysis of Mudflow Properties. Journal of Hydraulic Engineering, 114(8): 877-887.

Orange, D.L., Saffer, D., Jeanjean, P., Al-Khafaji, Z., Riley, G. and Humphrey, G., 2003. Measurements and Modeling of the Shallow Pore Pressure Regime at the Sigsbee Escarpment: Successful Prediction of Overpressure and Ground-Truthing with Borehole Measurements, Offshore Technology Conference, pp. 1-11.

Ostermeier, R.M., Pelletier, J.H., Winker, C.D., Nicholson, J.W. and Cowan, C.K., 2002. Dealing with Shallow-Water Flow in the Deepwater Gulf of Mexico. The Leading Edge(July): 660-668.

Ostermeier, R.M., Pelletier, J.H., Winker, C.D., Nicholson, J.W., Rambow, F.H. and Cowan, C.K., 2000. Dealing with Shallow-Water Flow in the Deepwater Gulf of Mexico, Offshore Technology Conference, Houston, TX, pp. 75-86.

Paola, C., Straub, K., Mohrig, D. and Reinhardt, L., 2009. The "unreasonable effectiveness" of stratigraphic and geomorphic experiments. Earth-Science Reviews, 97(1-4): 1-43.

Parsons, J.D., Whipple, K.X. and Simoni, A., 2001. Experimental study of the grain-flow, fluid-mud transition in debris flows. Journal of Geology, 109(4): 427-447.

Peakall, J., McCaffrey, B. and Kneller, B., 2000. A process Model for the Evolution, Morphology, and Architecture of Sinuous Submarine Channels. Journal of Sedimentary Research, 70(3): 434-448.

Pelletier, J.H., Ostermeier, R.M., Winker, C.D., Nicholson, J.W. and Rambow, F.H., 1999. Shallow Water Flow Sands in the Deepwater Gulf of Mexico: Some Recent Shell Experience, 1999 International Forum on Shallow Water Flows Conference Proceedings, League City, TX.

Phillips, C.J. and Davies, T.R.H., 1991. Determining rheological parameters of debris flow material. Geomorphology, 4(2): 101-110.

Piper, D.J.W., Farre, J.A. and Shor, A., 1985. Late Quaternary slumps and debris flows on the Scotian Slope. Geological Society of America Bulletin, 96(12): 1508-1517.

Piper, D.J.W., Pirmez, C., Manley, P.L., Long, D., Flood, R.D., Normark, W.R. and Showers, W., 1997. Mass-Transport Deposits of the Amazon Fan. In: R.D. Flood,

D. J. W. Piper, A. Klaus, and L. C. Peterson (Editor), Proceedings of the Ocean Drilling Program, Scientific Results, pp. 109-146.

Pirkle, E.C., 1960. Kaolinitic sediments in peninsular Florida and origin of the kaolin. Economic Geology, 55: 1382-1405.

Pirmez, C., 1994. Growth of a Submarine Meandering Channel-Levee System on the Amazon Fan, Columbia University, New York, 587 pp.

Pirmez, C., Isram, J., 2003. Reconstruction of turbidity currents in Amazon Channel. Marine and Petroleum Geology, 20: 823-849.

Pirmez, C., Marr, J., Shipp, C., and Kopp, F., 2004. Observations and Numerical Modeling of Debris Flows in the Na Kika Basin, Gulf of Mexico, Offshore Technology Conference, Houston, TX, pp. 1-13.

Posamentier, H. and Kolla, V., 2003. Seismic Geomorphology and Stratigraphy of Depositional Elements in Deep-Water Settings. Journal of Sedimentary Research, 73(3): 367-388.

Posamentier, H.W., 2003. Depositional elements associated with a basin floor channel-levee system: case study from the Gulf of Mexico. Marine and Petroleum Geology, 20: 677-690.

Poulos, S.J., 1981. The Steady-State Of Deformation. Journal Of The Geotechnical Engineering Division-Asce, 107(5): 553-562.

Poulos, S.J., Castro, G. and France, J.W., 1985. Liquefaction Evaluation Procedure. Journal Of Geotechnical Engineering-Asce, 111(6): 772-792.

Prins, M.A. and Postma, G., 2000. Effects of climate, sea level, and tectonics unraveled for last deglaciation turbidite records of the Arabian Sea. Geology, 28(4): 375-378.

Prior, D.B., Bornhold, B.D. and Johns, M.W., 1984. Depositional Characteristics of a Submarine Debris Flow. Journal of Geology, 92: 707-727.

Prior, D.B. and Suhayda, J.N., 1979. Application of infinite slope analysis to subaqueous sediment instability, Mississippi delta. Engineering Geology, 14(1): 1-10.

Rettger, R.E., 1935. Experiments on soft-rock deformation. Bulletin of the American Association of Petroleum Geologists, 19(2): 271-292.

Rogers, K.G. and Goodbred, S.L., Mass failures associated with the passage of a large tropical cyclone over the Swatch of No Ground submarine canyon (Bay of Bengal). Geology, 38(11): 1051-1054.

Sawyer, D.E., Flemings, P.B. and Dugan, B., 2007b. Lateral variations in core, log, and seismic attributes of a mass transport complex in the Ursa Region, IODP Expedition 308, Northern Gulf of Mexico, Paper # 19098, Offshore Technology Conference, Houston, TX, pp. 1-12.

Sawyer, D.E., Flemings, P.B., Dugan, B. and Germaine, J.T., 2009. Retrogressive failures recorded in mass transport deposits in the Ursa Basin, Northern Gulf of Mexico. J. Geophys. Res., 114.

Sawyer, D.E., Flemings, P.B., Shipp, R.C. and Winker, C.D., 2007a. Seismic geomorphology, lithology, and evolution of the late-Pleistocene Mars-Ursa turbidite region, Mississippi Canyon area, northern Gulf of Mexico. AAPG Bulletin, 91(2): 215-234, doi: 10.1306/08290605190.

Sawyer, D.E., Jacoby, R., Flemings, P.B. and Germaine, J.T., 2008. Data Report: Particle Size Analysis of Sediments in the Ursa Basin, IODP Expedition 308 Sites U1324 and U1322, Northern Gulf of Mexico. In: P.B. Flemings, J.H. Behrmann, C.M. John and a.t.E. Scientists (Editors), Proc. IODP, 308. Integrated Ocean Drilling Program Management International, Inc., College Station, TX, doi:10.2204/iodp.proc.308.205.2008.

Schwab, W.C., 1988. Causes of two slope-failure types in continental-shelf sediment, northeastern Gulf of Alaska. In: H.J. Lee (Editor), Journal of Sedimentary Petrology. Society of Economic Paleontologists and Mineralogists : Tulsa, OK, United States, United States, pp. 1-1.

Schwab, W.C., Lee, H.J. and Molnia, B.F., 1988. Causes Of Varied Sediment Gravity Flow Types On The Alsek Prodelta, Northeast Gulf Of Alaska. Marine Geotechnology, 7(4): 317-342.

Schwartz, H.-U., 1982. Subaqueous Slope Failures - Experiments and Modern Experiments. Contributions to Sedimentology, 11. E. Schweizerbart'sche Verlagsbuchhandlung (Nagele u. Obermiller), Stuttgart.

Seed, H.B., 1978. Wave-induced pore pressure in relation to ocean floor stability of cohesionless soils. In: M.S. Rahman (Editor), Marine Geotechnology. Crane, Russak & Co. : New York, NY, International, International, pp. 123-150.

Shengqiang, Y., Shiguo, W., Thomas, L., Genshun, Y., Fuliang, L., Feng, C., Hairong, W. and Li, L., 2009. Fine-grained Pleistocene deepwater turbidite channel system on the slope of Qiongdongnan Basin, northern South China Sea. Marine and Petroleum Geology, 26(8): 1441-1451.

Shepard, F.P., 1954. Nomenclature based on sand-silt-clay ratios. Journal of Sedimentary Petrology, 24: 151-158.

Shipp, R.C., Nott, J.A. and Newlin, J.A., 2004. Physical Characteristics and Impact of Mass Transport Complexes on Deepwater Jetted Conductors and Suction Anchor Piles, OTC 16751, Offshore Technology Conference. Offshore Technology Conference, Houston, TX, May 3-6, pp. 1-11.

Skempton, A.W., 1970. The consolidation of clays by gravitational compaction, Quarterly Journal of the Geological Society of London. Geological Society of London : London, United Kingdom, United Kingdom, pp. 373-411.

Steffens, G.S., Shipp, R.C., Prather, B.E., Nott, J.A., Gibson, J.L. and Winker, C.D., 2004. The Use of Near-Seafloor 3D Seismic Data in Deepwater Exploration and Production. Geological Society, London, Memoirs, 29(1): 35-43.

Stigall, J. and Dugan, B., 2010. Overpressure and earthquake initiated slope failure in the Ursa region, northern Gulf of Mexico. J. Geophys. Res., 115(B4): B04101.

Stow, D.A.A., 1986. Deep clastic seas. In: H.G. Reading (Editor), Sedimentary Environments and Facies. Blackwell Scientific Publications, Oxford, pp. 399-444.

Straub, K.M. and Mohrig, D., 2008. Quantifying the morphology and growth of levees in aggrading submarine channels. J. Geophys. Res., 113.

Strozyk, F., Strasser, M., Förster, A., Kopf, A. and Huhn, K., 2010. Slope failure repetition in active margin environments: Constraints from submarine landslides in the Hellenic fore arc, eastern Mediterranean. J. Geophys. Res., 115(B8): B08103.

Styzen, M.J., 1996. A Chart in Two Sheets of the Late Cenozoic Chronostratigraphy of the Gulf of Mexico, Gulf Coast Section, Society of Economic Paleontologists and Mineralogists, Houston, Texas.

Tappin, D.R., Watts, P., McMurtry, G.M., Lafoy, Y. and Matsumoto, T., 2001. The Sissano, Papua New Guinea tsunami of July 1998 - offshore evidence on the source mechanism. Marine Geology, 175(1-4): 1-23.

Terzaghi, K., 1956. Varieties of Submarine Slope Failures, 8th Texas Conference on Soil Mechanics and Foundation Engineering. University of Texas at Austin Bureau of Engineering Research, pp. 1-42.

Terzaghi, K. and Peck, R.B., 1948. Soil Mechanics in Engineering Practice. John Wiley & Sons, Inc., 566 pp.

Tripsanas, E.K., Piper, D.J.W., Jenner, K.A. and Bryant, W.R., 2008. Submarine mass-transport facies: new perspectives on flow processes from cores on the eastern North American margin. Sedimentology, 55(1): 97-136, doi:10.1111/j.1365-3091.2007.00894.x.

Twichell, D.C., Chaytor, J.D., ten Brink, U.S. and Buczkowski, B., 2009. Morphology of late Quaternary submarine landslides along the U.S. Atlantic continental margin. Marine Geology, 264(1-2): 4-15.

Urgeles, R., Canals, M., Baraza, J., Alonso, B. and Masson, D., 1997. The most recent megalandslides of the Canary Islands: El Golfo debris avalanche and Canary debris flow, west El Hierro island. Journal Of Geophysical Research-Solid Earth, 102(B9): 20305-20323.

Urgeles, R., Locat, J. and Dugan, B., 2007. Recursive Failures of the Gulf of Mexico Continental Slope: Timing and Causes. In: V. Lykousis, D. Sakellariou and J. Locat (Editors), Submarine Mass Movements and Their Consequences: 3rd International Symposium. Springer, pp. 11.

Urgeles, R., Locat, J., Sawyer, D.E., Flemings, P.B., Dugan, B. and Binh, N.T.T., 2009. History of Pore Pressure Build Up and Slope Instability in Mud-Dominated Sediments of Ursa Basin, Gulf of Mexico Continental Slope. In: D.C. Mosher et al. (Editors), Submarine Mass Movements and Their Consequences. Advances in Natural and Technological Hazards Research. Springer, Dordrecht, pp. 179-190.

Weber, M.E., Wiedicke, M.H., Kudrass, H.R., Hubscher, C. and Erlenkeuser, H., 1997. Active growth of the Bengal Fan during sea-level rise and highstand. Geology, 25(4): 315-318.

Weimer, P., 1990. Sequence Stratigraphy, Facies Geometries, and Depositional History of the Mississippi Fan, Gulf of Mexico. The American Association of Petroleum Geologists Bulletin, 74(4): 425-453.

Weimer, P. and Buffler, R.T., 1988. Distribution and seismic facies of Mississippi fan channels. Geology, 16: 900-903.

Weimer, P. and Shipp, C., 2004. Mass transport Complex: Musing on past uses and suggestions for future directions, OTC paper 16752, Offshore Technology Conference, Houston, TX, pp. 1-10.

Whitman, R.V., 1985. On liquefaction, Proceedings of the International Conference on Soil Mechanics and Foundation Engineering. A.A. Balkema : Rotterdam-Boston, International, pp. 1923-1926.

Williams, H. and Flint, S., 1990. Anatomy of a channel-bank collapse structure in Tertiary fluvio-lacustrine sediments of the Lower Rhine Basin, Germany. Geological Magazine, 127(5): 445-451.

Winker, C.D. and Booth, J.R., 2000. Sedimentary Dynamics of the Salt-Dominated Continental Slope, Gulf of Mexico: Integration of Observations from the Seafloor, Near-Surface, and Deep Subsurface, GCSSEPM Foundation 20th Annual Research Conference, pp. 1059-1086.

Winker, C.D. and Shipp, R.C., 2002. Sequence Stratigraphic Framework for Prediction of Shallow Water Flow in the Greater Mars-Ursa Area, Mississippi Canyon Area, Gulf of Mexico Continental Slope, 22nd Annual GCSSEPM Foundation Bob F. Perkins Research Conference, abs., pp. 1.

Yamamoto, Y., Sawyer, D.E., Behrmann, J.H., Flemings, P.B., John, C.M. and Party, I.E.S.S., 2005. Fabric contribution to sediment physical properties in Gulf of Mexico: Preliminary Results of IODP Expedition 308, Abstract OS21A-1514, Eos Trans. AGU, Fall Meet. Suppl.

Zakeri, A., Høeg, K. and Nadim, F., 2008. Submarine debris flow impact on pipelines -- Part I: Experimental investigation. 55(12): 1209.

Zreik, D.A., Ladd, C.C. and Germaine, J.T., 1995. A New Fall Cone Device for Measuring the Undrained Strength of Very Weak Cohesive Soils. Geotechnical Testing Journal, 18(4): 472-482.

Zühlsdorff, C., Wien, K., Stuut, J.B.W. and Henrich, R., 2007. Late Quaternary sedimentation within a submarine channel-levee system offshore Cap Timiris, Mauritania. Marine Geology, 240(1-4): 217-234.